Master's thesis

NTNU
Norwegian University of Science and Technology
Faculty of Engineering
Department of Structural Engineering

Bjørn Gjertsen
Sondre Tjessem

Testing and Modelling of Thick Aluminium Castings Under Impact Loadings

Master's thesis in Mechanical Engineering

Supervisor: Prof. Magnus Langseth / Assoc. Prof. David Morin / Torodd Berstad

June 2020

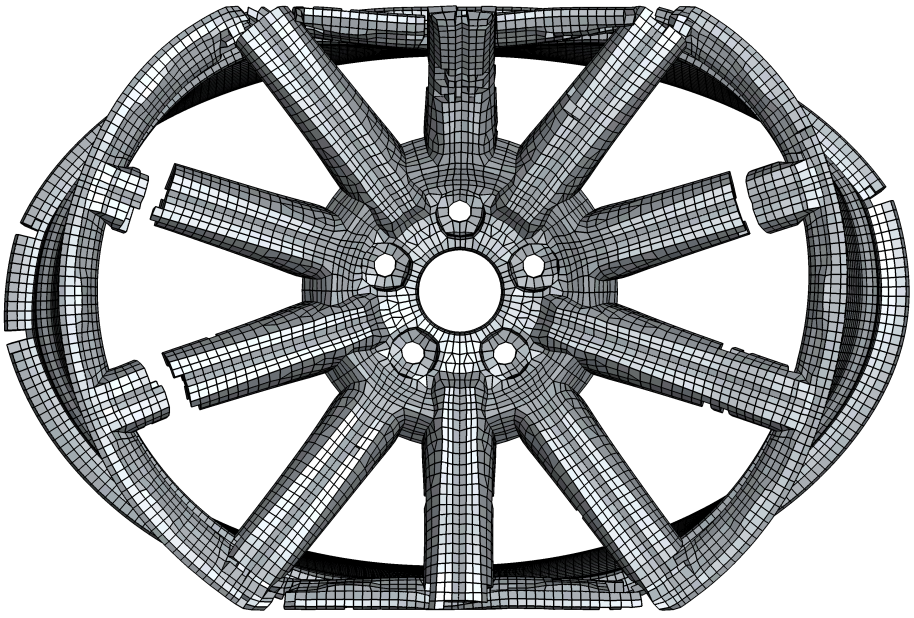

NTNU
Norwegian University of Science and Technology

Audi

Bjørn Gjertsen
Sondre Tjessem

Testing and Modelling of Thick Aluminium Castings Under Impact Loadings

Master's thesis in Mechanical Engineering
Supervisor: Prof. Magnus Langseth / Assoc. Prof. David Morin / Torodd Berstad
June 2020

Norwegian University of Science and Technology
Faculty of Engineering
Department of Structural Engineering

NTNU
Norwegian University of Science and Technology

Department of Structural Engineering
Faculty of Engineering
NTNU- Norwegian University of Science and Technology

ACCESSIBILITY
CLOSED

MASTER THESIS 2020

SUBJECT AREA: Numerical Analysis (SIMLab)	DATE: 15.06.2020	NO. OF PAGES: 78

TITLE:

Testing and Modelling of Thick Aluminium Castings Under Impact Loadings

Modellering og testing av tykke støpte aluminiumkomponenter utsatt for støtlast

BY:

Bjørn Gjertsen

Sondre Tjessem

SUMMARY:

This thesis aims to improve the numerical fracture formulation of a car rim made of die-cast aluminium and to determine an accurate and effective FEM formulation to be used in crash test simulations. New material tests will be performed in order to calibrate a state-of-the-art fracture criterion. Existing FE models will be improved upon, and novel models will be established. Special attention will be given to the implementation of a stress state dependent fracture criterion, as well as a stochastic fracture parameter following a Weibull distribution. Additionally, quasi-static rim tests will be performed, and the numerical models will be evaluated against these tests.

RESPONSIBLE TEACHER: Prof. Magnus Langseth

SUPERVISOR(S): Prof. Magnus Langseth, Assoc. Prof. David Morin, Torodd Berstad

CARRIED OUT AT: SFI CASA, Department of Structural Engineering, NTNU

MASTER THESIS 2020

Bjørn Gjertsen and Sondre Tjessem

Testing and modelling of thick aluminium castings under impact loadings

(Modellering og testing av tykke støpte aluminiumkomponenter utsatt for støtlast)

Nowadays, crash requirements of automotive structures involve chassis parts in addition to the traditional body in white. Recently, the Insurance Institute for Highway Safety (IIHSS) in the U.S. has released new crash scenarios which solicitate the full front end of a car. For example, a new test (referred to as the small overlap frontal test), subjects only 25% of the front end of a vehicle to a 64 km/h impact. Under these circumstances, the suspension system of the vehicle, including the wheel and rim, becomes part of the solution to manage the energy from the impact. Special numerical techniques must therefore be developed to ensure the accuracy of the numerical simulations used during the design of an automotive structure. This can only be achieved by having reliable test facilities for computer code validation.

In 2018 and 2019, a master thesis was run at CASA on the development of a test rig for impact testing of cast aluminium rims. The basis for the design was a numerical model of the test rig including the rim as well as the trolley and the reaction wall of the SIMLab "Kicking Machine". The main objective with the present thesis is to carry out impact testing for validation of a novel modelling approach for aluminium casting. Included here is also quasi-static tests as a reference. The thesis work will be carried out in close cooperation with Audi and includes a trip to the Audi plant in Ingolstadt, Germany.

The activities in this master thesis research work may include:

- A literature review of aluminium alloys/castings including constitutive and failure models as well as structural testing of rims.
- Material testing.
- Quasi-static and impact testing of of rims.
- Validation of a numerical model for the rims based on the tests carried out.
- Modelling guideliens for large scale simulations.
- Reporting

The candidate may agree with the supervisors to pay particular attention to specific parts of the investigation, or include other aspects than those already mentioned. The thesis is to be organized as a research report, recognising the guidelines provided by the Department of Structural Engineering.

The report is to be handed in not later than 15 June 2020.

Supervisors at NTNU: David Morin, Torodd Berstad and Magnus Langseth

NTNU, 15 January 2020

Magnus Langseth

Acknowledgements

First and foremost, we would like to thank the Centre of Advanced Structural Analysis (SFI CASA) and the Department of Structural Engineering at the Norwegian University of Science and Technology (NTNU) for providing an exciting topic for our master's thesis and great lectures. Great lectures in the mechanics courses throughout the years have been an inspiration to pursue the direction of mechanics and the finite element method in the mechanical engineering study programme. This has given us great value for the time at NTNU in terms of a fundamental theoretical understanding of methods used to solve mechanics problems.

A special thanks to our supervisors at SFI CASA, prof. Magnus Langseth, assoc. prof. David Morin and Torodd Berstad for offering a thesis on this challenging yet exciting topic and for providing guidance throughout our work. With a steep learning curve, the discussions with our supervisors have always been fruitful and of great help to further our understanding. The invaluable help of Torodd Berstad for giving great advice for numerical modelling and implementing a user material in LS-DYNA should also be mentioned.

Lastly, we would like to thank Tore Wisth and Trond Auestad for their great help with the planning and execution of the rim tests.

Abstract

The present thesis aims to establish and improve a finite element (FE) model to accurately capture the behaviour of a car rim subjected to impact loadings, using state-of-the-art modelling techniques. This development is part of an ongoing project at the Centre of Advanced Structural Analysis (SFI CASA) in cooperation Audi AG. Both experimental and numerical work was carried out to validate and improve both existing and novel FE models.

Previously, extensive material testing of the die-cast aluminium rim material has been performed, and an elastic-viscoplastic material model with a Cockcroft-Latham (CL) fracture criterion has been calibrated. Furthermore, a FE model has been established in the FE-software, Abaqus, a test rig for impact testing of rims has been constructed, and a force estimation scheme to estimate rim crushing forces during impact has been developed. The test rig and force estimation scheme have been validated, and four dynamic rim tests were performed.

In the present work, improvements of the previously established FE model were pursued in two separate ways. Firstly, by investigating the performance of an automatically meshed tetrahedral model, which if satisfactory, can significantly cut modelling time. Secondly, by an improvement of the material model, making use of a stress state dependent and probabilistic fracture model, composed by the Extended Cockcroft-Latham (ECL) fracture criterion and a Weibull-distributed fracture parameter. The performance was evaluated by comparison to physical rim tests and the other FE models, in quasi-static and dynamic loading conditions.

Extensive experimental and numerical work was conducted. To avoid the use of a force estimation scheme and to obtain more reliable experimental results, four rims were tested under quasi-static loading. Furthermore, several material tests were conducted experimentally and numerically in different stress states to calibrate the ECL fracture criterion. Three different baseline rim models were established in the FE-software, LS-DYNA, differing mainly in their geometric discretization, two shell-brick (S-B) hybrid models, referred to as S-B Simple Coupling and S-B Full Coupling, and one Tetrahedral model. These models were all formulated with the CL fracture criterion. With the S-B models differing in the interface between the shell and brick elements in the sense that only the S-B Full Coupling model transfers the moment between the element types.

The S-B Full Coupling and the Tetrahedral model were able to capture the general trends seen experimentally. While the S-B Full Coupling model had a clear advantage in computational cost, the Tetrahedral model had the time advantage in meshing. When probabilistic fracture model was included, the S-B Full Coupling was the only accurate model. This is believed to be due to size effects, as the element size of the S-B model was closer to the volume of the material specimens. The size effect is also believed to be the reason why the stress state data, used to calibrate the ECL fracture criterion, is deemed unreliable. The stress state data contradicted the trend that fracture strain decreases as triaxiality increases, as indicated in literature. To what extent the stochastically distributed defects in the die-cast material caused this is further discussed.

Lastly, some concluding remarks and recommendations for further work are presented.

Sammendrag

Denne masteroppgaven har som mål å etablere og forbedre en elementmetode (FE) modell som fanger opp oppførselen til en bilfelg utsatt for støtlast, ved bruk av "state-of-the-art" modelleringsteknikker. Utvikling er en del av et pågående prosjekt ved Centre of Advanced Structural Analysis (SFI CASA) i samarbeid med Audi AG. Både eksperimentelt og numerisk arbeid ble gjennomført for å validere og forbedre både en eksisterende og nye FE modeller.

Det har tidligere blitt gjennomført omfattende materialtesting på det støpte materialet som felgene er lagd av, og en elastisk-viskoplastisk materialmodell med et Cockcroft-Latham (CL) bruddkriterium har blitt kalibrert. Videre, har en FE modell blitt laget i FE-programvaren Abaqus, en testrigg for støttesting av felger har blitt lagd, og en prosedyre for estimering av krefter ved støtlast har blitt utviklet. Testriggen og prosedyren for beregning av krefter har blitt validert, og fire dynamiske felgtester ble gjennomført.

I dette arbeidet har forbedring av de tidligere FE modellene blitt undersøkt på to forskjellige måter. Først ved å undersøke ytelsen av en tetraedermodell skapt med automatisk generert netting som, om funnet tilfredsstillende, kan lede til betydelig kortere modelleringstid. Videre, ved å forbedre materialmodellen ved å bruke en spenningstilstandsavhengig og probabilistisk bruddmodell, bestående av et utvidet Cockcroft-Latham (ECL) bruddkriterium og en Weibull-distribuert bruddparameter. Ytelse ble evaluert ved sammenligning med fysiske felgtester og de andre FE modellene, under kvasi-statiske og dynamiske lasttilfeller.

Omfattende eksperimentelt og numerisk arbeid ble utført. For å unngå bruken av en prosedyre for kraftestimering, og for å oppnå mer pålitelige eksperimentelle resultater, ble fire felger testet under kvasi-statisk last. Flere materialtester ble gjennomført, både eksperimentelt og numerisk ved forskjellige spenningstilstander for å kalibrere ECL bruddkriteriet. Tre forskjellige utgangspunkts modeller ble lagt i FE-programvaren LS-DYNA. Disse er først og fremst ulike i diskretisering av geometrien, hvorav det var to skall-kube (S-B) hybridmodeller, referert til som "S-B Simple Coupling" og "S-B Full Coupling", og en modell med tetraeder elementer. Alle modellene ble formulert med CL bruddkriteriet. Forskjellen mellom S-B modellene ligger i grensesnittet mellom skall og kubeelementene i den forstand at kun "S-B Full Coupling" modellen er i stand til å overføre momenter mellom de forskjellige elementtypene.

"S-B Full Coupling" og tetraedermodellen var i stand til å fange de generelle trendene sett eksperimentelt. Samtidig som "S-B Full Coupling" har et klart fortrinn når det kommer til beregningskostnad, har tetraedermodellen en tidsfordel når det kommer til nettgenerering. Når den probabilistiske bruddmodellen ble brukt var "S-B Full Coupling" den eneste nøyaktige modellen. Dette er antatt å være på grunn av størrelseseffekter, ettersom størrelsen på S-B modellen er nærmere volumet til materialprøvestykkene. Størrelseseffekten er også trodd å være grunnen til at spenningstilstands dataen som ble brukt til å kalibrere ECL bruddkriteriet ble vurdert til å være upålitelig. Spenningstilstands dataen var i motsigelse med trendene at bruddtøyning reduseres når triaksialiteten øker, noe som er sett i litteraturen. I hvilken grad dette skyldtes de stokastisk fordelte defektene i det støpte materialet blir videre diskutert.

Til slutt presenteres noen konkluderende bemerkninger og anbefalinger for videre arbeid.

Table of Contents

Chapter 1

Introduction

The work in this thesis was conducted at the Centre for Advanced Structural Analysis (SFI CASA) at the Norwegian University of Science and Technology (NTNU). SFI CASA is a world-leading research group developing theory and methods to model the behaviour of materials and structures subjected to blast and impact loading. One of the groups ongoing projects is in collaboration with Audi AG. This project aims to accurately predict the structural response of a car rim subjected to impact loads in a full-scale car model, an important piece in the continuous improvement of passenger vehicle safety.

1.1 Motivation

Up until recently, the framework for evaluating vehicle safety has failed to cover crash scenarios that account for a large portion of fatal accidents. According to the Insurance Institute for Highway Safety (IIHS), the energy-absorbing structures of today's vehicles fail to engage in one in four fatal frontal accidents [1]. This unsatisfactory performance of the vehicle safety system motivated the release of new crash scenarios that assess the full front end of the car, including the small overlap crash test, shown in Figure 1.1 [2] [3].

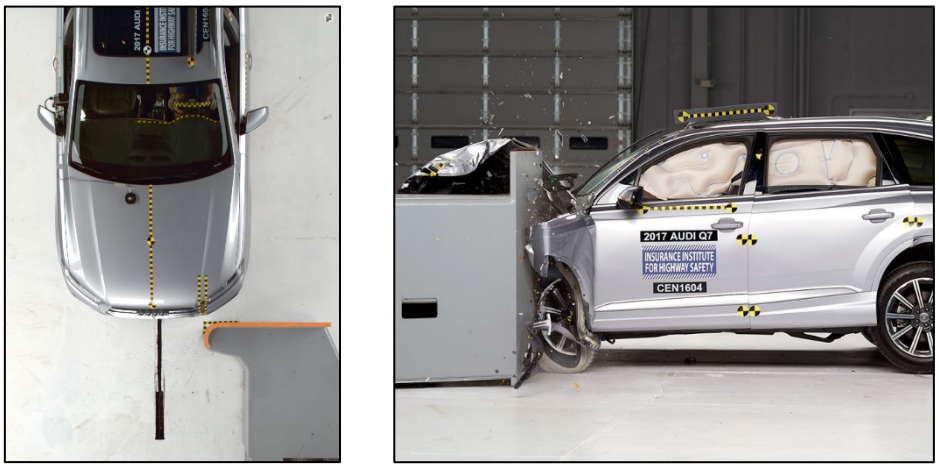

a) b)

Figure 1.1: Small overlap crash test of the 2017 Audi Q7, a) top view, b) side view showing large deformations and fracture of the rim [3].

By the release of new crash tests, car producers such as Audi need to consider new structural designs, utilising new parts of the car to absorb energy. Compared to previous crash tests, the small overlap crash test requires the suspension and rim to absorb more of the energy, as opposed to the crash box located closer to the centre of the car. The *crash box* is a typical component of every modern car, specifically designed to absorb energy in frontal accidents. However, in a small overlap crash, this system fails to fully engage, leading to a transfer of impact forces to the suspension and rim. The role of the rim is apparent in Figure 1.1 b), where large deformations and fracture can be seen. In this case, the energy absorption of the rim becomes vital to meet the safety standards of tomorrow.

Since crash testing of prototype vehicles is costly, the automotive industry aims to increase the use of numerical simulations using the *finite element method* (FEM). However, car rims are particularly challenging to model for several reasons. Firstly, in impact loading, the calibration of advanced material and fracture models is required. Secondly, modelling of fracture is especially challenging as car rims typically are *die-cast*, resulting in a material with stochastically distributed *defects*. Lastly, the intricate geometry of the rim complicates the modelling.

1.2 Objective and Scope

This thesis aims to improve the numerical fracture formulation of a car rim made of die-cast aluminium and to determine an accurate and effective FEM formulation to be used in crash test simulations. The numerical Abaqus model used in previous work will be transformed into an LS-DYNA model, to make use of LS-DYNA specific capabilities. LS-DYNA is a FEM software developed by Livermore Software Technology Corporation (LSTC). Figure 1.2 illustrates how such a numerical model can reproduce the behaviour of a physical rim. New material tests will be performed in order to calibrate a state-of-the-art *fracture criterion*. A review of recent research on fracture modelling will form the basis for the selection of the fracture criterion. In order to represent the stochastically distributed defects in the die-cast material, a combination of new and old material tests will be used to calibrate a *probabilistic* fracture model. The performance of the numerical model will then be evaluated against experimental rim tests. For this purpose, new *quasi-static* rim tests will be performed. By quasi-static loading, it is meant that loading is applied sufficiently slow so that the inertial forces are vanishingly small compared to the static forces. Additionally, a parametric study will be carried out to assess the effects of a range of *finite element* (FE) modelling choices.

Although the overall goal of the project is to establish a numerical rim model for use in full-scale car crash simulations, this thesis is mainly concerned with the development of an accurate rim model. Therefore, the numerous considerations that need to be made in order to incorporate the rim model into a full-scale car crash analysis are out of scope for the present work. As a consequence of the complex rim design, it is challenging to discretize the geometry of the rims into elements. There are two alternatives, manual meshing using *shell* and *brick* elements, or automatic meshing using *tetrahedral* elements. Since manual meshing is very labour intensive, it is desirable to evaluate the performance of a tetrahedral element model. A *hybrid model*

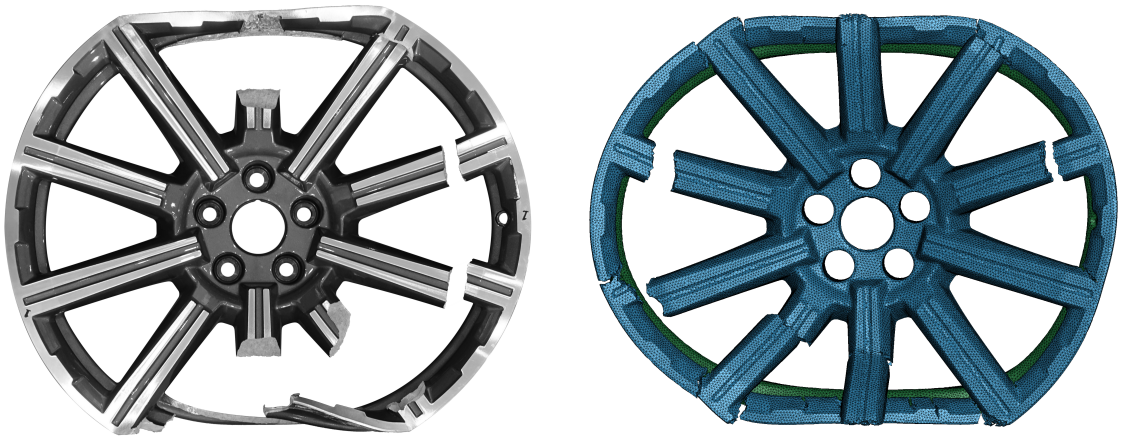

a) b)

Figure 1.2: Deformed rims, a) physical test, b) numerical simulation.

consisting of shell and brick elements has been used in the previous work and will be used as a reference. A weakness of this hybrid model is that the moments are not transferred between the two structural parts of the rims, resulting in a component stiffness that is inadequate. Alternatives to obtain a more accurate stiffness of the model will, therefore, be considered. The study will be limited to three different *baseline models*, two hybrid models, and one tetrahedral model. The two hybrid *shell-brick* (S-B) models differ in the way that the interface and *coupling* between the two element-types are modelled.

In order to limit the uncertainties regarding experimental measurements, quasi-static experiments and numerical simulations are used as opposed to the previously used *dynamic* loading conditions. This helps simplify the problem so that the performance of the numerical model can more readily be evaluated.

As this thesis is a continuation of an ongoing project, the extent to which previous work is evaluated needs to be clarified. The authors will not attempt to thoroughly evaluate the previous work conducted at SFI CASA or Audi's design of the rim. Results previously obtained will be used as a starting point, but the methods used to obtain them will not be explained. Instead, the reader will be referred to the previous works. However, some thoughts and comments regarding past work are included where necessary.

To the knowledge of the authors, this work is one of the first attempts to achieve a combination of *stress state* dependent fracture and probabilistic fracture model in a FE model for a component made out of a die-cast material.

Chapter 2 provides some background information about the rim manufacturing process and an overview of the fundamental theoretical aspects of *materials mechanics*, fracture modelling and explicit nonlinear FEM. Chapter 3 gives the reader a description of the methods used in experimental testing, calibration of material models and numerical modelling. Chapter 4 presents both experimental and numerical results, along with a brief discussion on each topic. Topics that require a more in-depth discussion are saved for Chapter 5, where a comprehensive discussion is found. Finally, Chapter 6 outlines the main conclusions and provides recommendations for further work.

1.3 Previous Work

The present work is a continuation of previous work conducted at SFI CASA in collaboration with Audi and extends upon the work from three former master's theses.

In 2017, Kittilsen and Swanberg calibrated an elastic-plastic material model based on several quasi-static tensile tests, taken from various locations of two Audi Q7 rims [4]. Numerous test specimens were taken from both the spokes and the bed of the rims, in order to characterize the stochastic behaviour and variation in the material properties throughout the rims. Based on the tensile tests, *systematic global variations* in the material properties were found between the rim bed and the spokes, and a separate material model was calibrated for these two sections of the rim. Furthermore, large *pseudo-random variations* were found within the spokes. In order to account for this scatter, a stochastic fracture model based on a normal distribution of the fracture parameter was developed and implemented. The FE-software Abaqus was used. In order to validate the numerical model, two separate component tests were attempted. A compression test of half a rim was attempted but was aborted due to safety concerns. Additionally, a spoke bending test was performed and showed good agreement with the numerical model.

As the first quasi-static component tests attempted by Kittilsen and Swanberg were aborted due to safety concerns, a test rig was needed to complete a rim compression test. In 2018 Martinsen developed the design of a test rig to be used in dynamic impact tests of the rims [5]. Along with the test rig, the concepts of a *force estimation scheme* for dynamic tests were outlined.

Dahler and Thuve then validated the test rig in 2019 and performed dynamic tests of four rims [6]. A complex scheme for filtering and estimation of the forces was developed and validated. Additionally, new material tests were performed in order to confirm the material parameters obtained by Kittilsen and Swanberg and to assess the strain rate sensitivity of the material. Based on the new material tests, the material model was slightly altered, and strain rate sensitivity was included. The dynamic rim tests were simulated numerically and compared with the experiments. Acceptable results were obtained, but a more accurate model was still desired. Several factors that could affect the results were pointed out, mainly uncertainties regarding the test rig, the force estimation scheme, and the numerical rim model. Several improvements were suggested, including the choice of fracture model and element formulation.

Based on these three theses, uncertainties regarding the accuracy of the numerical model and the accuracy of the experimental data obtained from dynamic experiments remain. Thus, further work should focus on quasi-static tests, where forces can be easily be measured, and the numerical formulation of the rim model. The fracture model is identified as one of the aspects that need further development.

The quasi-static tests performed in 2017 applied the load to the rims in such a way that the spokes of the rim failed in a tension dominated stress state. The selected fracture criterion accurately described the fracture. However, when the rim is subjected to more complex loading, such as during a car crash, it is uncertain how accurate this fracture model will be. Performing new quasi-static tests where the whole rim is crushed will also test this. Furthermore, the selection of a normal distribution for fracture modelling has to be reconsidered.

Chapter 2

Background and Theory

Since this thesis is a continuation of previous work, this chapter will focus mainly on the background and theory that is unique for the present work. First, a short introduction about the rim material, manufacturing process, and design are given. Second, the central notions in material mechanics and FE formulation will be presented in greater detail. Lastly, a short description of the most important measurement tools is made.

2.1 Material, Manufacturing and Rim Design

2.1.1 Aluminium

Aluminium alloys are highly versatile materials that have seen a rapid increase in its usage in the automotive industry throughout the last decades and are currently the second most utilised material in car construction, after steel. There are several properties that make aluminium alloys appropriate for use in cars, one of which is its high strength and ability to absorb energy relative to its low weight. Due to its high ductility, aluminium alloys have been shown to be able to absorb twice the energy of mild steel during crash loading, relative to its weight.

Additionally, in today's market, there is a continuously increasing focus on weight reduction of vehicles, particularly in order to reduce energy consumption and emissions. An advantage of aluminium is that almost 90% of the aluminium can be recycled, which reduces the need for mining of new metal ore, as well as reducing the amount of energy required for production.

The combination of properties of aluminium alloys makes it possible to design and manufacture safer vehicles, while at the same time reducing the weight and emissions [7].

2.1.2 Die-Casting

Casting was one of the first shaping processes to be discovered and has been used by humans for several thousands of years. Casting is a process in which molten material is poured into a mould, where it is left to solidify. The mould consists of a cavity with the negative shape of the casting. Note that casting refers to both the process itself and the resulting part. Once the material has solidified, the mould is opened. The cast part can then be removed [8].

In metal casting, moulds are categorised as either expendable or permanent moulds. As the names imply, expandable moulds are used only once while permanent moulds can be reused. Die-casting is a permanent mould process. In die casting the liquid metal is injected into a permanent mould under pressure [8].

One of the main advantages of casting is the possibility to make parts with complex shapes that require little or no further processing after the casting process. Certain casting processes, such as die-casting, are also highly appropriate for mass production, explaining its common use for certain automotive parts [8]. There are also some disadvantages associated with casting processes, particularly when it comes to the mechanical properties of the cast parts. This is due to the pseudo-random nature of the casting process. During the flow of the molten material into the cavity of the mould, complex flows and temperature fields are highly sensitive to slight changes in the external environment as well as process parameters [9]. Figure 2.1 shows images of the three main types of defects associated with die-casting of aluminium.

Shrinkage porosity is a defect that arises due to the volume reduction of the part as the alloy solidifies. This can be especially detrimental in thick geometries due to high temperature gradients [9].

The presence of gaseous bubbles in the molten metal leads to *gas porosity*. These bubbles may consist of different gases. One of the sources of gas porosity are bubbles of air that arise due to the turbulent flow as the moulds are filled under high pressures. Another source is hydrogen. As the temperature of the molten metal decreases during cooling, the hydrogen solubility is reduced. Thus, hydrogen will come out of solution in bubbles and cause small pores in the metal [9].

When molten metal is in contact with air, it will likely form thin *oxide films*. These oxide films disrupt the bonding in the metal and will effectively function as tiny cracks in the cast parts [9].

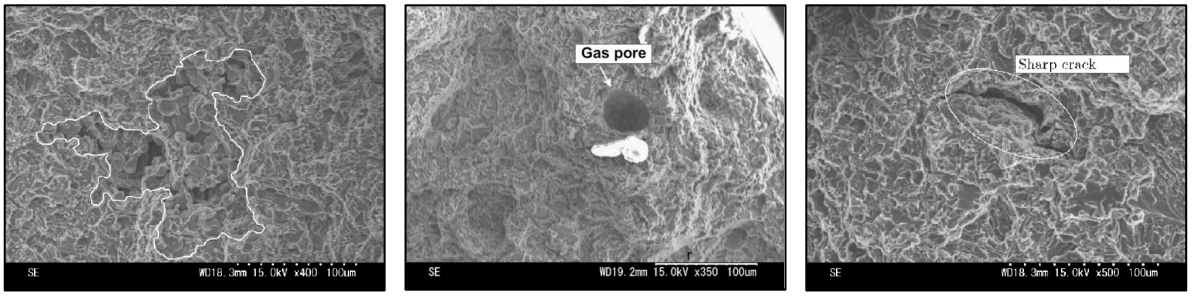

Figure 2.1: Typical defect types in die-cast aluminium parts, a) shrinkage porosity, b) gas porosity, c) oxide film [9].

2.1.3 Precipitation Hardening

Precipitation hardening is a heat treatment process that can be applied to certain metal alloys in order to increase their strength. Although the metal alloys subjected to precipitation hardening often contain several alloying elements, a hypothetical example alloy consisting of only two elements will be used to explain the principles of the process. This example follows the explanation given in the textbook by Callister and Rethwisch [10]. The hypothetical alloy can be represented by a *binary phase diagram* shown in Figure 2.2 a). The example alloy is made up of the two elements A and B, with a composition C_0. C_0 is the weigh-percentage of B in the alloy. The process consists of two separate heating-cooling cycles.

The first cycle is known as *solution heat treating*. From the initial temperature T_1 the material is heated up to T_0. This induces a phase change, from a mix of α and β at T_1 to a state of only α-phase at T_0. The material is then quenched. This induces a cooling rapid enough to prevent any β-phase from being formed. The α-phase is now supersaturated with B atoms. Although there is no equilibrium at this stage, most alloys have slow diffusions rates at low temperatures. Some duration of time can, therefore, pass without the generation of any new β-phase.

In the second heating cycle, called *precipitation heat treating*, the alloy is heated to the temperature T_2. T_2 remains within the $\alpha + \beta$ region, and the diffusion rates are drastically increased. Fine particles of β-phase will now start to form within the α-phase matrix. The α-phase is now of composition C_α, while the β-phase has composition C_β. At the end of the process, the alloy is again cooled to room temperature. Figure 2.2 b) shows the varying temperature versus the time of the process. The small particles lead to increased resistance to dislocations in the material, which strengthens and hardens the material [10].

2.1.4 Ductile and Brittle Fracture

Fracture is characterized by the separation of a component into several pieces, usually due to external loading. Metals may fracture in two distinctly different fracture modes. These are

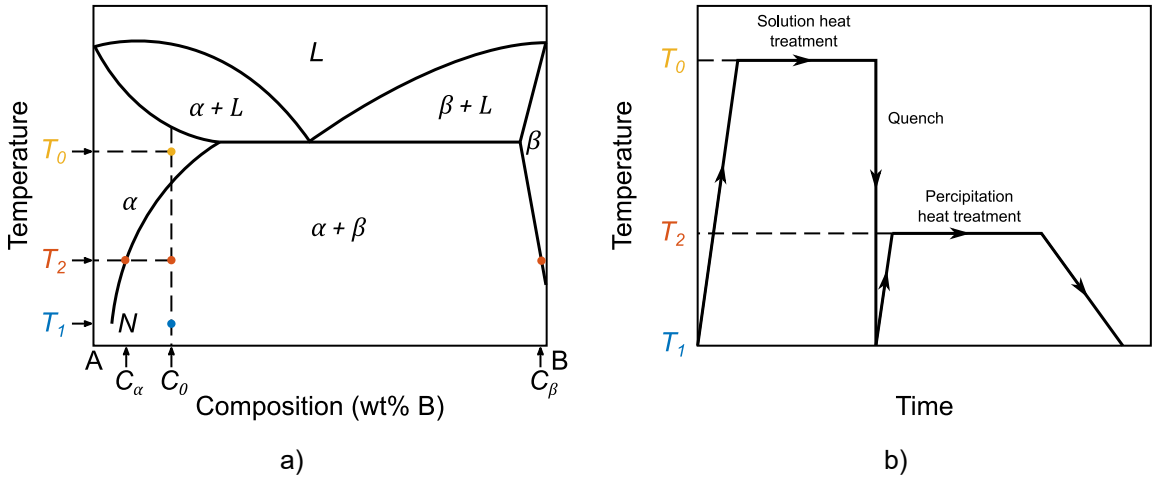

Figure 2.2: Illustrations of the precipitation hardening principles of a hypothetical alloy, a) binary phase diagram, b) temperature vs time history. Reproduced from figure in [10].

known as *brittle fracture* and *ductile fracture.* Brittle fracture refers to the situation where the material fractures before any significant plastic deformation is observed. If the material deforms plastically before fracturing, it is classified as ductile [10].

Fracture is a process consisting of two steps, crack initiation and crack propagation. Ductile and brittle fracture differ mainly in the way that the crack propagates. In brittle fracture, the crack propagates rapidly without much plastic deformation. This is an unstable process as the crack will propagate until fracture, regardless of whether the loading is increased or maintained. Before ductile fracture the cracks propagate much more gradually, accompanied by large plastic deformations. In this case, the crack will not continue propagating unless the magnitude of the loading is increased, and the process is therefore characterized as stable [10].

2.1.5 Rim Design

The 20 by 9-inch Audi 2017 ALY58988 low-pressure die-cast rim was investigated throughout the project. The measurements are based on the inner measurements of the tires that are fitted on the rims. The actual physical diameter of the rims was measured to $547\ mm$, with a width of $255\ mm$. The rims have a mass of approximately $15.7\ kg$ [6]. The rim has ten spokes with alternating lengths, five short spokes and five long spokes. The rim is further divided into two main sections, the *spokes* and the *rim bed*. Figure 2.3 displays the rim in two different views, showcasing the spokes and the rim bed. Figure 2.3 a) shows the orientation that is referred to as the *short spoke configuration*, where a short spoke is facing the impacting wall.

The rims are made of the aluminium alloy AlSi7Mg-T6, which is a precipitation-hardened alloy with Si (7 wt%), Mg (0.3 wt%), Fe (0.2 wt%), Mn (0.1 wt%), Zn (0.1 wt%) and Cu (0.05 wt%) as the alloying elements [4]. Although no information about the manufacturing process has been revealed, a more detailed characterization based on thoughtful assumption can be found in the thesis by Kittilsen and Swanberg [4].

Figure 2.3: 2017 Audi Q7 ALY58988 rim, a) top view showing the short spoke configuration, b) side view. Modified version of image found in [4].

2.2 Materials Mechanics

In this section, a thorough look at the theory used to represent material behaviour in a FE model is made. Several pages are dedicated to this important topic, as it is crucial in understanding how components such as car rims can be represented in a numerical model. Not all equations and symbols will be fully established and defined. Instead, the reader is referred to the relevant literature. The essential equations are summarized on the last page of this section in Figure 2.7.

The field of materials mechanics concerns the behaviour of materials subjected to various loads. Although materials have been studied since ancient times and today's knowledge undoubtedly suffices for a broad range of applications, in some cases, it still becomes a great challenge to predict material behaviour. With the use of FEM becoming increasingly important, the branch of materials modelling called *continuum mechanics* is central in the numerical representation of materials. The key assumption in continuum mechanics is that the material or substance completely fills the space it occupies, and its physical properties are continuous over the same space [11]. The mathematical representation of the materials makes use of tensors [12]. Meaning that the die-cast material will be modelled by a continuous mass, ignoring the complex atomic-scale structures. It is therefore important to remember that while much of the characteristics of the materials can be explained by its atomic structure, it is not how the material is represented in a numerical FE model.

For materials, the relationship between stresses and strains is of primary interest, as it gives a description of how the material deforms when subjected to a load. This relation is called a *constitutive relation* and can also include the effects of other influencing factors, such as temperature. In addition to constitutive equations, the fracture behaviour of the material must be represented by a fracture criterion. Fracture modelling is significantly complicated by the distribution of defects in the die-cast material, adding stochastic variation to the material model.

2.2.1 Components of a Material Model

In impact problems where large deformations and possibly fracture occurs, a material model will typically consist of the following components [9] [12]:

- Elasticity
- Yield criterion
- Hardening rule
- Flow rule
- Loading/unloading conditions
- Fracture criterion

These terms and the symbols used in their mathematical formulation will now be explained.

The important symbols used in the mathematical representation are, first of all, $\boldsymbol{\sigma}$ and $\boldsymbol{\varepsilon}$, which represent the stress and strain tensor, respectively. Additionally, $\boldsymbol{d}$, is the rate-of-deformation tensor, so that the strain increment can be obtained as $d\boldsymbol{\varepsilon} = \boldsymbol{d}dt$.

Elasticity is the domain of strain where the deformations are reversible, path independent, and the deformation energy can be recovered. In the relation describing the stresses and strains in this domain, the *Young's modulus*, E, and *Poisson's ratio*, v, are typical material parameters used. As explained by Knoll in his PhD, the casting process of die-cast materials results in a very fine microstructure with pseudo-randomly distributed casting defects, which in turn results in a material with no clear direction dependence [9]. A material without any directional dependence is called *isotropic*.

At some point of deformation, the material transitions into what is called the *plastic domain* where stresses and strains no longer follow the linear relation typical of metals in the elastic domain. In this region, it is distinguished between deformations that are elastic and plastic. This is done by decomposing the deformation by its elastic and plastic components, often called *additive decomposition*. The transition into this domain is described by the *yield criterion* which takes some function for the *equivalent stress*, σ_{eq}, and compares it to a reference stress called the *yield stress*, σ_0. For an isotropic material, the *von Mises* equivalent stress is commonly used [13]. Furthermore, yielding typically depends on the *deviatoric stress*, meaning that the yielding is independent of the hydrostatic stress. Deviatoric stress is further explained in [12].

In the plastic domain, materials typically experience *work hardening*, which is resulting from changes in the microstructure of the material. Work hardening increases the yield strength of the material, expanding the elastic domain, and often depends mainly on three factors, plastic strain, plastic strain rate and temperature. Plastic strain and plastic strain rate are denoted as p and $\dot{p}$, respectively. Furthermore, some relation between the stress tensor, $\boldsymbol{\sigma}$, and the *plastic strain rate tensor*, $\dot{\boldsymbol{\varepsilon}}^p$, is needed. This is called the *flow rule*, and also assures that the material cannot deform in the opposite direction of loading by enforcing non-negative dissipation. Commonly, for metals, an *associated flow rule* is used, which assumes that the plastic strain increment is normal to the yield surface, also called the *normality rule*. Lastly, to distinguish between elastic loading/unloading and plastic loading, a set of equations called the *loading/unloading conditions* are required.

The ductility of a material is determined by the fracture behaviour and is linked to the materials ability to absorb energy. Consequently, in impact mechanics and analysis of structures subjected to dynamic loads, an accurate fracture model is highly important. The fracture model can either be dependent on the plastic formulation of the material or assumed to be independent. These two alternatives are referred to as *coupled* and *uncoupled fracture,* respectively. In coupled damage, the material damage is included in the constitutive equations so that material damage directly influences the plastic behaviour. However, this can lead to cumbersome calibration of material parameters. Uncoupled fracture has the advantage that it results in simple identification of damage parameters, as the plasticity model and fracture model can be calibrated separately. Fracture of the material is defined when some criterion is met, often depending on the stress state and the equivalent plastic strain [13]. The type of loading the material is subjected to, is referred to as the stress state.

2.2.2 Modified Johnson-Cook Plasticity for Uncoupled Damage

With the general key terms and concepts defined and briefly explained, the next step is to look into a specific material model and its applicability to describe the material at hand. The *Modified Johnson-Cook* (MJC) model is a version of the *Johnson-Cook* (JC) model, where hardening rule is replaced by the isotropic Voce hardening rule, and strain rate sensitivity is included through the generalised *Norton creep law* [13] [14]. An uncoupled version of the MJC plasticity model proposed by Børvik et al. describes the plastic behaviour of the material independently of the material damage [15]. The model is hypoelastic, meaning that the constitutive model is independent of the finite strain measures except in the linearized cases [16], and uses von Mises yield criterion and the associate flow rule. Rate-of-deformation tensor $\boldsymbol{d}$ is decomposed into elastic and plastic parts according to the additive decomposition. *Jaumann stress rate* $\boldsymbol{\sigma}^{\nabla \mathrm{J}}$ is adopted to ensure a good representation for large deformations and large rotations. Two-terms Voce rule is used as the isotropic hardening rule. See Figure 2.7 for the key equations of this model. At SIMLab the MJC material model has already been implemented in Abaqus as a user material, while in LS-DYNA this material model available as standard.

2.2.3 Generic Ductile Fracture Criterion

The term *ductile failure criterion* applies to fracture criteria where the straining history of the material is evaluated and fracture defined at some critical value for the *equivalent plastic strain*, p_f. Sometimes also simply referred to as the *fracture strain*.

When it comes to establishing a fracture criterion, the crux of the matter is to determine what quantity throughout the deformation of the material that has an influence on fracture strain. The most conventional criteria make use of the stress space of the material, which is expressed by the principal stresses. However, recent research shows that the stress state in terms of the stress invariants is of great importance for fracture [17] [12]. This stress state dependence is not only seen by the use of physical experiments but also in micromechanical modelling and unit cell analysis [18] [19] [20]. Providing strong support for a fracture being dependent on the stress invariants. By the term *invariant,* it is meant that these are quantities that do not change under coordinate transformation and the three commonly used invariants of the stress tensor, $\boldsymbol{\sigma}$, are the *von Mises equivalent stress*, σ_{eq}, *triaxiality*, σ^*, and *Lode parameter*, L.

Triaxiality describes the relative magnitude of the *hydrostatic pressure,* σ_h, and the equivalent stress, expressed mathematically as

$$\sigma^* = \frac{\sigma_h}{\sigma_{eq}} \tag{2.1}$$

where the von Mises equivalent stress is given as

$$\sigma_{eq} = \sqrt{\frac{1}{2}[(\sigma_I - \sigma_{II})^2 + (\sigma_{II} - \sigma_{III})^2 + (\sigma_{III} - \sigma_I)^2]}. \tag{2.2}$$

While the Lode parameter is used to distinguish between the three generalized stress states generalized tension, generalized shear and generalized compression for $L = -1$, $L = 0$, and $L = 1$ respectively. The Lode parameter is expressed in terms of the principal stresses as

$$L = \frac{2\sigma_{II} - \sigma_I - \sigma_{III}}{\sigma_I - \sigma_{III}} \tag{2.3}$$

To establish a generic expression for, p_f, based on findings in recent research, the value for p_f can be assumed to be path-dependent with respect to the triaxiality and Lode parameter. Mathematically such a stress state dependent critical equivalent plastic strain is expressed as

$$p_f = p_f(\sigma^*, L) \tag{2.4}$$

and based on this, the damage, D, of the material can be evaluated by a *damage accumulation rule* as

$$D = \int_0^p \frac{dp}{p_f(\sigma^*, L)} \tag{2.5}$$

where fracture occurs when D equals unity.

Lastly, it is necessary to elaborate upon some of the main assumptions behind the mathematical representation of fracture. Equation (2.4) is a surface in three-dimensional space defining the critical plastic strain for a given stress state (σ^*, L). Firstly, it must be assumed that such a reference surface even exists. Secondly, for this surface to have any practical use, some assumption regarding the extension to loading paths with non-constant stress states must be made. Loading paths where the stress state varies are called *non-proportional stress paths*. It is assumed that the failure strain in non-proportional loading cases is defined by the damage accumulation rule in Equation (2.5). Lastly, assumptions related to calibrating the reference surface must be made. Ideally, the tests used for calibration should have constant stress states. However, in practice, this is only possible for micromechanical models, while for physical material tests, the loading almost always is non-proportional. Consequently, some method to calibrate the reference surface from non-proportional loading must be used, and it must be assumed that this gives a good approximation of the surface.

In 2008, Bai and Wierzbicki published a much-cited paper where they propose a fracture model that takes into account the Lode parameter [17]. In their study, they calibrated the fracture surface using the average stress state history extracted from numerical simulations. This approach has been criticised by Benzerga [21]. Nonetheless, the hybrid method of combining experimental and numerical experiments to obtain stress state data is commonly used [22] [23] [24] [25]. In summary, fracture modelling is not straight forward, and strong assumptions must be made in order to arrive at a practically usable formulation.

2.2.4 Cockcroft-Latham Fracture Model

The *Cockcroft-Latham* (CL) criterion, proposed in 1968, is a commonly used criterion [22]. Damage is driven by plastic power per unit volume using the first principal stress, σ_1, and

accumulates only for positive values. The expression for the equivalent plastic strain to failure can be written as $p_f = W_c / \max(\sigma_I, 0)$, where the principal stress can be related to the stress state. The surface represented by this function is illustrated in Figure 2.4. The expression for the criterion then becomes

$$\omega = \frac{1}{W_c} \int_0^p \max(\sigma_I, 0)\, dp \tag{2.6}$$

and has only a single parameter that needs to be calibrated, namely, W_c. The integral in Equation (2.6) is referred to as the plastic work, W. This is a strength when considering that the fracture criterion can be calibrated based on very few tests. However, this is a weakness if the ductility of the material has a strong stress state dependence, as the model does not allow for any calibration of the stress state dependence.

2.2.5 Extended Cockcroft-Latham Fracture Model

Motivated by recent research showing that the ductility of some materials has a strong dependence on the Lode parameter, Gruben et al. extended upon the CL criterion with two additional parameters to allow calibration of Lode dependence in 2012 [22]. In their formulation, the influence of the maximum shear stress, $\sigma_I - \sigma_{III}$, is included as a second term. The model is referred to as the *Extended Cockcroft-Latham* (ECL) criterion and expressed as

$$\mathrm{D} = \frac{1}{W_c} \int_0^p \left\langle \phi \frac{\sigma_I}{\sigma_{eq}} + (1 - \phi) \left(\frac{\sigma_I - \sigma_{III}}{\sigma_{eq}} \right) \right\rangle^{\gamma} \sigma_{eq}\, dp \tag{2.7}$$

where W_c defines the overall ductility of the material, ϕ controls the relative influence of the major principal stress and the maximum shear stress, and γ governs the strength of the stress state dependence [22].

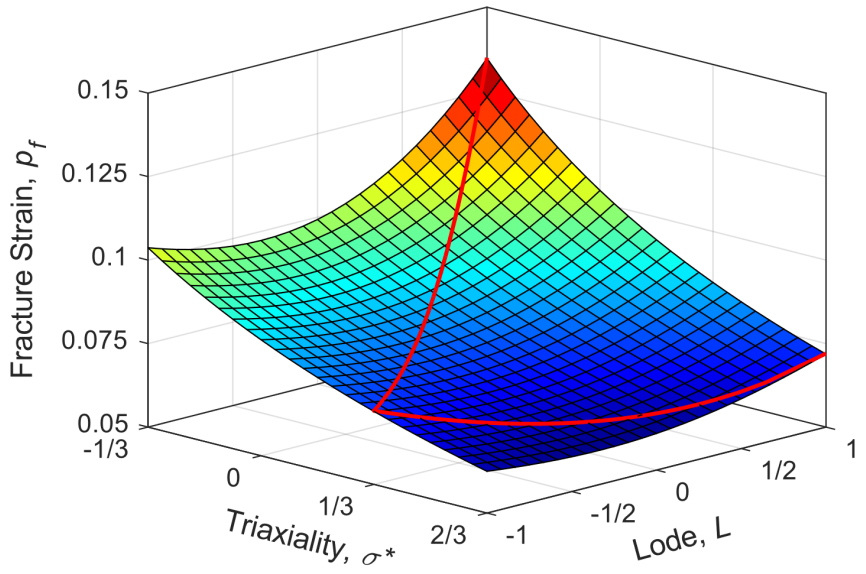

Figure 2.4: Cockcroft-Latham fracture surface showing the equivalent plastic strain at failure for different stress states.

By expressing the principal stresses in terms of the triaxiality and Lode parameter using Equation (2.1) to Equation (2.3), substituting these into Equation (2.7) and setting D equal to unity, a form of the criterion that can be used to determine a fracture surface is obtained as

$$W_c = \int_0^{p_f} \left\langle \frac{\phi\left(3\sigma^*\sqrt{3+\mu^2} - 3 - \mu\right) + 6}{3\sqrt{3+\mu^2}} \right\rangle^{\gamma} \sigma_{eq} dp. \tag{2.8}$$

2.2.6 Probabilistic Fracture

The probabilistic fracture modelling approach used in the present work is based on the PhD by Knoll and extends upon the work carried out in the master thesis by Kittilsen and Swanberg [4] [9]. This section aims to derive expressions based on statistics that enable analysis and prediction making of the stochastic behaviour of a die-cast material. Most materials have homogenous properties, and it is often assumed that mechanical properties are the same at every point. This is not the case for die-cast metals, as is explained in Section 2.1. Based on limited amounts of tests, the goal is to arrive at a probability density function that with sufficient accuracy describes the stochastic properties of the material.

Total or partial failure of a component occurs when the weakest point of the component or region fails, and a crack propagates, causing an entire region or component to fail. For die-cast materials, such weak points are distributed randomly across the material volume. The starting point obtaining equations for this phenomenon is a mechanical chain subjected to tensile forces. It is clear that as soon as one of the links fail, the chain cannot transfer forces anymore, and has failed. The chain is only as strong as the weakest link.

Three main assumptions have to be made to simplify the statistical analysis. Firstly, the material defect is considered as a point defect. Secondly, the spatial probability distribution of the material defect is uniform, and lastly, all material defects are statistically independent [9].

The chain of length l_Ω is considered to be homogenous and with links considered as continuous points x_i along the chain. It is assumed that that the chain has n weakest links Q_i. By the second assumption, the probability density function to find a defect is given as $g_{Q_i}(x_i) = 1/l_\Omega$. Then the probability of finding at least one weakest link Q_i in segment Λ is $P_F^\Lambda = 1-(1 - l/l_\Omega)^n$ and by taking the limit as l_Ω approaches infinity this can be rewritten as $P_F^\Lambda = 1 - e^{-cl}$ where $c = n/l_\Omega$. P_F^Λ is the probability for the segment to fail under loading, which is increasing with the length of the segment and the number of critical defects along the segment. Accordingly, the failure probability of a material volume V within the total volume V_Ω is expressed as

$$P_F^V = 1 - \left(1 - \frac{V}{V_\Omega}\right)^{n_c(f)} \tag{2.9}$$

where instead of using n to denote the critical links along a chain, $n_c(f)$ gives the number of critical defects that are distributed across the volume V_Ω for the given loading f. The addition is that the number of defects that have become critical is a function of the loading on the material

volume. Taking the limit as V_Ω approaches infinity is $P_F^V = 1 - e^{-c(f)V}$ where the density of critical defects across the volume is given as

$$c(f) = \frac{n_c(f)}{V_\Omega}. \tag{2.10}$$

Instead of the second assumption stated previously, the spatial probability distribution of the material defect can be taken as the Weibull density function, which is the best-known empirical density function for this application. The Weibull distribution function is expressed as

$$c(f) = \frac{1}{V_0}\left(\frac{f}{f_0}\right)^m \tag{2.11}$$

by Knoll, giving an expression for the failure probability by Weibull as

$$P_F^V = 1 - \exp\left(-\frac{V}{V_0}\left(\frac{f}{f_0}\right)^m\right). \tag{2.12}$$

The parameters V_0, f_0, and m can be found experimentally. V_0 is commonly taken as the gauge volume of the specimen, leaving f_0 and m to be calibrated based on repeated material tests. The influence of these parameters is shown in Figure 2.5.

Firstly, it can be seen that m represents the variance or scatter in the fracture behaviour, as with the increase of the m value, the variability decreases. The lower the scatter, the more likely it is that failure occurs around the reference load f_0. Secondly, as the volume considered, V, increases compared to the reference volume V_0 the probability of fracture occurring for a load lower than the reference load increases. This is expected, as it is more likely that a large sample of a material volume contains a critical defect, compared to a small volume.

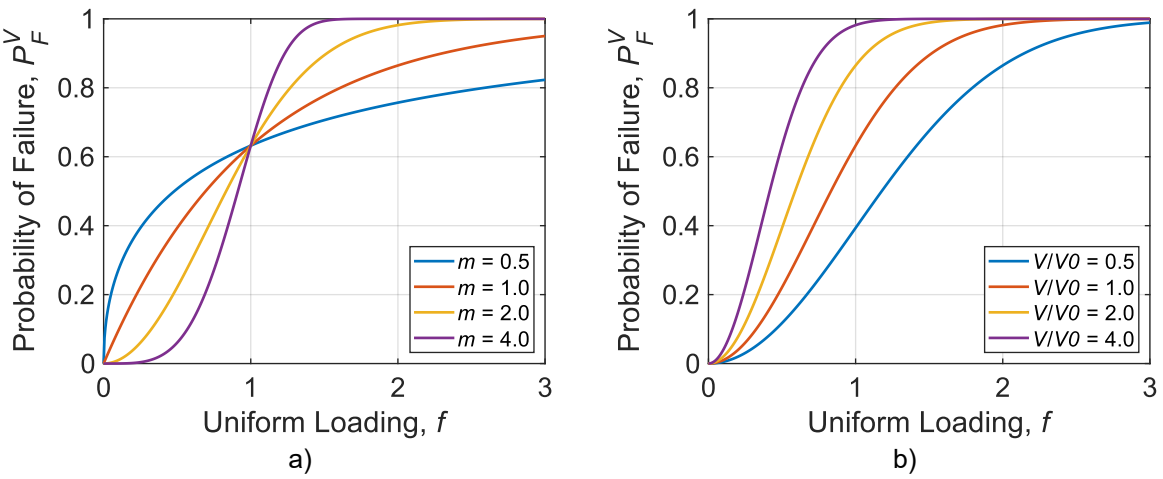

Figure 2.5: Probability of failure for different values of the Weibull distribution, a) different values for m and a constant value $V/V_0 = 1$, b) different values for V/V_0 and a constant value $m = 2.0$. $f/f_0 = 1$ in both cases.

The *probability density function* (PDF) can be expressed as

$$g(f) = \frac{\partial c(f)}{\partial f} V e^{-c(f)V}. \tag{2.13}$$

In FEM the evaluation of fracture parameter in Equation (2.6) happens at the element integration points, as will be further explained in Section 2.4. Instead of a critical load for each element, the critical Cockcroft-Latham parameter W_C is used to determine when an element fails. The equations presented previously can be changed by substituting W and W_0 for f and f_0. Expressing Equation (2.12) on this form

$$P_F^V = 1 - \exp\left(-\frac{V}{V_0}\left(\frac{W}{W_0}\right)^m\right). \tag{2.14}$$

In summary, Equation (2.14) can be used to obtain parameters for a Weibull distribution used to assign critical fracture values W_c for the elements in the FE model. The approach has a dependence on the element volume, which is consistent with what is known about defects in die-cast materials. An example of what such a PDF is shown in Figure 2.6.

2.2.7 Combined Material Model

The equations that constitute the combined material model are shown in Figure 2.7. These equations describe the different phenomena observed in die-cast material, including the elastic and plastic behaviour and the pseudo-random fracture characteristics. To the author's knowledge, the only published research where a stress state dependent fracture criterion has been calibrated for a die-cast material is by Lee et al. [25]. In order to calibrate this model, 15 material parameters need to be determined. Some are well known and can be taken from literature, while others are largely uncertain and require extensive material testing to be accurately determined.

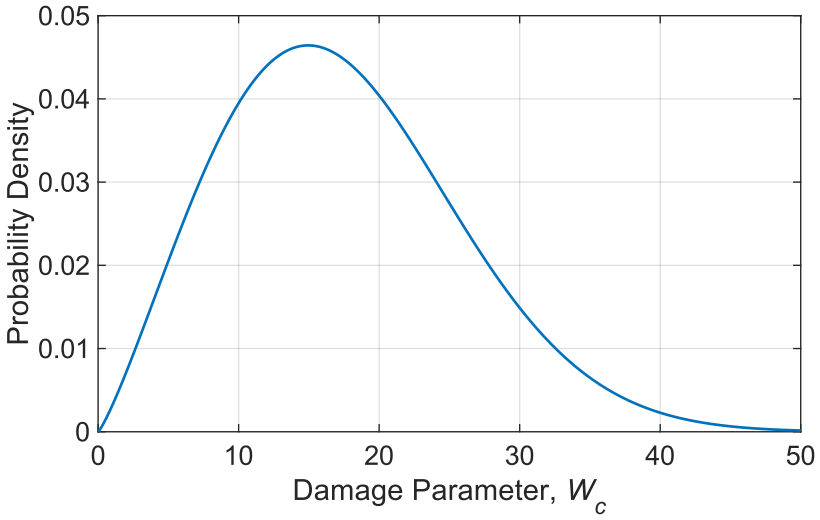

Figure 2.6: Example of a Weibull PDF used to assign critical damage parameters to elements in a FEM model.

1. Additive decomposition:

$$\boldsymbol{d} = \boldsymbol{d}^e + \boldsymbol{d}^p$$

2. Linear hypoelasticity:

$$\boldsymbol{\sigma}^{\Delta J} = \left(K - \frac{2}{3}G\right) tr(\boldsymbol{d}^e)\boldsymbol{I} + 2G\boldsymbol{d}^e$$

$$K = \frac{E}{3(1-2\nu)} \quad and \quad G = \frac{E}{2(1+\nu)}$$

3. Isotropic von Mises yield criterion:

$$f(\boldsymbol{\sigma}, p, \dot{p}) = \sqrt{\frac{3}{2}\boldsymbol{\sigma}' : \boldsymbol{\sigma}'} - \left(\sigma_0 + R(p, \dot{p})\right) \leq 0$$

4. Isotropic Voce hardening rule and Norton creep law:

$$R(p, \dot{p}) = \left(\sum_{i=1}^{2} Q_i(1 - \exp(-C_i p))\right)\left(1 + \frac{\dot{p}}{\dot{p}_0}\right)^C$$

5. Associated flow rule:

$$\boldsymbol{d}^p = \dot{\lambda}\frac{\partial f(\boldsymbol{\sigma}, p, \dot{p})}{\partial \boldsymbol{\sigma}} = \frac{3\dot{\lambda}}{2\sigma_{eq}}\boldsymbol{\sigma}' \quad \text{where} \quad \dot{\lambda} = \dot{p} = \sqrt{\frac{3}{2}\boldsymbol{d}^p : \boldsymbol{d}^p}$$

6. Loading/unloading conditions:

$$f \leq 0, \quad \dot{\lambda} \geq 0, \quad \dot{\lambda} f = 0$$

7. Extended Cockcroft-Latham fracture criterion:

$$\mathrm{D} = \frac{1}{W_c}\int_0^{\bar{\varepsilon}^p} \left\langle \phi\frac{\sigma_I}{\bar{\sigma}} + (1-\phi)\left(\frac{\sigma_I - \sigma_{III}}{\bar{\sigma}}\right)\right\rangle^{\gamma} \bar{\sigma}\, d\bar{\varepsilon}^p$$

8. Fracture parameter Weibull PDF:

$$g(W, V) = \frac{\partial c(W)}{\partial W} V e^{-c(W)V} \quad \text{where} \quad c(W) = \frac{1}{V_0}\left(\frac{W}{W_0}\right)^m$$

9. Material parameters:

$$[E, \ \nu, \ \sigma_0, \ Q_1, \ Q_2, \ C_1, \ C_2, \ \dot{p}_0, \ C, \ W_c, \ \phi, \ \gamma, \ V_0, \ W_0, \ m\,]$$

Figure 2.7: Isotropic hypoelastic-plastic material model, including strain rate effects, and stress state dependent and probabilistic fracture, neglecting thermal effects [9] [12] [15] [26].

2.3 Material Parameters from Previous Work

Material parameters taken from Kittilsen and Swanberg, and Dahler and Thuve are listed in Table 2.1. The yield stress of the spoke material was changed by Dahler and Thuve, based on new UT60 tests carried out in 2019. Dahler and Thuve also performed dynamic Split-Hopkinson tension tests in order to obtain the strain rate sensitivity parameters. The remaining parameters were calibrated by Kittilsen and Swanberg [4] [6].

2.4 Finite Element Method

Although a primary focus is directed at the material mechanics aspect of the numerical rim model, the numerical formulation with respect to FE-formulation can be just as important to establish an accurate rim model. Here some central notions in explicit nonlinear FEM are reviewed.

2.4.1 Time Integration

In order to solve the governing equations of structural dynamics, the time interval must be subdivided into time increments. To solve these equations in FEM the central difference scheme is employed, where the nodal displacements for each time increment are calculated based on the nodal values at the previous time step. This method is referred to as explicit FEM. Because there is no equation solving, the method becomes only conditionally stable, and a small time step is needed to obtain an accurate solution. The approximation for the stable time step for the simulation is obtained as

$$\Delta t \leq \alpha \min\left(\frac{h_e}{c}\right) \tag{2.15}$$

where h_e is the characteristic dimension of element e, α is the Courant number, and $c = \sqrt{E/\rho}$ is the current wave speed in the material [13]. Because a large number of time increments is needed, explicit FEM usually makes use of the lumped mass matrix, making each time step computationally inexpensive.

Explicit FEM is particularly suited for the analysis of transient dynamics problems, such as structural impacts. For structures or components modelled with a large number of *degrees of freedom* (DOFs) and subjected to impact loading and large plastic deformations, the method is the preferable choice [27]. Implicit FEM might struggle or never converge to such problems.

Table 2.1: Voce hardening and Norton creep law parameters from Kittilsen and Swanberg, and Dahler and Thuve [4] [6]. *Changed from 181.3 MPa to 200.0 MPa by Dahler and Thuve.

	$\sigma_0\ [MPa]$	$Q_1\ [MPa]$	$C_1\ [-]$	$Q_2\ [MPa]$	$C_2\ [-]$	$\dot{p}_0\ [-]$	$C\ [-]$
Spokes	200.0*	84.2	15.7	47.3	177.2	$5 \cdot 10^{-4}$	0.00718
Rim Bed	208.2	86.2	17.8	30.8	239.6	$5 \cdot 10^{-4}$	0.001

2.4.2 Mass Scaling

Mass scaling is a convenient method to decrease the simulation times of quasi-static analyses. Mass scaling is a means of artificially increasing the material density. As stated in Eq. (2.15) the critical time step is proportional to the root of the material density, and thus increasing the density leads to a larger critical/stable time step. Caution must be taken when employing mass scaling, as too much mass scaling may introduce inertial forces to the problem. It is therefore important to make sure that the kinetic energy remains low relative to the internal energy. As a rule of thumb, the kinetic energy should not be more than 10% of the internal energy [28].

Mass scaling can be implemented in several ways. The simplest method is to increase the density of the material for all elements in the model. Alternatively, the desired time step can be specified. Mass is then added automatically by the FE-code to an element as soon as its stable time step is reduced below the specified time step. Mass is added so that the critical time step of the element is equal to the specified time step. This is referred to as *automatic mass scaling*.

2.4.3 Element Formulation

Appropriate element selection requires knowledge about the available element formulations and greatly depends on the problem at hand. This subsection aims to review essential aspects of element selection in FEM and is based mainly on the lectures by professor Kjell Magne Mathisen at NTNU and the introductory FEM book by professor Kolbein Bell [29].

The rim model can be classified as an impact problem using explicit FEM. This already imposes some direction to the element selection. Firstly, in explicit FEM, it is advisable to avoid the use of higher-order elements since they have higher frequencies than lower-order elements and might produce noise when stress waves propagate across the mesh [27]. Secondly, analysis of impact problems often requires the element to retain its accuracy for large deformations. Thirdly, LS-DYNA represents fracture by eroding the element, removing its stiffness contribution and mass from the analysis. Consequently, a fine mesh and a large number of elements is required to capture fracture accurately. This means that a simple and efficient element formulation, such as elements using reduced integration, is desirable. Lastly, due to the complex geometry, it must be considered what type of element gives the best representation of the geometry without the expense of accurate element behaviour.

Due to the limiting factors imposed by the numerical solution method used in explicit FEM, the element selection leads towards the use of the simplest types of solid elements, the four-node tetrahedral element and the eight-node brick element. These elements have trilinear interpolation functions used to evaluate the stresses and strains, both shown in Figure 2.8 alongside the four-node shell element.

The stiffness of the element is evaluated by the integral $\boldsymbol{k} = \int_V \boldsymbol{B}^T \boldsymbol{C}\boldsymbol{B} dV$ where $\boldsymbol{B}$ is the strain-displacement matrix obtained from the shape functions and $\boldsymbol{C}$ is the elasticity matrix relating stresses and strains. This integral must be evaluated numerically. How this is done affects the element characteristics. The two main methods used are referred to as *full integration,* and *reduced integration*, which refers to the quadrature rule used to calculate the integral. A

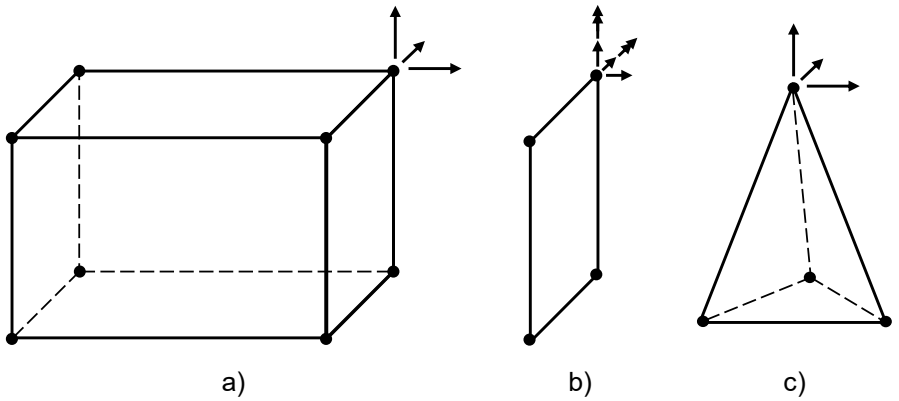

Figure 2.8: Basic elements types, a) eight-node brick, b) shell, c) constant strain tetrahedral.

combination of the two is referred to as *selectively reduced integration.* Full integration uses a quadrature rule that evaluates the integral exactly, while reduced integration uses one less integration point in each direction compared to full integration. Reduced integration might lead to spurious energy modes and deformations of the element that do not affect the strain energy. By this, it is meant that for some modes of deformation, the strains at the integration point become zero, thus the element has no stiffness against these deformations. This is called hourglassing and is illustrated in Figure 2.9. Some means to control these modes are needed to obtain a stable solution.

The element that is commonly used to model impact problems in the automotive industry is the eight-node brick element with reduced integration [30]. Typically, the brick element formulation is preferable to the tetrahedral formulation since tetrahedral elements typically suffer from more defects. However, for complex geometries, the generation of a mesh consisting of brick elements might be very challenging. Geometric simplifications or highly distorted elements might be the only way to achieve a mesh. Tetrahedral elements are far more suited to represent complex geometries, but the standard formulation has the defect of volumetric locking for nearly incompressible deformations [30]. The problem of volumetric locking must be overcome when the tetrahedral element is to be used in a model that includes fracture. This is because volumetric locking can cause checkboard pattern strain fields that cause premature element failure. A remedy for this problem, and a possible alternative to the reduced integration eight-node brick element, is the average nodal pressure four-node tetrahedral element proposed by Bonet and Burton [30]. This element is implemented in LS-DYNA as ELFORM = 13 and was developed specifically for explicit dynamic applications.

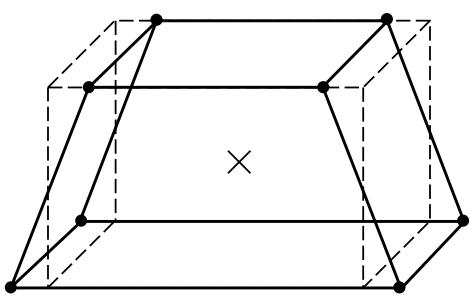

Figure 2.9: Hourglass mode of the reduced integration eight-node brick element.

2.4.4 Contact Definition

Correct numerical representation of contact between different part, surfaces or nodes is crucial in impact simulations, especially for brittle material such as the die-cast aluminium. This is because the concentration of contact forces depends on the contact stiffness. If the contact stiffness is too high, then unrealistic large forces are transferred to a few nodes of the model, and fracturing can more easily occur.

Contact definition begins with defining sets of so-called slave and master nodes. At every time step, an algorithm is employed to check for any penetration of a slave node into the surface defined by the master nodes. Figure 2.10 shows a two-dimensional representation of a slave surface partially penetrating a master surface.

The *penalty method* is a commonly used method of implementing contact in numerical models. In the penalty method, a force proportional to the depth of penetration is applied to the penetrating nodes, to counteract the penetrations [31]. This is analogous to the compression of a series of springs, where further compression of each spring leads to a larger force in the opposite direction. The penalty-based contact can be expanded by using a so-called segment-based contact algorithm. This replaces the node-to-segment treatment of contact with a between-segment contact treatment. A segment is meant as the surface that is made up between a number of nodes. This treatment leads to an improved and more realistic distribution of forces in the contact area [31].

2.4.5 Shell-to-Solid Coupling

In hybrid meshes where both shell and solid elements are used, careful thought has to be put into the interface between the two. Shell elements have rotational DOFs while solid elements typically do no. Therefore, it is necessary to include some means to transfer the rotation of the shell elements to the brick element. This can be done either by a surface to surface contact coupling between an edge-based shell surface and an element based solid surface, or by transfer of rotation through the coupling of multiple translational DOFs. In the latter method, the rotation of one shell node is transferred to a minimum of two solid nodes, which is analogous to transferring a moment by a pair of forces. This is illustrated in Figure 2.11 where the shell part is split into a “Y-shape” at the end, where it interfaces with the solid elements. This way, the rotation of the shell part is transferred to the solid part. Figure 2.11 a) and Figure 2.11 b) show the coupling methods referred to as *simple coupling* and *full coupling*, respectively.

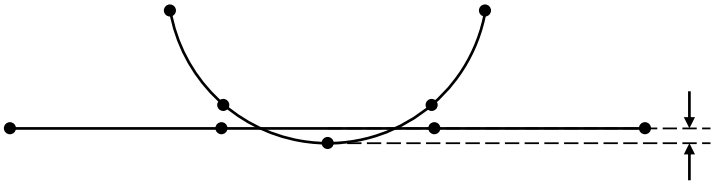

Figure 2.10: Contact between two surfaces, where the curved surface is the slave surface and the flat surface master surface, penetration depth is indicated by the arrows.

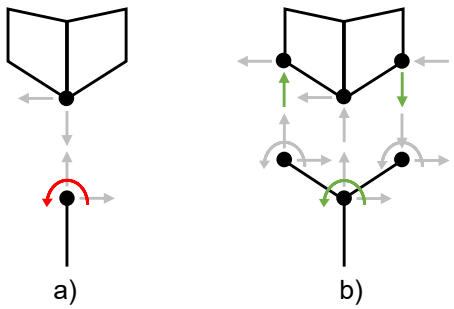

Figure 2.11: Shell-to-solid coupling types, a) single node coupling between shell and solids, *simple coupling*, resulting in no moment transfer, b) multiple node coupling between shell and solids, *full coupling*, resulting in moment transfer by a pair of forces.

2.5 Rim Model from Previous Work

An S-B rim model was previously established in Abaqus by Kittilsen and Swanberg. In order to replicate the varying thickness along the rim bed, the model was split into several shell sections. These shell sections were in turn given different thicknesses, roughly corresponding to the actual thickness of the rim at the given locations. The rim bed was split into 15 different segments. The spokes were modelled with reduced integration brick elements.

2.6 Measurement Tools

2.6.1 Load cell

Load cells are force transducers that rely on the relations between force, material deformation and the flow of electricity. The load cell has one end attached to a base and one free end that is attached to the part where force is measured. As force is applied at the free end, the body of the load cell flexes. A strain-gauge circuit is bonded to this body, and its electrical resistance is altered when it deforms. Since this relation and the material properties of the body of the load cell are well-known, the force acting upon the free end can be obtained [32].

2.6.2 Laser

Laser distance sensors typically measure distance by the *triangulation principle*. The sensor emits a laser beam that is reflected by a surface. The triangulation principle uses the angle that the reflected beam returns to the sensor to calculate the distance. Alternatively, the distance can be measured based on the time it takes for the emitted signal to return to the sensor [33].

2.6.3 Digital Image Correlation

Digital image correlation (DIC) is a technique for measuring the deformation fields based on a series of images captured during the deformation of an object. An optimisation scheme is used to correlate each image to the reference image at specified image coordinates. The tracking of

points can be helped by applying a speckle pattern or some other markers that create contrast in the image. Typically, monochrome greyscale images are used, with a single value per pixel representing its light intensity. Theory from FEM can be used to obtain deformation fields where inter-nodal strains are approximated by interpolation. The element formulation of the Q4 element is the most basic formulation that can be used to obtain a continuous deformation field. The advantage of this method compared to other methods of deformation measurement is that it results in a deformation field, rather than a single measure between two points. DIC can, however, also be used to measure the vector elongation between two points, which means it can be used a virtual extensometer [34]. The software used in the present work is named eCorr and developed by Egil Fagerholt at SIMLab, NTNU.

Chapter 3

Methods

3.1 Material Tests of Spokes

A series of new material tests were performed in order to calibrate the ECL fracture criterion and the Weibull parameters. All specimens were loaded to the point of fracture. The physical tests were performed by Tore Andre Kristensen at SINTEF.

3.1.1 Specimens

Four different types of specimens were machined from two different long spokes, both taken from the same rim. UT60, NT10, NT335 and ISS-Venkat specimens with a thickness of 2 mm were used. UT and NT are commonly used abbreviations for *uniaxial tension* and *notched tension,* respectively. Figure 3.1 and Figure 3.2 show the locations from which the specimens were extracted. Dimensions for each specimen can be found in Figure A-1.

Figure 3.1: Location of specimen extraction, NT10 to the left and NT335 to the right.

Figure 3.2: Location of specimen extraction, UT60 to the left and ISS-Venkat to the right.

3.1.2 Test Set-up

The instrumentation and test set-up were the same for all specimens. A camera facing the specimen in the test rig was used to capture the deformation of the specimen. Figure 3.3 illustrates the main components for the test set-up and shows the mounting of the camera used for DIC. The camera was oriented so that the entire gauge section is captured. The camera captured images of the speckle pattern that was painted on the specimens before testing. In post-processing, a virtual extensometer was placed between the edges of the gauge section, as shown in Figure 3.3. The elongation measured was then used to calculate the displacement of the gauge section. Figure 3.4 shows the speckle pattern from one of the UT60 specimens. Additionally, for all NT10, NT335 and ISS-Venkat specimens, a 40 mm clip extensometer was mounted over the gauge section, with the exception of the first NT10 test.

Each end of the specimen was mounted to the testing machine with a pin, where one pin was fixed, and the other pin moved at a constant velocity during testing. Force was measured by the built-in load cell of the testing machine. Quasi-static loading conditions for each of the specimens required different loading speeds in terms of the velocity of the moving pin. Loading velocities for the specimens were $0.6\,mm/min$, $0.1\,mm/min$, $0.065\,mm/min$ and $0.015\,mm/min$ for the UT60, NT10, NT335 and ISS-Venkat specimens respectively.

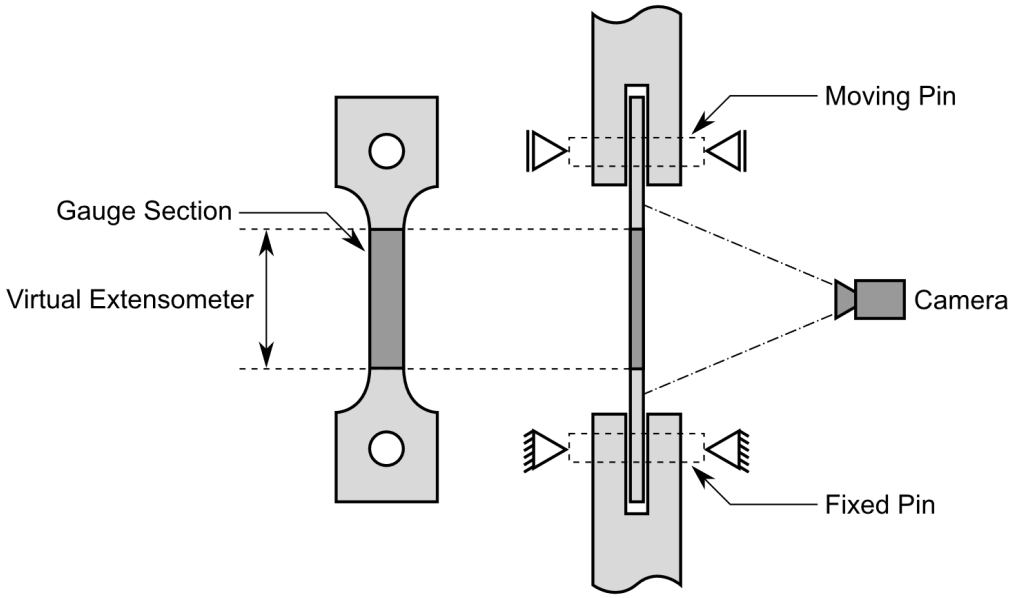

Figure 3.3: Test set-up used in material testing, illustrated with a UT60 specimen.

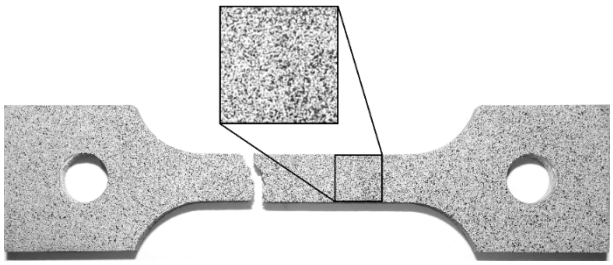

Figure 3.4: Speckle pattern painted on a material specimen used for DIC.

3.2 Fracture Parameter Identification of Spokes

Based on old and new material tests, calibration of the material parameters related to the ECL fracture criterion and Weibull distribution was attempted. In both cases a hybrid approach was used, meaning that experimental results were combined with results from a corresponding numerical simulation. Before these parameters could be identified, the hardening parameters of the material had to be validated.

3.2.1 Validation of Hardening Parameters

The experimental data from the UT60 specimens were used to calibrate the Voce hardening parameters in the MJC material model. Calibration was carried out using the in-house software, MatPrePost, developed at SIMLab the host research group of SFI CASA. The parameters were then compared to the values obtained by Kittilsen and Swanberg in 2017, and to those obtained by Dahler and Thuve in 2019 [4] [6].

3.2.2 Numerical Specimen Models

A numerical model of each of the specimens was created in Abaqus CAE, with the use of the MJC material model and fully integrated brick elements, C3D8. The meshes used in each of the models are shown in Figure 3.5. Quasi-static loading conditions were applied through a ramped velocity at the end nodes of the specimen. The Abaqus/Implicit solver was used.

The hybrid approach was used to obtain stress state histories from the numerical simulations. Because fully integrated elements were used, the stress state was taken as the average of all integration points. The stress state was taken from the critical element, which is the element with the highest plastic work, W, at the point in deformation where the physical specimen fails. This is most typically the centre element, which is what was used for all specimens. Out of the three specimens of each type, the specimen with the largest strain at failure is used, since it is the specimen where casting defects have the least impact on fracture behaviour.

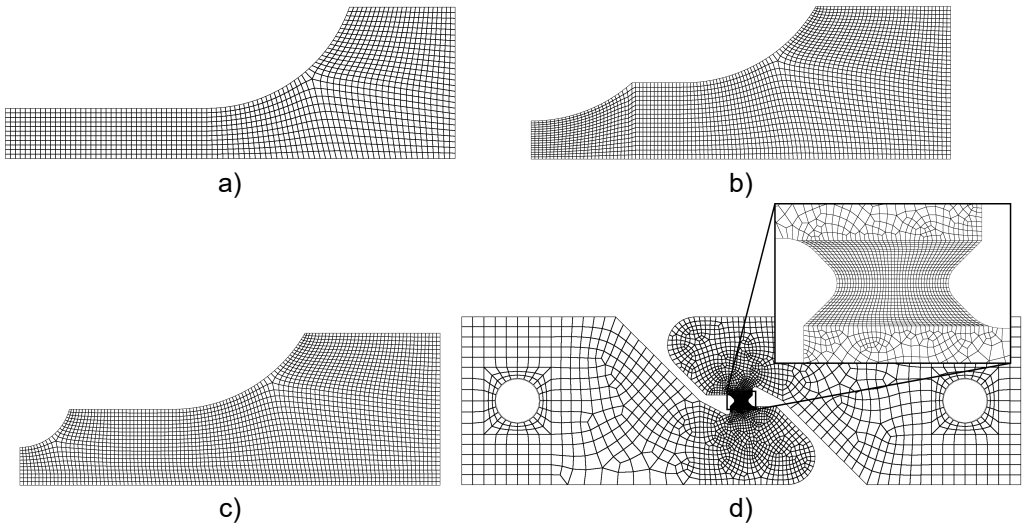

Figure 3.5: Meshes of the various specimens, a) UT60, b) NT10, c) NT335, d) ISS-Venkat.

3.2.3 Extended Cockcroft-Latham

Calibration was to be performed using a MATLAB script provided by co-supervisor David Morin. However, this was not done for reasons explained in Subsection 4.2.3.

3.2.4 Probabilistic Fracture

A combination of new and old UT60 tests was used to obtain the Weibull parameters. For all tests, a hybrid approach was used, in the sense that the plastic work, W, at failure for each of the specimens was calculated from numerical simulations. For the three new UT60 specimens, W, was calculated at the critical element by numerical evaluation of the integral in Equation (2.6). The Weibull parameters were obtained using the `fitdist` function in MATLAB.

3.3 Experimental Quasi-Static Tests

Four quasi-static tests were performed using the test rig developed by Martinsen [5].

3.3.1 Test Set-Up

For all tests, the rim was oriented with a short spoke facing the *impact wall*, which is referred to as the *short spoke configuration*. This orientation can be seen in Figure 2.3, corresponding to a top-down crushing of the rim. Contrarily, the *long spoke configuration* referrers to an orientation where a long spoke is facing the impact wall. Impact wall refers to the side of the *impact box* that is in contact with the rim, as shown in Figure 3.6, whereas the *reaction wall* refers to the fixed bottom plate. The short spoke configuration was chosen, as it was the configuration used in three out the four dynamic tests carried out by Dahler and Thuve, making a direct comparison between dynamic and quasi-static loading possible. Additionally, this configuration ensured that the rim was loaded in a symmetric manner so that it would not eject from the test rig during loading.

Although the test rig was designed for dynamic impact tests in a kicking machine, it was mounted in a $5\ MN$ Instron hydraulic jack for the quasi-static rim tests. In this set-up, the impact box of the test rig is pressed by a hydraulic cylinder. A detailed schematic of the test set-up is shown in Figure 3.6. The force applied by the hydraulic machine displaces the impact box with a constant velocity of $15\ mm/min$, which in turn crushes the rim.

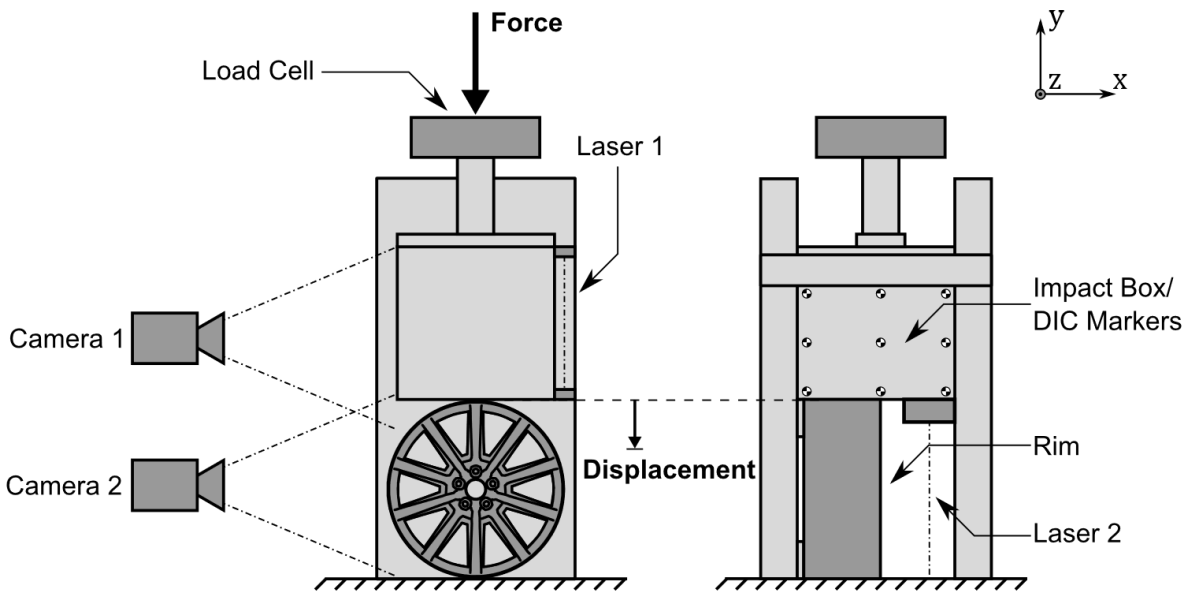

Figure 3.6: Test set-up for quasi-static rim tests, showing the placement of the various measurement tools and the placement of the rim in the test rig.

3.3.2 Measurements

The main objective was to measure the force applied to the rim and the deformation of the rim. The force was measured with an HBM-U5 500 kN load cell mounted between the hydraulic jack and the test rig, as the integrated 5 MN load cell of the testing machine was deemed not to be accurate enough. The total force applied to the rim was found by adding the weight of the 150 kg impact box to the force measured by the load cell. The deformation of the rim was measured as the displacement of the impact wall. The displacement in the negative y-direction, as seen in Figure 3.6, was measured by a MICRO-EPSILON optoNCDT 1700 laser mounted on the edge of the impact box, denoted Laser 2.

Furthermore, to investigate the elastic behaviour of the impact box, a MICRO-EPSILON optoNCDT 2300 laser was mounted at the top of the impact box, measuring the displacement relative to the bottom of the impact box, denoted Laser 1.

Finally, two Basler acA4112-30um cameras were mounted facing the rig, each with a resolution of 4,096 pixels by 3,000 pixels. Camera 1 was used to capture images of nine DIC markers that were placed on the impact box, as shown in Figure 3.6. Camera 2 was used to capture the deformation of the rims.

3.3.3 3D-DIC

For the fourth test, Camera 1 and Camera 2 were used in stereo for 3D-DIC of the rim in order to capture the displacement in the z-direction. The 3D-DIC test set-up was calibrated according to the procedure in the eCorr documentation [35]. The method is based on the principles of 2D-DIC but is extended to calculate three-dimensional deformation fields by correlating images from two separate cameras. The camera set-up for the 3D-DIC can be found in Figure A-2.

3.4 Experimental Dynamic Tests

No further experimental dynamic tests were conducted as a part of this master's thesis. Instead, the results obtained by Dahler and Thuve were used and compared with both the new quasi-static experimental tests and to dynamic numerical simulations in LS-DYNA. For this reason, a short recap of the dynamic test set-up is given here. For a more comprehensive description, the reader is referred to the thesis by Dahler and Thuve [6].

The test rig developed by Martinsen was mounted in the SIMLab kicking machine [5]. The kicking machine consists of a hydraulic/pneumatic actuator that rotates a large arm, which in turn accelerates a trolley along a guiding rail. The trolley travels along the rail until it impacts the target. In the dynamic tests, the trolley assembly had a total mass of $1407.2\,kg$, and impacted the rims at a velocity of approximately $5\,m/s$.

A complex force estimation scheme was used, as it was not possible to measure the impacting force applied to the rim directly. A load cell was placed between the trolley and the impact box. The force estimation scheme uses this force along with estimated forces from mass times acceleration of various parts of the set-up. The accelerations were then calculated by tracking the position of certain points with cameras, and the numerical differentiation of these positions. The scheme also included extensive use of filtering in order to reduce noise in the measured data.

3.5 Numerical Test Rig Models

3.5.1 Quasi-Static

The elastic deformation of the impact box was assumed to negligible compare with the deformation of the rim. In order to reduce the computational cost, and thereby time, a simplified numerical model of the test rig was developed. Only the impact wall and the reaction wall, along with the supports, was included in the model. Both the impact wall and the reaction wall were modelled as rigid shell parts. The impact wall was constrained in all DOFs apart from displacements in the y-direction, where was given a constant velocity. Furthermore, two *supports* were modelled to keep the rim from moving in the z-direction.

3.5.2 Dynamic

A dynamic rig model was developed to be used in LS-DYNA, based on the Abaqus model by Dahler and Thuve as well as the measurements of the physical test rig [6]. Figure 3.7 shows various components that make up the numerical model.

Different element types and material models were used for the various parts of the test rig. The *trolley* was modelled using rigid reduced integration brick elements. The *load cell* and *nose* were also modelled with reduced integration brick elements, but with an elastic-perfectly plastic material model. The *impact plate* is composed of two parts, both with brick elements and

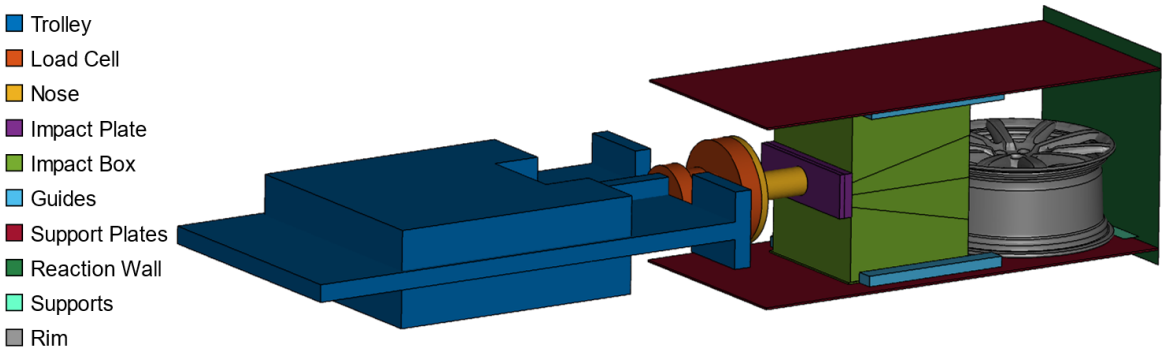

Figure 3.7: Dynamic LS-DYNA model.

elastic-perfectly plastic material models. The part of the impact plate in contact with the nose was modelled with a significantly lower density and yield strength, in order to act as a buffer introducing some damping to the system. This is explained in detail in the thesis by Dahler and Thuve [6]. The impact box was modelled with shell elements, with thicknesses corresponding those of the physical impact box, and with an elastic-perfectly plastic material model. The *guides* were modelled with reduced integration brick elements and an elastic-perfectly plastic material model. The *support plates* were modelled with reduced integration brick elements and a rigid material model. The reaction wall and the supports were modelled with rigid shell elements.

In order to obtain the correct behaviour, some boundary conditions were applied to the test rig. The reaction wall and the support plates were fixed, and the trolley, the load cell and the impact box were given an initial velocity of $5\ m/s$.

3.6 Validation of Test Rig

Some test regarding the validity of the test rig was performed as a part of the present work, with special attention to the plastic behaviour of the steel cover plate of the reaction wall and the elastic properties of the impact box.

3.6.1 Energy Absorption of Cover Plate

Figure 3.7 deviates from the physical test rig in the sense that the physical test rig has a *cover plate* between the rim and the reaction wall. During the dynamic testing conducted by Dahler and Thuve, the cover plate was permanently deformed. The cover plate was pressed into two holes in the reaction wall. These holes have since been filled to eliminate this problem in the quasi-static rim tests. To determine the impact this has on the dynamic experimental results, material tests of the plate and dynamic numerical simulations of the test rig were performed. An illustration showing the cover plate and the holes in the reaction wall is found in Figure A-3. A numerical simulation was performed in order to approximate the relative influence this deformation had on the experiments.

Four UT200 specimens were machined from an undeformed plate, identical to the cover plate. The specimen thickness was 2 mm. Machine drawing of this specimen is found in Figure A-4. In order to determine the anisotropic properties of the material, two specimens machined in the horizontal direction, and the other two in the vertical direction. The test set-up is identical to what is shown in Figure 3.3, also with the use of DIC to measure the strains. All tests were performed by Vidar Hjelmen at SINTEF.

For each of the tests, a true stress vs plastic true strain curve was generated, and an average curve of all the tests was calculated. The Voce hardening law was then fitted to this curve using the Curve Fitting Toolbox in MATLAB. In order to validate the obtained parameters, a numerical simulation of the UT200 specimens was performed in Abaqus, with the MJC material model.

Finally, dynamic simulations were carried out with a modified version of the dynamic numerical rim model described in Subsection 3.5.2, where the cover plate and the holes in the reaction wall were included. The cover plate was modelled with the MJC material model calibrated from the UT200 material tests.

3.6.2 Stiffness of Impact Box

To verify that the elasticity of the impact box can be neglected in quasi-static loading, and the impact box modelled as rigid, a quasi-static simulation including the impact box was run. Deformation of the impact box was measured using Laser 1 and by DIC using Camera 1, as shown in Figure 3.6. Displacements of the impact box in the simulation were measured at points corresponding to the markers used for DIC in the experiments.

3.7 Preliminary Numerical Study

In order to establish sufficiently well-behaved baseline rim models for further analysis, a preliminary numerical study was performed. As previously stated, three baseline models will be considered, one tetrahedral and two S-B models. These will hereafter be referred to as the *Tetrahedral*, *S-B Simple Coupling*, and *S-B Full Coupling* models, with the latter two differing in the coupling of the shell and brick elements, as shown in Figure 2.11. The differences in the baseline models will be further elaborated upon in Section 3.8. Among the FE modelling aspects that were review, the most important was the fracture modelling, element formulation, Young's modulus, and time and mass scaling. Additionally, this study was used to gain an overview of FEM-modelling capabilities of LS-DYNA.

3.7.1 Non-Stochastic Fracture Modelling

The response of a quasi-static Tetrahedral model using the CL fracture criterion and the average fracture parameter, $W_{c,avg}$, as obtained by Kittilsen and Swanberg was investigated and compared to experimental results [4]. Because the use of the average fracture parameter avoids the implementation of a user material, this naturally was a first step in the preliminary study.

3.7.2 Element Formulation

First, to determine the appropriate tetrahedral elements to be used in simulations of die-cast components in compression, a study on different tetrahedral element formulations in LS-DYNA was carried out. A pronounced checkboard pattern in the stress field is a known problem related to tetrahedral elements and is expected to be a problem for brittle materials. The tetrahedral formulation ELFORM = 13 and the more common ELFORM = 10 were compared with a more accurate brick element, ELFORM = 2, used as a reference. A simple compression test of a cylinder using the rim spoke material, obtained by Dahler and Thuve in 2019, was performed for each of the element formulations.

Second, to identify the most appropriate brick element, the quasi-static S-B Full Coupling model was run with the two most common brick element formulations available in LS-DYNA. These are the reduced integration ELFORM = 1 and the fully integrated ELFORM = 2. The performance of these formulations was evaluated with regards to the experimental data.

3.7.3 Validation of Mass and Time Scaling

Time was normalised so that when simulation time reaches one second, the impact wall has moved approximately $120\ mm$, the same end displacement as used in physical rim tests. In order to control the mass scaling, the automatic mass scaling feature in LS-DYNA was used. The time step of the explicit analysis was controlled using the DT2MS option in the *CONTROL_TIME STEP keyword. Various time steps were tested in order to find an appropriate value while monitoring the system energies throughout the simulation.

3.8 Baseline Rim Models

Three different baseline models were established in LS-DYNA based on the preliminary numerical study, the Tetrahedral, S-B Full Coupling and S-B Simple Coupling models. The fundamental difference between three baseline models is in the mesh and in the transition from the rim bed to the spokes, as illustrated in Figure 3.8.

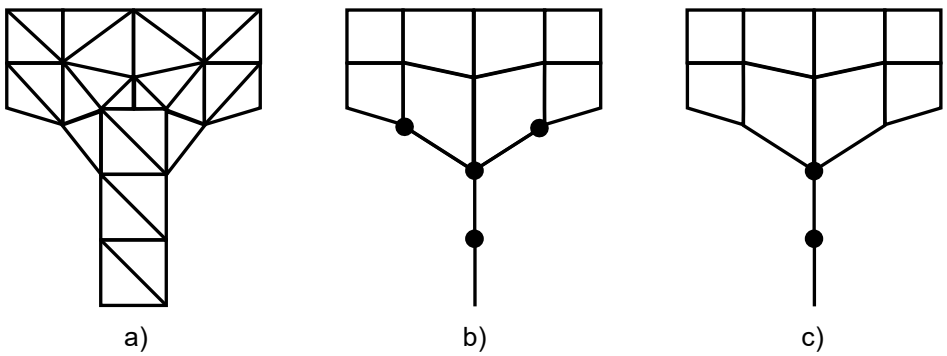

Figure 3.8: Illustration of the fundamental differences between the baseline models, a) Tetrahedral, b) S-B Full Coupling and c) S-B Simple Coupling.

Tetrahedral model refers to a model consisting of tetrahedral elements only, where no additional coupling between the rim bed and the spokes is necessary. The mesh was established by automatic meshing using LS-PrePost, a pre and post-processor delivered by LSTC.

Shell-Brick Full Coupling model refers to an improved version of the S-B Simple Coupling model where both translational and rotational DOFs are transferred at the interface between the shell and brick elements. The rotational DOFs of the shell elements are transferred as illustrated in Figure 2.11, through a pair of translational DOFs.

The Shell-Brick Simple Coupling model is equivalent to the model used in the previous work. In this model, only the translational DOFs are coupled at the interface between the shell and brick elements.

3.8.1 Material Parameters

Young's modulus, E, and the Poisson's ratio, ν, were taken from literature. The parameters of the Voce hardening law and the Norton creep law were taken from the previous work by Kittilsen and Swanberg, and Dahler and Thuve. All the baseline models were modelled with the CL fracture criterion and the average fracture parameter, $W_{c,avg}$. The non-stochastic approach was taken for the baseline models in order to decrease the number of simulations necessary, both when comparing the baseline models to each other, and when evaluating the performance of different FEM formulations. Table 3.1 lists all the material parameters that were used in the numerical baseline models. The strain rate sensitivity was only included in dynamic simulation.

Table 3.1: All material parameters used for the numerical baseline models.
*Used only in dynamic simulations.

	Spokes	Rim bed
$E\ [MPa]$	$73 \cdot 10^3$	$73 \cdot 10^3$
$\nu\ [-]$	0.3	0.3
$\rho\ [t/mm^3]$	$2.7 \cdot 10^{-9}$	$2.7 \cdot 10^{-9}$
$\sigma_0\ [MPa]$	200.0	208.2
$Q_1\ [MPa]$	84.2	86.2
$C_1\ [-]$	15.7	17.8
$Q_2\ [MPa]$	47.3	30.8
$C_2\ [-]$	177.2	239.6
$\dot{p_0}\ [-]$	$5 \cdot 10^{-4}$*	$5 \cdot 10^{-4}$*
$C\ [-]$	0.00718*	0.001*
$W_{c,avg}\ [MPa]$	9.22	39.0

3.8.2 Mesh

The meshes used for the S-B Full Coupling and Tetrahedral models are shown in Figure 3.9 and Figure 3.10. Both S-B models have the same mesh except for the added shell elements in the coupling of the S-B Full Coupling model and some minor deviations in the segmentation of the rim bed. Two types of element meshes were provided by Audi, an S-B mesh and a tetrahedral mesh. Whereas the S-B mesh required extensive manual labour, the tetrahedral mesh was obtained by automatic meshing of the rims orphan geometry. The S-B mesh was used directly, while the tetrahedral element model was remeshed using LS-PrePost, in order to reduce the number of elements. The Tetrahedral was meshed with a fine mesh, consisting of 996,271 elements. The S-B models were discretized with a considerably coarser mesh than the Tetrahedral model, only consisting of about 25,000 elements.

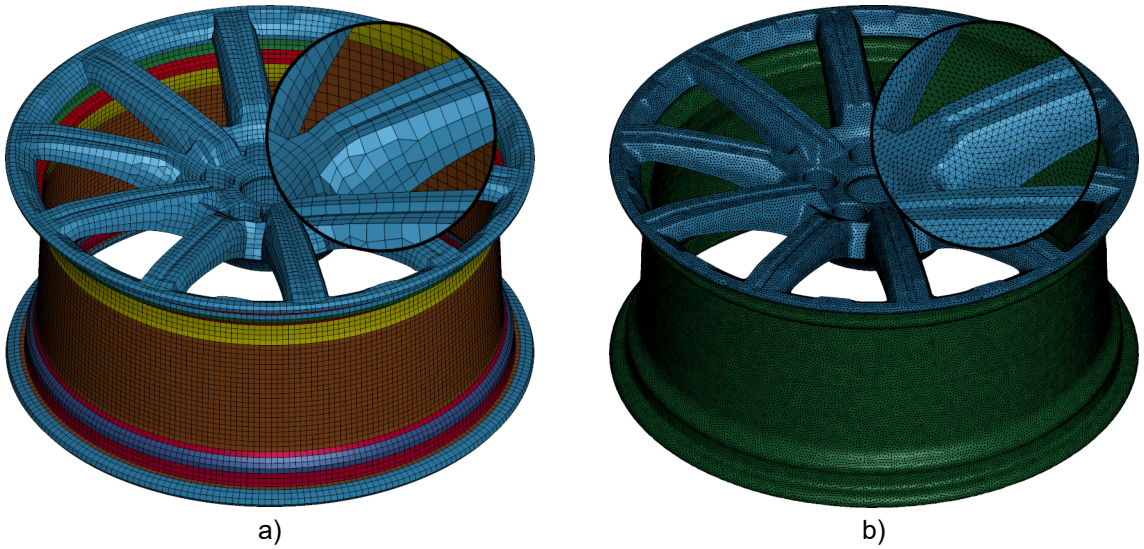

Figure 3.9: Meshes of the rim models, a) S-B Full Coupling, b) Tetrahedral.

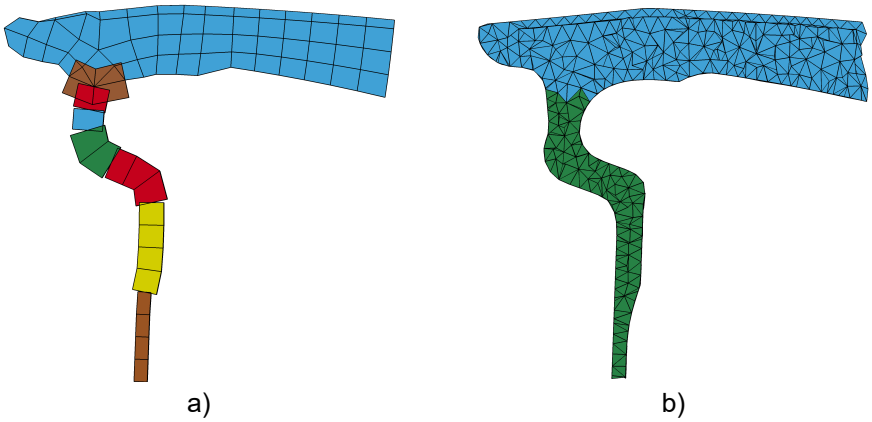

Figure 3.10: Mesh in transition area between the spokes and the rim bed, a) S-B Full Coupling, b) Tetrahedral.

3.8.3 Element Formulation

Three different element formulations were used for the baseline models. Brick elements were formulated as eight-node reduced integration solid elements. In LS-DYNA this formulation is obtained by using the keyword *SECTION_SOLID with option ELFORM = 1. Shells followed the Belytschko-Tsay shell element formulation and are selected in LS-DYNA using the keyword *SECTION_SHELL with ELFORM = 2. Tetrahedral elements were chosen to follow the trilinear and nodal pressure averaged element formulation proposed by Bonet and Burton obtained by *SECTION_SOLID and ELFORM = 13 [30]. Information about the various *SECTION keywords used and a theoretical explanation of the element formulation is found in [26] and [36].

3.8.4 Automatic Mass Scaling

Automatic mass scaling in LS-DYNA was implemented with the option DT2MS under the keyword *CONTROL_TIME STEP. In DT2MS, the desired time step is specified, and sufficient mass is added to all elements whose time step fall under this limit. For the Tetrahedral model, the time step was specified to be $3.5 \cdot 10^{-6}\ s$, while the S-B model was given a larger time step of $7.5 \cdot 10^{-6}\ s$.

3.8.5 Contact Formulation

The contact between the rim and the plates were modelled with the *CONTACT_ERODING_SURFACE_TO_SURFACE keyword in LS-DYNA, with a segment-based contact algorithm invoked by the keyword SOFT = 2. The eroding type of contact is used to remove failed elements in accordance with the fracture criteria. In order to achieve a correct contact stiffness together with the automatic mass scaling, the keyword PSTIFF = 1 was used. This formulation calculates the penalty stiffness based on nodal masses rather than material density.

To model self-contact within the rim the *CONTACT_ERODING_SINGLE_SURFACE keyword was used, also with the options SOFT = 2 and PSTIFF = 1.

3.8.6 User-Defined Material

A user-defined material including the ECL fracture criterion and a Weibull distributed fracture parameter was implemented in LS-DYNA. The user material was based on the already implemented MJC material model in LS-DYNA, *MAT_MODIFIED_JOHNSON_COOK, and has the same formulation except for the fracture formulation [26]. The Fortran code of this subroutine was written and compiled by co-supervisor Torodd Berstad.

3.9 Parametric Study

In order to better understand the performance of the Tetrahedral baseline model, a parametric study of several key modelling choices was performed. The Tetrahedral model was analysed in the parametric study, as it represents a new approach to model the rim and therefore needs to be further understood.

3.9.1 Automatic Mass Scaling

In order to assess the impact of mass scaling, several simulations were run with different amounts of mass scaling. The minimum time step was controlled so that the total mass was scaled by a factor in the range 10 to $5{,}000$. All the simulations were performed with the same time scaling factor of $1/480$.

3.9.2 Element Formulation

The performance of the ELFORM = 13, ELFORM = 10, ELFORM = 17, and ELFORM = 4 tetrahedral element formulations were evaluated. The specified termination times of the simulations were halved, as some of the element types increase the computational cost dramatically.

3.9.3 Mesh Size

In order to get a better idea of the impact of mesh refinement, simulations were run with three different mesh sizes. A coarse mesh was obtained by remeshing of the Tetrahedral baseline model and consists of $306{,}645$ elements. The original tetrahedral mesh provided by Audi was used as the fine mesh and the Tetrahedral baseline model as the medium mesh. The medium and the fine meshes consist of $996{,}271$ and $4{,}277{,}552$ elements, respectively.

3.9.4 Contact Stiffness

The impact of different scaling factors on the checkboard patterning was examined. The *scaling factor* (SF) controls the stiffness of the contact by scaling the forces in a penalty-based contact formulation. Scaling factors ranging from $SF = 0.0625$ to $SF = 1.0$ were used.

3.9.5 Fracture Parameter

To assess the impact of the average fracture parameter, $W_{c,avg}$, on the ductility of the Tetrahedral rim model, several values of $W_{c,avg}$ were tested. The values assessed were obtained by scaling the parameter obtained by Kittilsen and Swanberg in 2017, $W_c = 9.22\ MPa$, by factors in the range from 0.5 to 1.5 [4].

Furthermore, to understand how the rim behaviour is affected by the scatter in material behaviour, a probabilistic Tetrahedral model was simulated using normal distributions with

various standards deviations. The normal distribution was used for simplicity as the mean value of the distribution does not change with the variation. The standard deviation was taken from Kittilsen and Swanberg as $\sigma = 4.6425$, and scaled by factors in the range from 0.5 to 1.5 [4].

3.10 Probabilistic Fracture Model

Based on the procedures described in Section 3.2, the Weibull parameters were calibrated. Furthermore, these were used to implement a probabilistic fracture model in the baseline models. Three simulations were run for both the Tetrahedral and S-B Full Coupling models. In each case, the scatter and average behaviour was evaluated by looking at the deformation and force vs displacement history.

3.11 Extended Cockcroft-Latham

As further explained in Section 4.10, the ECL fracture criterion could not be calibrated based on the material tests. The impact of the ϕ parameter on the overall behaviour of the rim was evaluated by a parametric study. The Tetrahedral baseline model was used along with the non-stochastic fracture parameter, $W_{c,avg}$. Values of ϕ were in the range from one to zero, which is equivalent to the CL fracture criterion and the Tresca fracture criterion, respectively.

Chapter 4

Results

In this chapter, both experimental and numerical results are presented. Each subsection also includes a brief discussion of the findings. Topics that require a more comprehensive discussion are further addressed in Chapter 5.

4.1 Material Tests of Spokes

4.1.1 Validation of Specimen Dimensions

The dimensions of the specimens were measured but lost before the fractured specimens were delivered to the authors. Therefore, validation of the specimen dimensions was performed on the remaining "specimen shaped" blocks from which specimens were machined. In the thickness direction, the best measurement that could be made was of a fractured specimen in an area where little deformation had occurred. Based on these measurements, the dimensions of the specimens appeared to be accurate.

4.1.2 Force vs Displacement

The recorded force vs displacement history across the gauge area for the tested specimens are shown in Figure 4.1. Figure A-5 shows all the specimens after the point of fracture. Displacements were calculated from the DIC strains and validated by comparing the measurements to a secondary measurement by the clip extensometer. In doing this, it was observed that the noise was larger in the data from the extensometer and that the two measurements agreed well. It was concluded that the DIC measurements were accurate.

A notable scatter in the fracture strain was found for the UT60, NT10 and NT335 specimens, while for the ISS-Venkat specimen this scatter was less apparent. For the ISS-Venkat specimen, the force drops slowly to zero as the specimen gradually fails. From the recorded images, a gradual formation of cracks and partial failures across the gauge area was observed. An image of the cracks forming in the ISS-Venkat specimen is included in Figure A-6.

Although three tests are not enough to draw any conclusions about the scatter in the material properties, it appears that the scatter is similar between the UT and NT tests. Due to size effects, less scatter is expected between specimens with a smaller area of strain localization. This is indeed seen to be the case for the NT specimens compared to the UT specimens, although far more tests are required for a conclusion to be drawn.

4.1.3 DIC Measurements

Figure 4.2 shows the effective strains on the surface of the specimens, with images taken from one of the tests for each specimen. The images are the last captured frames before fracture, except for the ISS-Venkat where the frame corresponding to peak force is taken. The area of strain localisation is apparent on all the specimens and is clearly non-uniform within the weakest part of the specimens where strains are expected to localise.

As the stress fields shown in Figure 4.2 are based on DIC, the accuracy of the mesh node tracking could impact the results. Poorly tracked points may create a similar strain field since strains increase in areas where the mesh becomes distorted when the algorithm fails to track some points. However, as a similar strain field was seen in the DIC analysis of all nine UT60, NT10 and NT335 specimens it is likely that the DIC analysis correctly captures localised strains within the gauge area and does not itself introduce this as a tracking error.

The localisation of strains within the gauge area is not due to a neck forming as the material reaches its peak hardening but is seen already in the early stages of plastic deformation. The largest strained areas correspond with the location of the fracture path and are likely the point where fracture first initiated. This is then likely the location of the critical material defect.

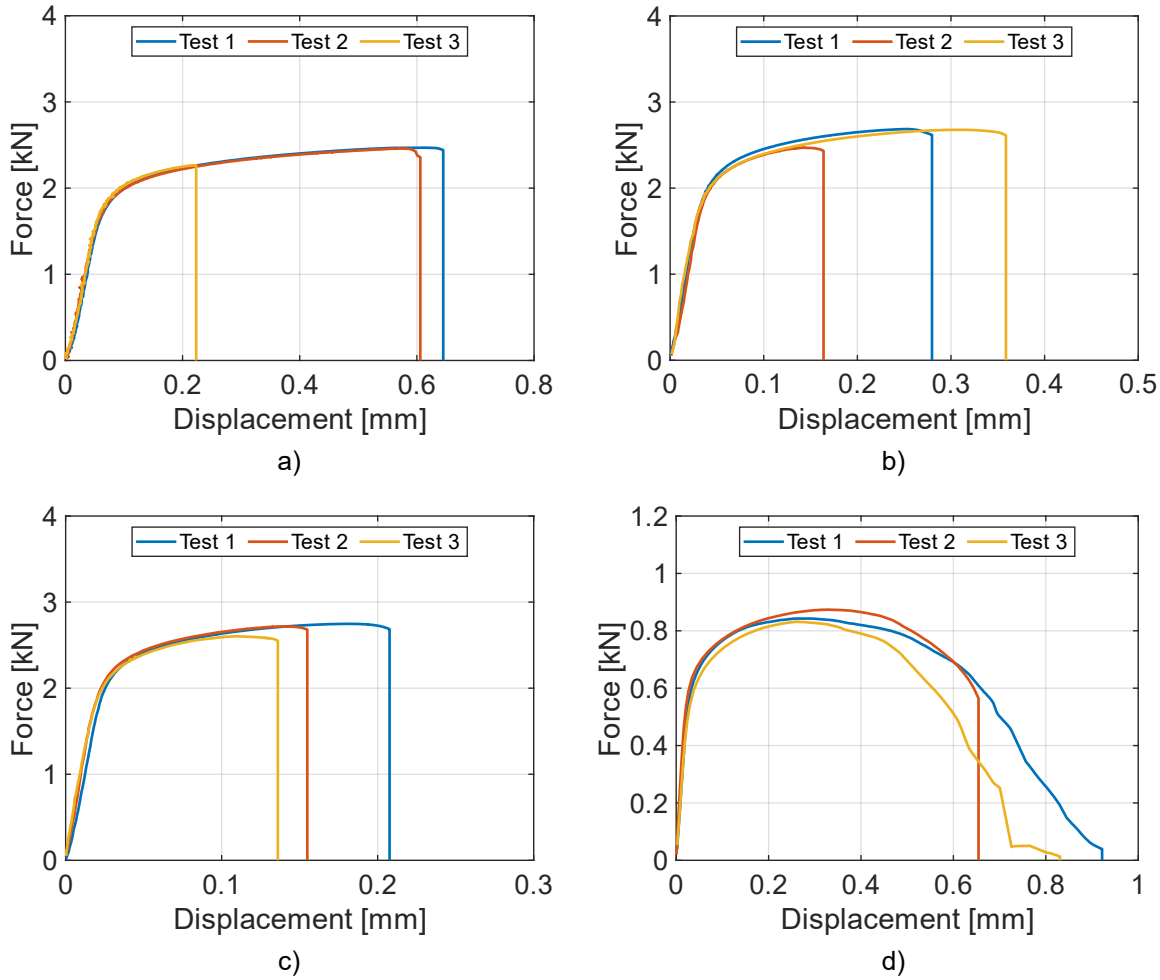

Figure 4.1: Force vs displacement for all material tests, a) UT60, b) NT10, c) NT335, d) ISS-Venkat.

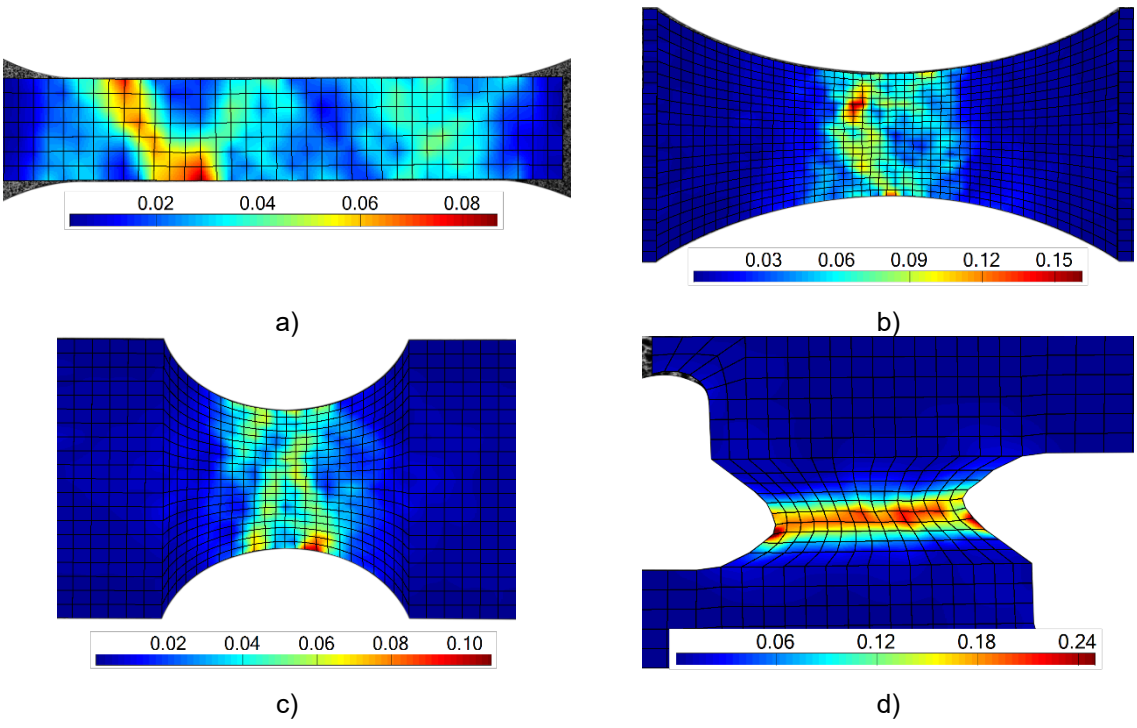

Figure 4.2: Effective strain field map taken from DIC analysis of one of the three tests performed for each of the specimens, a) UT60, b) NT10, c) NT335, d) ISS-Venkat.

4.2 Fracture Parameter Identification of Spokes

4.2.1 Validation of Hardening Parameters

To be able to use the calibrated hardening parameters, the numerical model must capture the experimental behaviour with some accuracy. A simple elastic-plastic material model with no fracture, using Voce hardening was calibrated based on the new UT60 specimens. The parameters obtained from the calibration turned out to be similar to those obtained in 2017. The parameters from 2017 were therefore used. Figure 4.1 shows the numerical results compared with the experimental tests. Based on the force vs displacement history, it is clear that the elastic-plastic material model calibrated from the 2017 UT60 tests has acceptable accuracy for all the different specimen types.

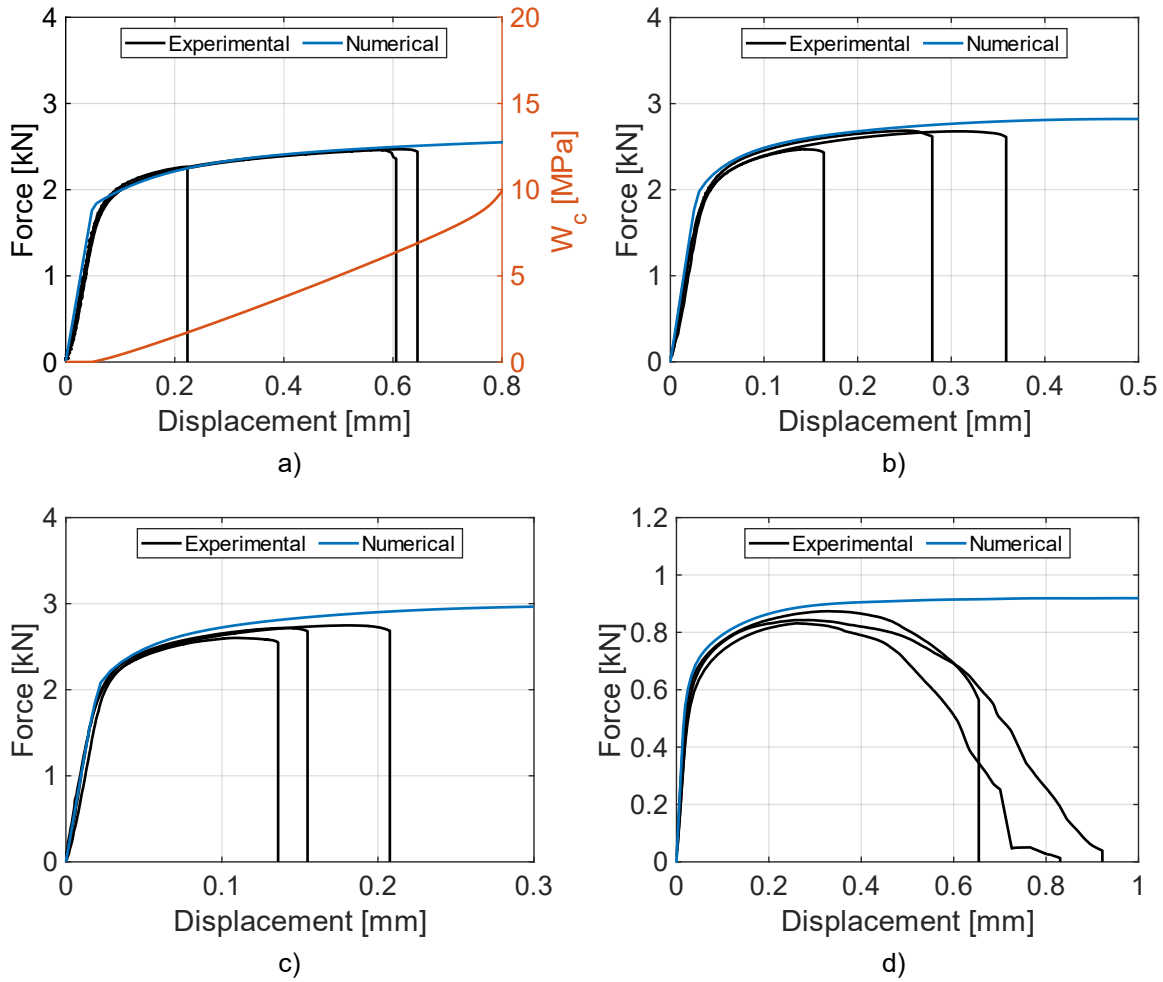

Figure 4.3: Force vs displacement for all material tests, including numerical simulations, a) UT60, b) NT10, c) NT335, d) ISS-Venkat.

4.2.2 Stress State Measurements

The stress state history was extracted from the numerical simulations and is plotted in Figure 4.4. The stress state data from the numerical simulations are plotted to the point of displacement where the most ductile specimen failed in physical experiments. This was the first, third and first test for the UT60, NT10 and NT335 tests, respectively. Since no apparent fracture occurred in the ISS-Venkat specimens, the data is plotted up to $0.48\,mm$, where the force starts to drop significantly from the peak force, and partial failure is starting to occur.

The stress states throughout the deformation of the specimens are quite constant, which means that the design of the specimen is successful in achieving close to proportional loading throughout the deformation. Furthermore, there is a good variation in the stress states between the specimens, suggesting that the selection of specimen types was appropriate. Although the stress state data is promising, the fracture strain for the different types of specimens is of concern. Most noticeable is the large fracture strain of the ISS-Venkat specimen compared to the others. Additionally, the fracture strain of the notched specimens NT10 and NT335 are larger than the UT60 specimen, which is unexpected.

With the failure strain of the NT specimens being greater than the UT specimen, the *size effect* is suspected to impact the results. In the reviewed literature, it has been stated that the fracture strain typically is reduced as the triaxiality increases. Since the NT specimens have an increased triaxiality, it is therefore expected that their ductility should decrease. However, the area where strain localizes has a significantly smaller volume in the NT specimens than in the UT specimens. This means that there is a difference in the probability of defects being present in the specimens, as a larger volume has a higher chance of containing defects. For this reason, care should be taken when interpreting these results, as it is possible that the size differences of the specimens impact the results to some extent.

4.2.3 Extended Cockcroft-Latham

Due to the influence of the size effect on fracture strain, and in turn, the stress state, it was decided that the ECL fracture criterion could not be reliably calibrated from this data. The data from the tests contradict the slope of the fracture surface, as the triaxiality of the NT specimens is greater than the UT specimen. No further attempt to calibrate the surface was made. As the calibration of the ECL fracture criterion and comparison to the CL fracture criterion was of primary interest in the present work, a further discussion of the topic is included in Section 5.1.

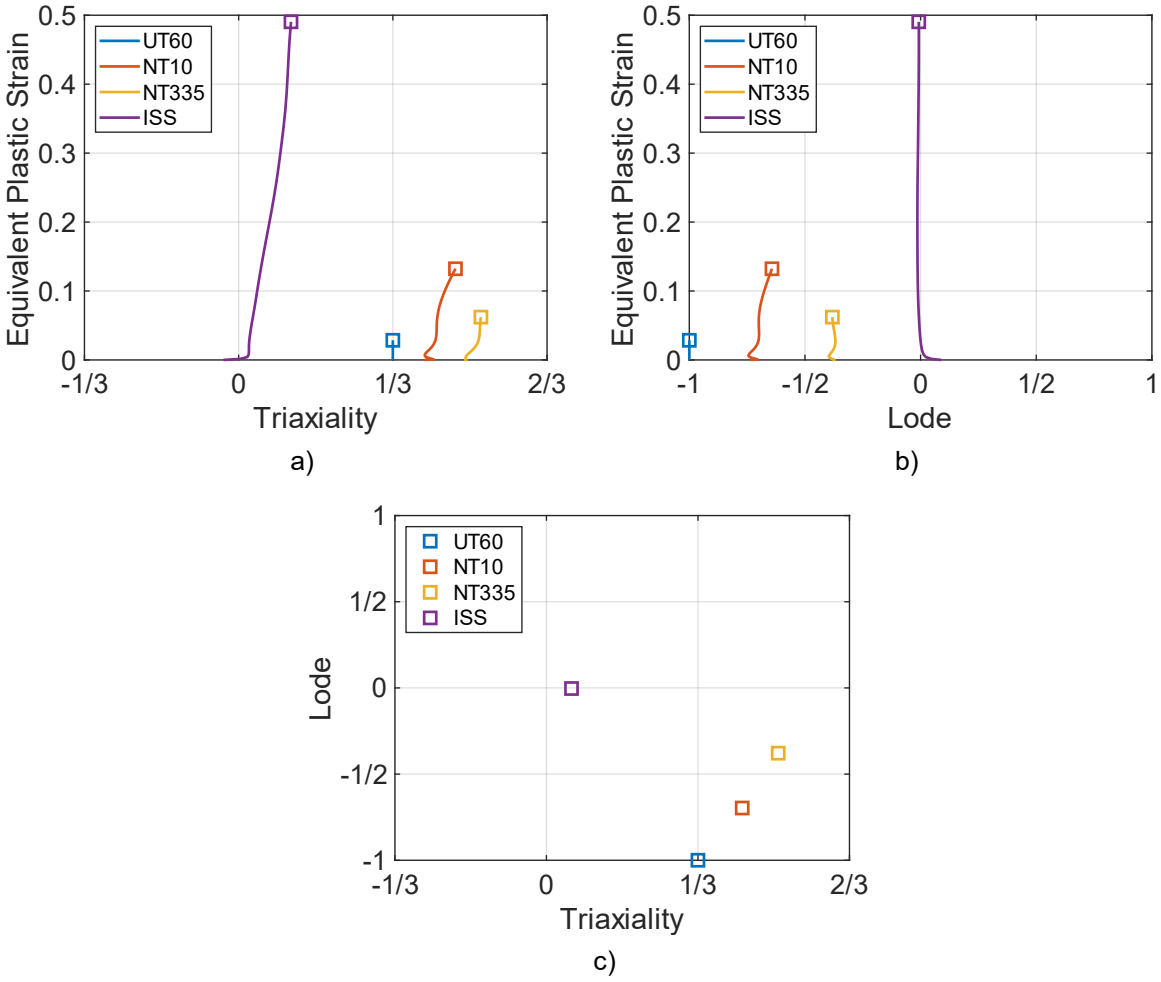

Figure 4.4: Stress state history for each of the material specimens, taken from the critical element in the numerical simulations, a) triaxiality, b) Lode parameter, c) average stress state.

4.2.4 Probabilistic Fracture

The Weibull probability distribution was calibrated by combining the result from the UT60 tests performed by Kittilsen and Swanberg and the new UT60 tests [4]. The parameters in the Weibull equation in Equation (2.14) were calibrated, and the values $W_0 = 9.87\ MPa$ and $m = 2.20$ were obtained. A histogram showing the values of the critical fracture parameter, W_c, from all the UT60 tests is plotted in Figure 4.5, along with the fitted Weibull PDF. Two additional lines are also plotted, showing the 95% confidence interval of the m parameter, which is in the range from 1.64 to 2.95.

The range of the m parameters 95% confidence interval is large due to the relatively low number of tests, as the Weibull PDF is sensitive when calibrated to a low number of tests. The variation in the probability of low values of W_c is especially noteworthy. This means that based on the tests it is highly uncertain how often a fracture parameter of less than $W_c = 5\ MPa$ will occur. Ideally, more tests should be performed to get a better understanding of the scatter in the data. However, tests are costly and difficult to machine out from a rim, and for this reason, no further tests were conducted.

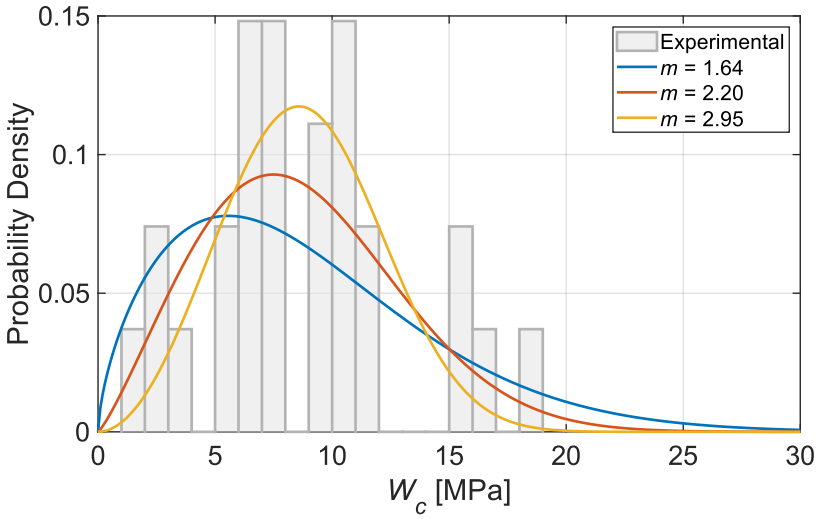

Figure 4.5: Weibull fit to the experimental values of W_c, showing the different values of the Weibull parameter m within the 95% confidence interval.

4.3 Experimental Quasi-Static Tests

4.3.1 Force vs Displacement

Due to a technical issue, the laser measuring the deformation of the rim was not activated during the first test. Instead, the deformation recorded by the testing machine was used. Based on the deviations in displacement measure between the laser and the testing machine for the second test, a method for correction of the testing machine displacement was found. This method was then validated using the third test and was applied to the first test.

The resulting force vs displacement plots for all the tests are shown in Figure 4.6. It is evident that all four rims behave similarly up to a displacement of about $50\ mm$. After the two first peaks the deformation is dominated by stochastic effects with each of the following peaks corresponding to a spoke fracture, however, in varying order for each rim. This is further discussed in Section 5.1. Figure 4.6 b) shows the mean force through the deformation. Although there are differences in the force vs displacement plots after the two first peaks, the mean force is comparable for all test throughout the deformation.

Figure 4.7 shows the deformed rims after each of the tests, and Figure 4.9 shows an image series of the third test, with markers in the force vs displacement plot. By examining the pictures of the deformation, it is seen that the first peak corresponds to shear fracture of the short spoke, that is, the spoke oriented against the impact box. The load is then transferred largely to the long spoke, and the force level increases up to another peak at which the long spoke fractures in the same manner as the short spoke. In the last frame shown in Figure 4.9 f), it is seen that fracture has initiated in the non-vertical spokes as well.

4.3.2 3D-DIC of Rim

3D-DIC was used to obtain a quantitative data of the out-of-plane displacements of the spokes, which could be used as a reference point for the deformation mode of the numerical simulations. The out-of-plane displacement fields of the fourth test are shown in Figure 4.8, where a) and b) show the displacement just before shear fracture of the short spoke and the long spoke, respectively. The short spoke buckles somewhat more than the long spoke, as evidence by the larger out-of-plane displacements. The buckling of the spokes can be recognized in the force vs displacement curves in Figure 4.6 as the tangents of the curves are decreasing just before fracture. This is seen for both the first and the second peak, although the rounding of the curve is more noticeable for the first peak. At the second peak, a more abrupt fracture occurs. This is consistent with what is seen in the 3D-DIC displacement fields.

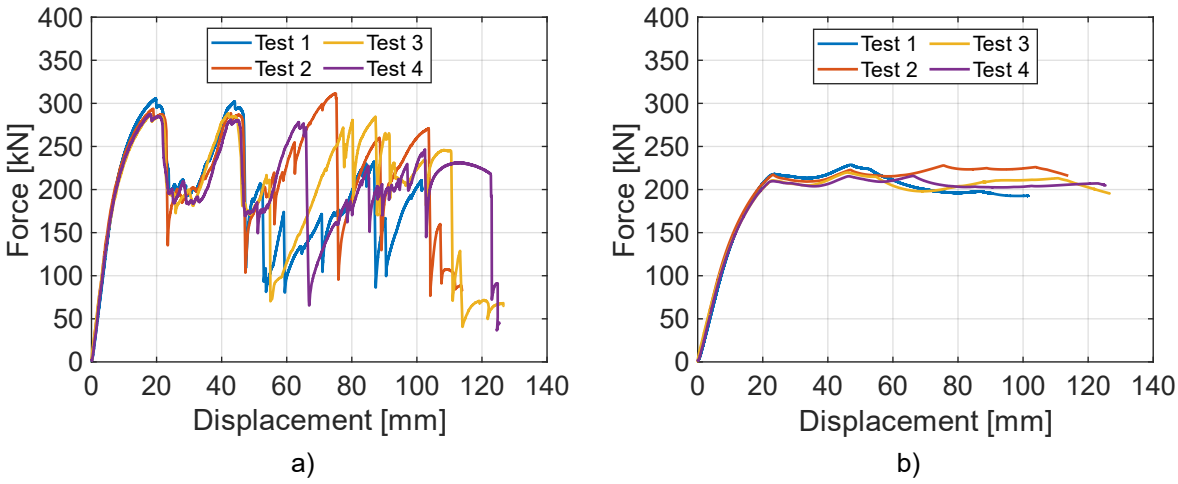

Figure 4.6: Force vs displacement for the quasi-static rim tests, a) force, b) mean force.

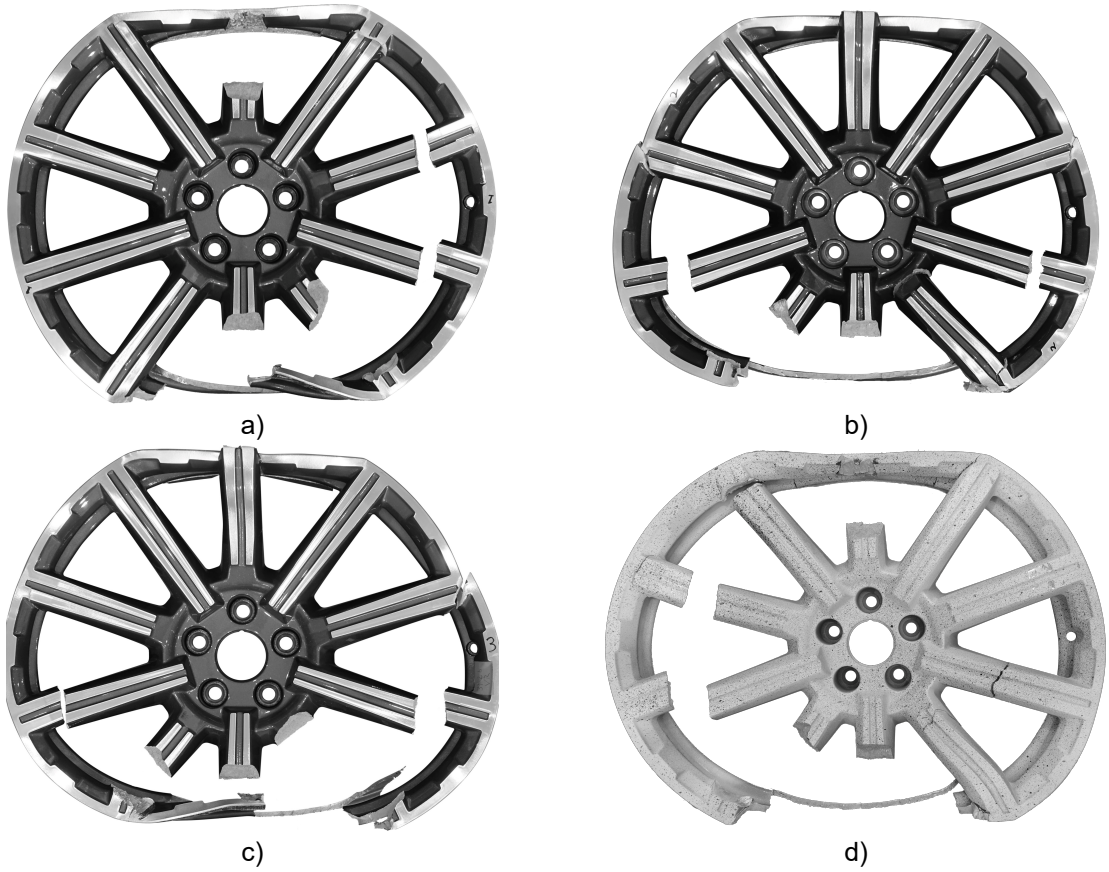

Figure 4.7: Deformed rims after the quasi-static rim tests, a) test 1, b) test 2, c) test 3, d) test 4.

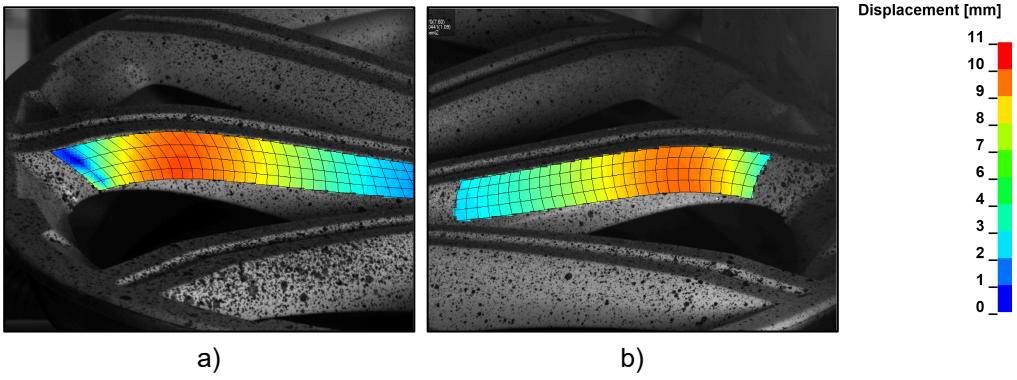

Figure 4.8: Displacement of the spokes before shear fracture, a) short spoke, b) long spoke.

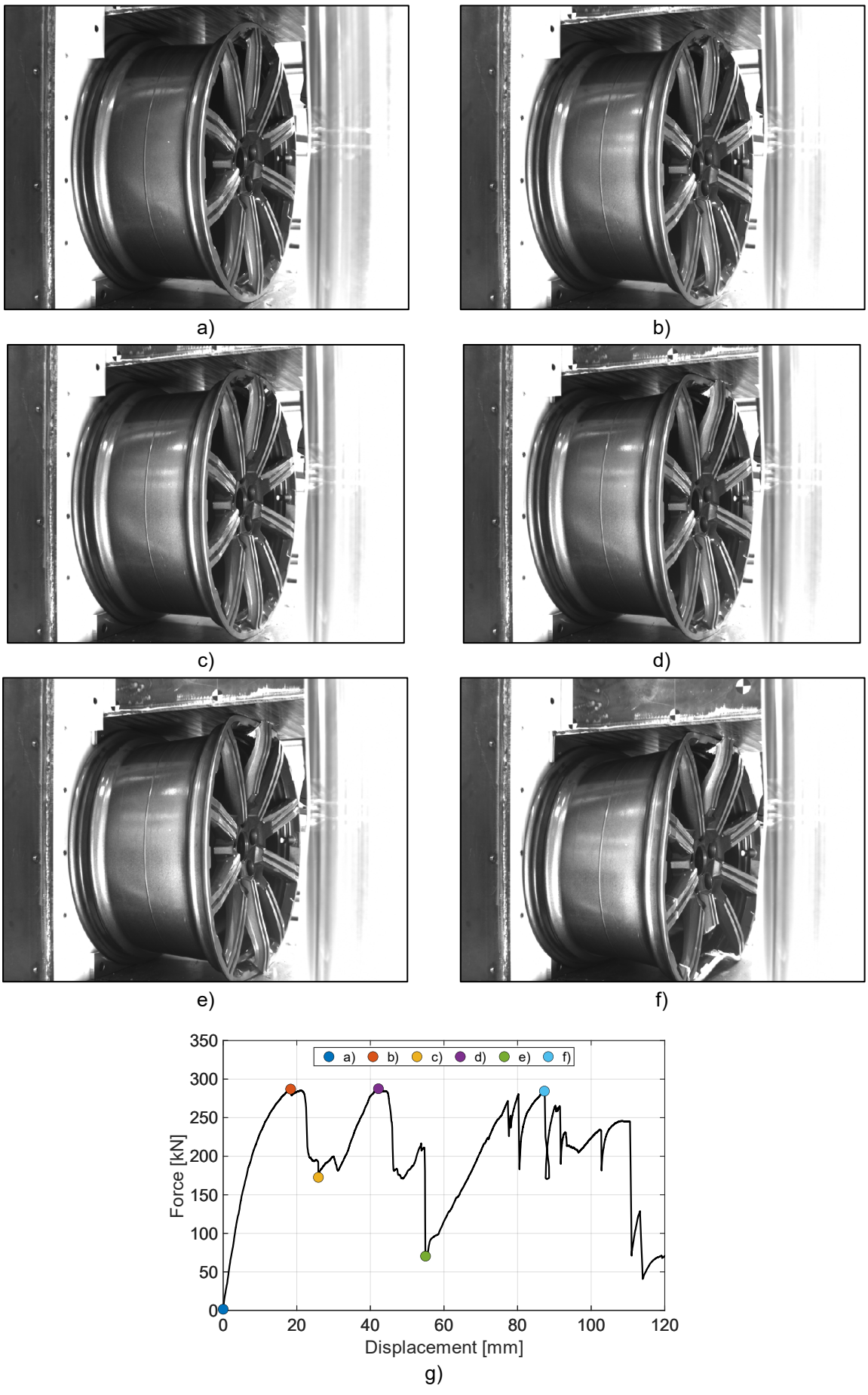

Figure 4.9: Image series and force vs displacement for the second quasi-static test, showing the deformed rims in a) to f) with corresponding force levels in g).

4.4 Experimental Dynamic Tests

4.4.1 Force vs Displacement

Force vs displacement for the dynamic tests is shown in Figure 4.10. The same trends observed in quasi-static testing are also found in the dynamic test. There are two peaks corresponding to shear fracture of the spoke facing the impact box and the reaction wall, respectively. The fourth test differs from the other tests in that the long spoke configuration was used. This orientation of the rim leads to a significantly higher first peak force, and a lower second peak force.

4.4.2 Comparison with Quasi-Static Tests

In Figure 4.11, the quasi-static and the dynamic tests are compared. The fourth dynamic test with the long spoke configuration is left out here. Some general trends can be observed in this comparison. Firstly, the peak forces in the dynamic tests are generally higher than in the quasi-static tests, which is indicative of strain rate dependence in the material. Secondly, there is significantly more scatter up to the two first peaks in the dynamic tests than in the quasi-static tests. A possible explanation is that this is due to the extensive filtering of the dynamic data. This is because raw data can be amplified in the filtering process. Lastly, it can also be observed that the peaks are more densely spaced in the quasi-static tests compared to the dynamic tests. This is unexpected. Although increased force levels can be expected for a strain-rate dependent material, it cannot alone explain why fracture occurs later in the deformation of the rim. The complex geometry, material behaviour, deformation mode and measurements techniques make it difficult to reach a definitive conclusion regarding the cause of this difference.

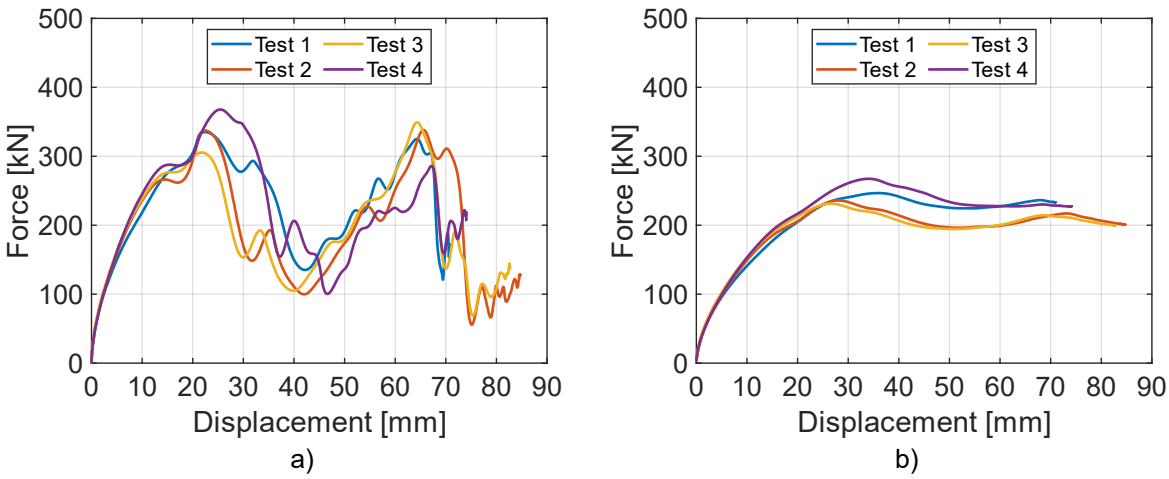

Figure 4.10: Force vs displacement for the dynamic rim tests, a) force, b) mean force [6].

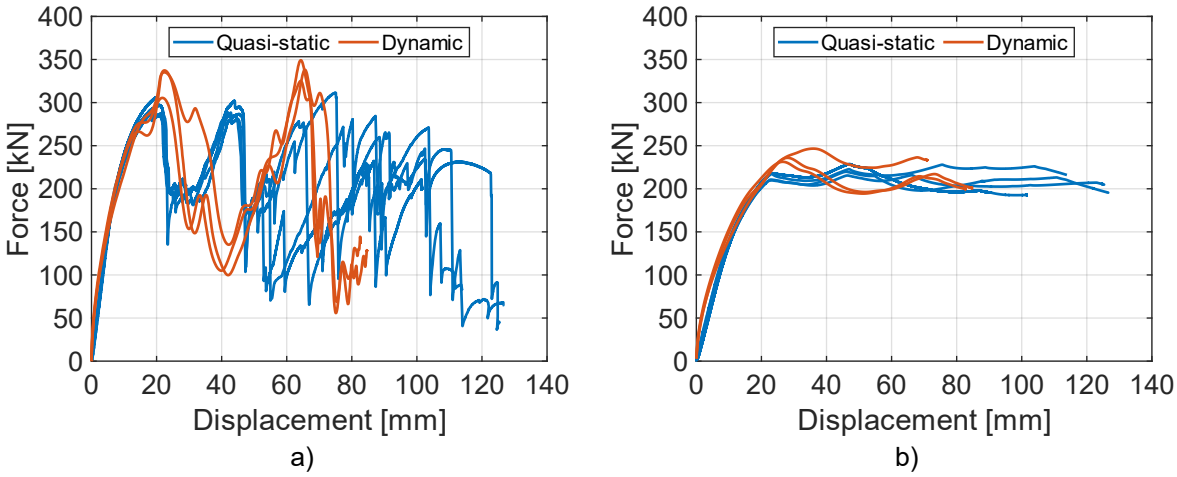

Figure 4.11: Force vs displacement for the quasi-static and dynamic rim tests, a) force, b) mean force.

4.5 Validation of Test Rig

4.5.1 Material Tests of Cover Plate

Four UT200 tensile tests were performed, two in each direction. The resulting forces are plotted against displacements measured by DIC in Figure 4.12 a). The first and second correspond to the horizontal specimens, while the second and fourth tests are in the vertical direction. Although the tests show signs of anisotropy in the material, this is determined not to be of great importance in the estimation of the energy absorption of the cover plate. The true stress vs plastic strain curves are found in Figure 4.12 b), and the resulting material parameters are listed in Table 4.1. The result from the simulation is shown in Figure 4.12 a) along with the experimental forces and displacements. The numerical curve corresponds well with the experimental tests, especially up to necking. From necking until the points of fracture in the experiments, the numerical curve is close to the specimens taken in the vertical direction.

4.5.2 Energy Absorption of Deformed Cover Plate

A simple model of the cover plate and the backplate was included in a dynamic simulation, and the energy absorption of this part is compared to the energy absorption by the rim. Figure 4.13 shows the internal energies in the rim and the steel plate as well as the total kinetic energy in the system throughout the deformation. The energy absorbed in the steel plate is seen to be vanishingly small compared to the internal energy of the rim. Not all the kinetic energy was absorbed by the rim. A significant amount was also absorbed in the impact plate, used to introduce damping to the system. The energy absorption in this part is not shown here. Conclusively, the marginal influence of the cover plate was confirmed, and further investigation of the system energy of the dynamic model is out of scope.

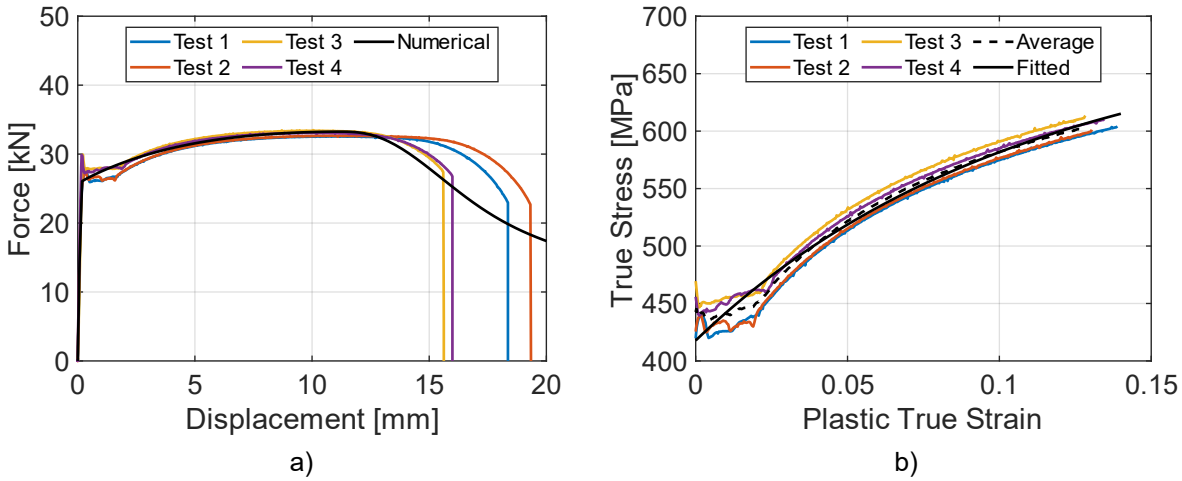

Figure 4.12: Experimental and numerical results for the cover plate, test 1 and test 2 in the horizontal direction, test 3 and test 4 in the vertical direction, a) force vs displacement b) true stress vs plastic true strain. The dashed line represents the average of the tests. The black solid line shows the fitted Voce hardening law.

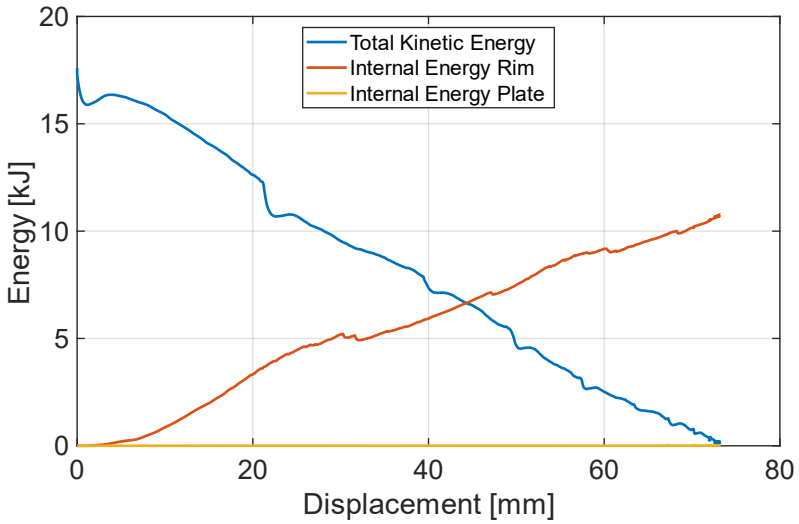

Figure 4.13: Comparison of energies in rim and test rig from dynamic numerical simulations, showing the energy absorbed by the cover plate compared to the rim.

Table 4.1: Material parameters of test rig cover plate.

$\sigma_0\ [MPa]$	$Q_1\ [MPa]$	$C_1\ [-]$	$Q_2\ [MPa]$	$C_2\ [-]$	$E\ [MPa]$	$\nu\ [-]$	$\rho\ [t/mm^3]$
417.8	242.2	10.05	538.4	0.1943	$210 \cdot 10^3$	0.33	$7.9 \cdot 10^{-9}$

4.5.3 Stiffness of Impact Box

The relative elongation of the impact box in the first three tests is shown in Figure 4.14, including DIC and laser measurements, along with numerically obtained results.

The reliability of these measurements must be discussed. The DIC measurements show largely varying values for the relative elongation and both positive and negative values. Therefore, it seems that the DIC measurements are not accurate enough to measure such small elongations. The seemingly erroneous DIC results could be because the elongation is too small to be reliably obtained by DIC, possibly because of distortions caused by the camera lens or noise affects the tracking of points in DIC analysis. When it comes to the laser measurements, the results did not seem completely reliable either. First, the exact location of the laser placement was not documented during testing. Second, in the second test, a sudden increase in elongation is observed in Figure 4.14 b). When looking at the force vs displacement for this test in Figure 4.6, a large drop in force is seen at this point. It seems likely that some forces in the test rig distorted the laser measurement to get a contestant offset value. Since this happened in the second test, it is unsure whether this impacts the other tests as well. The laser corresponds relatively well with the numerical elongations for the most part and is of the same magnitude. However, it is deemed that the elastic behaviour of the impact box in the numerical model cannot be verified based on the test data.

From the numerical simulation comparing the response of the rim when loaded by the impact box and when replaced by a rigid wall, the resulting force vs displacement plots are shown in Figure 4.15. The models closely resemble each other throughout the deformation. Although the stiffness of the impact box could not be confirmed, it is assumed that it is of the same magnitude in the numerical model and that the results shown in Figure 4.15 closely represent the physical response of the system. It is therefore concluded that for quasi-static loading, the modelling of the impact box using a rigid wall is sufficiently accurate.

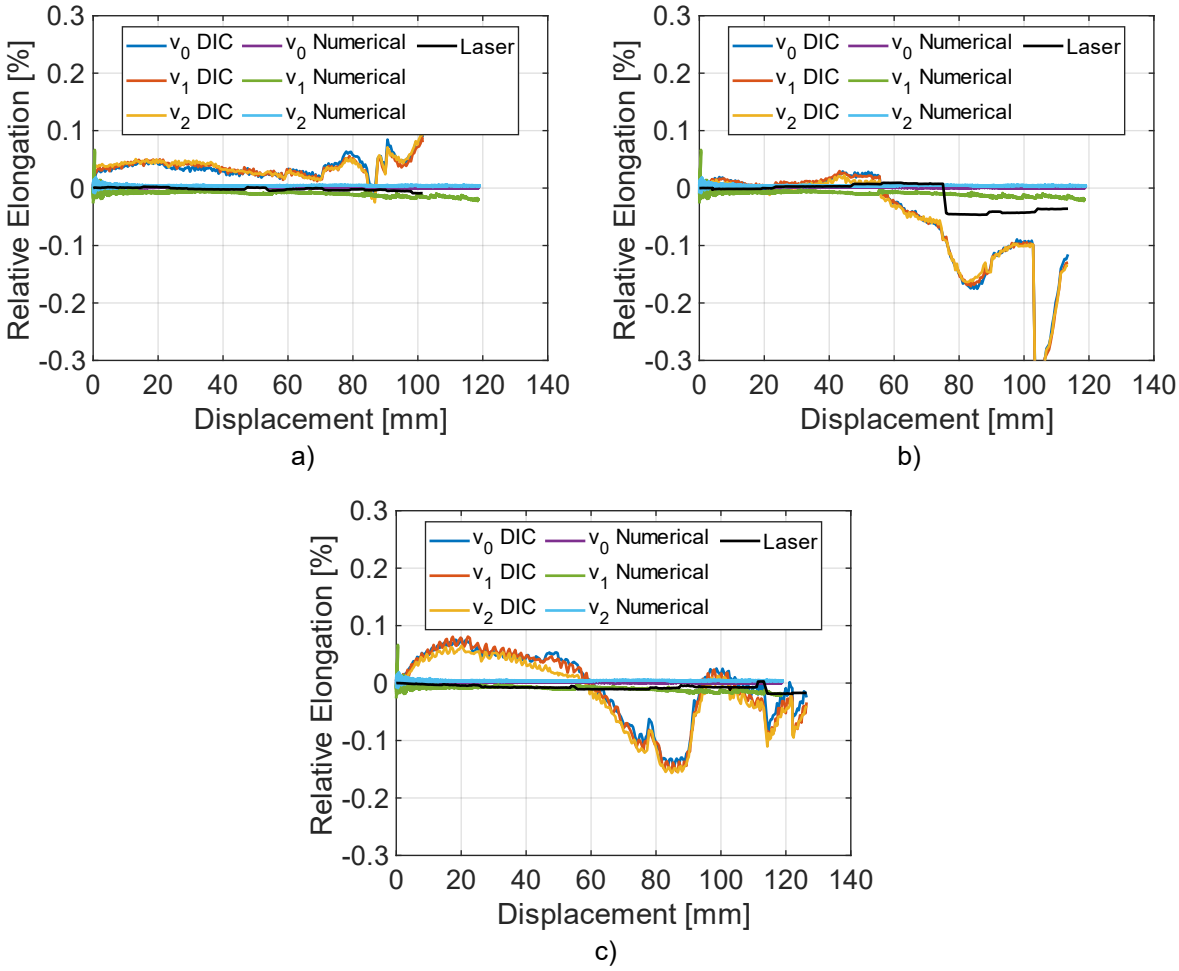

Figure 4.14: Relative elongation of impact box vs the deformation of the rim, a) test 1, b) test 2, c) test 3. Each plot shows the elongation of three vectors, experimentally and numerically, in addition to a laser measurement.

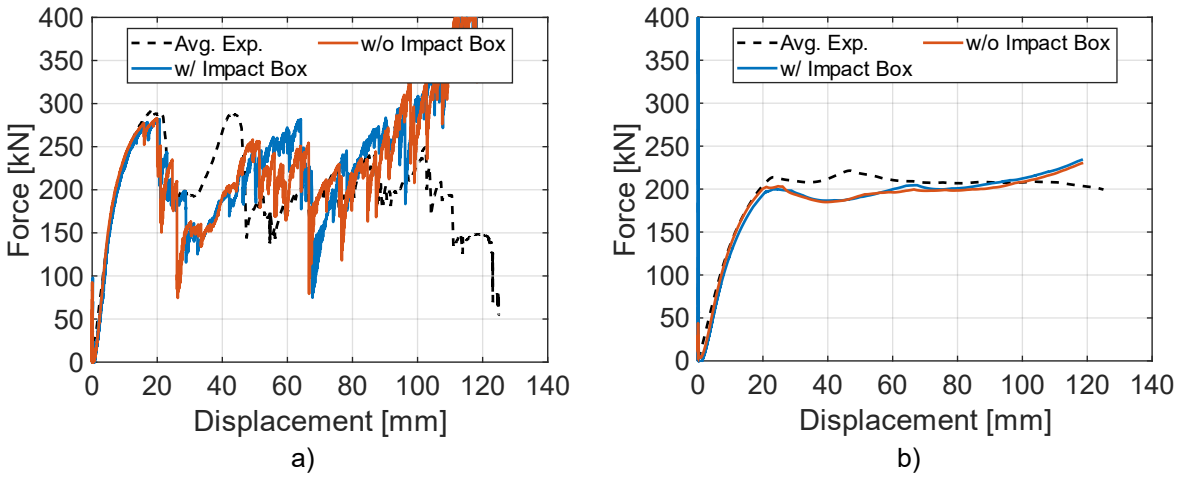

Figure 4.15: Force vs displacement for the quasi-static S-B Full Coupling baseline model, a) force, b) mean force, comparing the response with or without an elastic impact box.

4.6 Preliminary Numerical Study

4.6.1 Non-Stochastic Fracture Modelling

In early studies, the rim model using the average fracture parameter, $W_{c,avg} = 9.22\ MPa$, showed acceptable results. It was therefore used as a reference for further studies. Although this way of assigning the fracture parameter does not represent the stochastic properties of the rim, it is possible to use without implementing a user material in the FE-code. By describing the fracture behaviour in an average sense, it becomes much simpler to evaluate the impact different modelling choices have on the performance in a numerical study. Also, the first objective of the numerical analysis is to obtain a model that accurately captures the correct stiffness. Stochastic fracture modelling is a second priority, as a correct fracture behaviour can only be achieved if the stiffness of the model is described accurately. This approach can also be justified by the fact that in the early stages of deformation, very little scatter is seen in the experimental force vs displacement data.

4.6.2 Element Formulation

Figure 4.16 shows a clear checkboard pattern with ELFORM = 10 and that the performance is greatly improved with ELFORM = 13 when compared to the brick element. It is seen that a significant number of elements are eroded prematurely when ELFORM = 10 is used. While some checkboard pattern is still present with ELFORM = 13, it is greatly reduced.

It appears that in a numerical model where a brittle material is subjected to compressive loading, the checkboard pattern in the stresses becomes a large problem when fracture is included. In the CL fracture criterion, fracture is driven by the first principal stress. When a checkboard pattern occurs the tension stresses in some elements are amplified while they are reduced for neighbouring elements. This artificial amplification of tensile stresses is what leads to the premature fracture of elements seen in Figure 4.16. Therefore, it appears that for this application ELFORM = 13 is the only usable tetrahedral element type available in LS-DYNA, thanks to its nodal pressure averaging.

Figure 4.17 shows the effect of reduced and full integration on the force vs displacement history of the S-B Full Coupling model. It is observed that the fully integrated selectively reduced element, ELFORM = 2, results in much lower force level compared to reduced integration element, ELFORM = 1. The fully integrated elements thereby display too brittle behaviour, where elements are prematurely eroded. The differences between these two elements will be discussed further in Section 5.5 with regards to full-scale simulations.

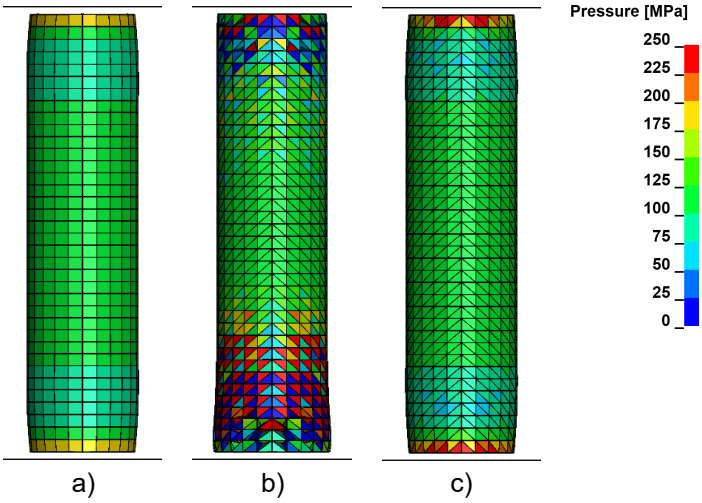

Figure 4.16: Pressure field from a cylinder compression test with a) selectively reduced integration brick element (ELFORM = 2), b) one point constant stress tetrahedral element (ELFORM = 10), c) one point constant stress tetrahedral element with nodal pressure averaging (ELFORM = 13).

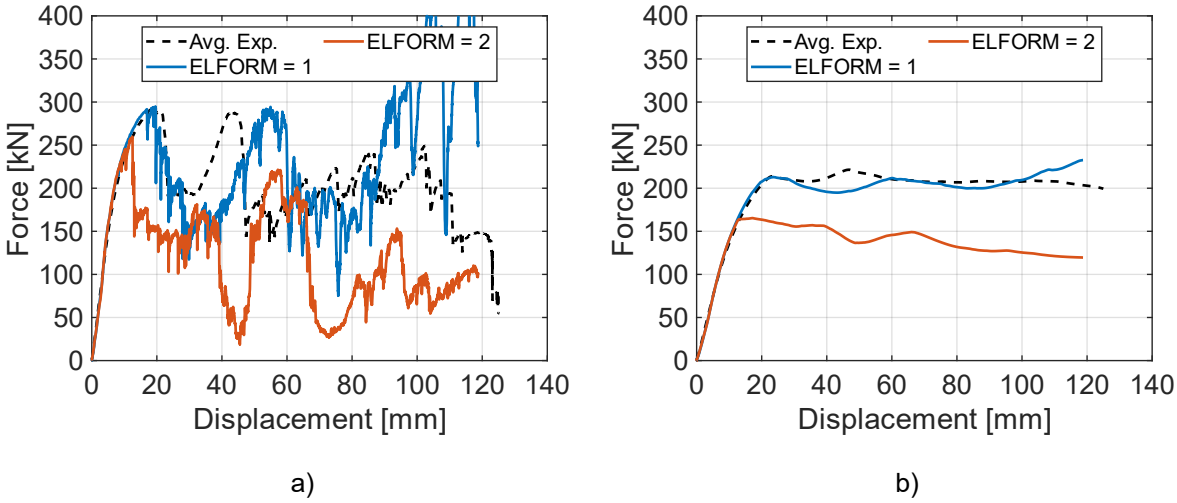

Figure 4.17: Force vs displacement for the quasi-static S-B Full Coupling baseline model, a) force, b) mean force, comparing the response for the selectively reduced integrated brick element, ELFORM = 2 and the reduced integration element, ELFORM = 1.

4.6.3 Young's Modulus

In 2017 Kittilsen and Swanberg calibrated the Young's modulus, E, from the UT60 specimens. To calibrate the Young's modulus from tensile tests requires highly accurate measurements, and according to good practice, generally requires a separate test set-up, with dedicated measuring equipment. As the 2017 tests were not specifically designed to measure the Young's modulus, the values obtained may have been unreliable. Due to the difficulty of measuring the Young's modulus, it is common practice to use pre-determined or handbook values, rather than calibrating from tensile tests [37]. In literature, the Young's modulus of A356.0-T6 aluminium alloy was found to be 73 GPa [38], and this value was deemed to be more reliable than what was obtained from the UT60 tests.

4.6.4 Validation of Mass and Time Scaling

Internal and kinetic system energies for the quasi-static Tetrahedral model were compared for a simulation where the mass is, on average, multiplied by a factor of 100 and time divided by a factor of 480. The results are shown in Figure 4.18. The kinetic energy in the system is vanishingly small compared to the internal energies, meaning that quasi-static loading conditions are preserved throughout the deformation.

4.7 Comparison of Numerical Baseline Models

4.7.1 Quasi-Static Model

The three baseline models were compared in terms of force vs displacement, deformation mode and fracture behaviour. A comparison of the baseline models in quasi-static loading is shown in Figure 4.19, showing the force vs displacement history. Included in the plot is the average force from the experimental tests. The first notable observation is that the S-B Full Coupling is the most accurate in capturing the first peak, whereas the S-B Simple Coupling is the least accurate. This highlights the importance of the moment transfer between the rim bed and the spokes, in term of accurately capturing the stiffness of the rim. In the S-B Simple Coupling model, the bending moments are not transferred between the rim bed and the spokes, and as a result, the numerical model buckles too much. This is turn affects the way that the model fractures. The short spoke of the S-B Simple Coupling fractures in bending due to the excessive buckling, as opposed to the S-B Full Coupling and the Tetrahedral model which recreates the more abrupt shear fracture seen in the experimental tests.

The S-B Full Coupling accurately captures the second peak force, although at a displacement that is larger than in the experiments. This discrepancy in the displacements can be explained by the size of the mesh and the way that fracture is modelled. Fracture is modelled by element

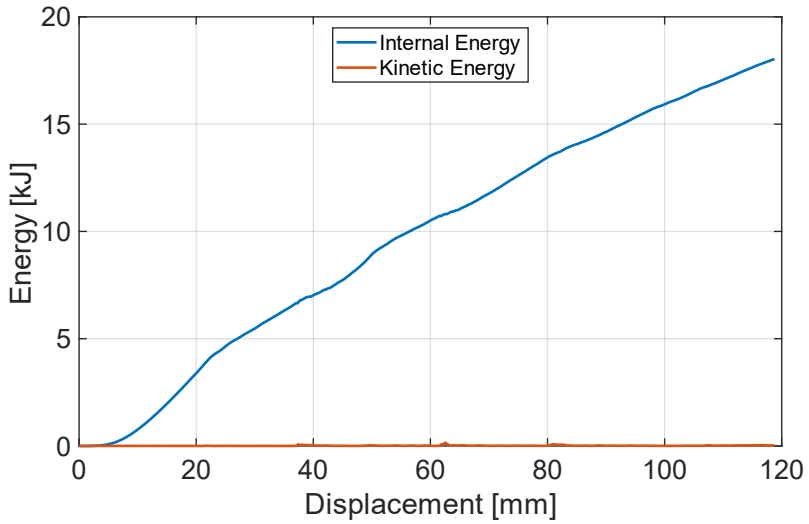

Figure 4.18: Internal and kinetic system energies vs displacement for the quasi-static Tetrahedral model.

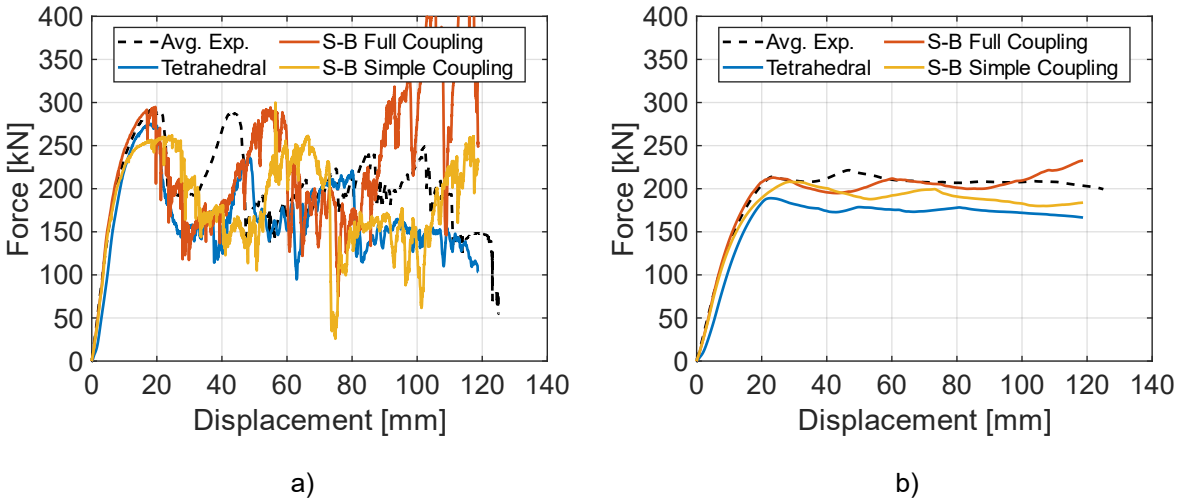

Figure 4.19: Force vs displacement comparison of the quasi-static baseline models, a) force, b) mean force.

erosion, and as the element sizes in the S-B models are quite large, large portions of the spokes are removed each time a segment of element fails. As these failed elements leave behind large empty spaces, the impact wall must travel a certain distance before contact is re-established. This explains why the second peak force is reached later than in the experiments.

The Tetrahedral model has a second peak that is significantly lower than the experimental average. The forces are in general, quite low. This is seen more clearly in the mean force vs displacement plot, where the Tetrahedral model has the largest deviation from the experimental reference. Figure 4.20 shows the eroded elements for all the baseline models at the end of the deformation. It is seen that the model with the largest amount of fracturing is the Tetrahedral model, possibly explaining why this model has the lowest mean forces.

When looking at the deformation history of the Tetrahedral model, it is observed that two of the horizontally oriented spokes fracture before the second force peak. This is not seen experimentally or in the other models, possibly explaining why the force levels beyond this point were considerably reduced. Another possible explanation is the influence of checkboard

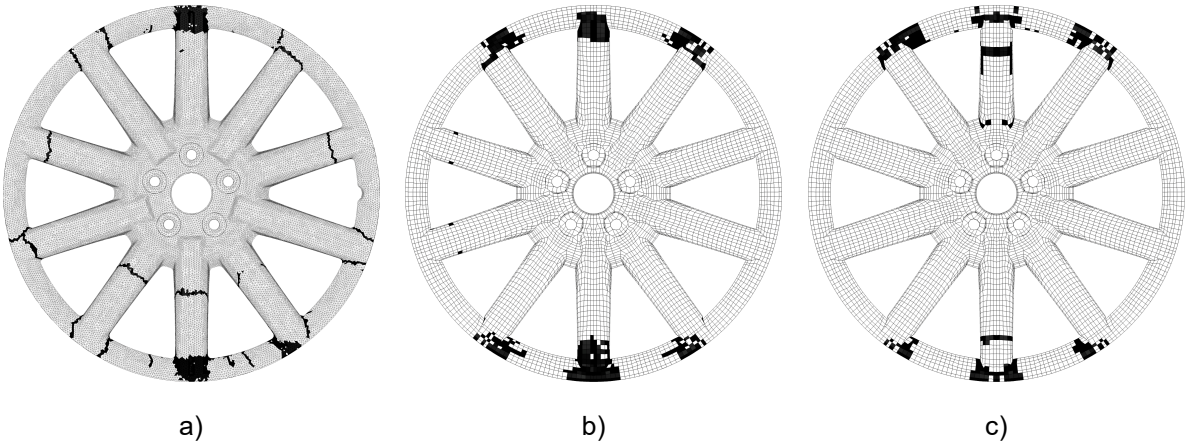

Figure 4.20: Eroded elements at the end of deformation in quasi-static simulations, a) Tetrahedral, b) S-B Full Coupling c) S-B Simple Coupling.

pattern stresses. As discussed in Subsection 4.6.2, checkboard patterning typically seen in tetrahedral elements will accelerate fracture. Although ELFORM = 13 greatly reduces the problem of checkboard patterning, the problem is not completely removed. This can be seen in Figure 4.21, showing the checkboard pattern of the tetrahedral elements in the region in contact with the impact wall.

Figure 4.22 and Figure 4.23 show the out-of-plane displacements fields for each of the baseline models and the fourth quasi-static rim test, for the short and the long spoke, respectively. The last frame before fracture is shown. It is evident that the S-B Simple Coupling buckles excessively before fracture. This is because the simple coupling cannot transfer moments from the rim bed to the spokes, reducing the stiffness against rotation at the interface between the rim bed and the spokes. This highlights the shortcomings of the S-B Simple Coupling model and explains why an incorrect fracture mode is seen. In both the Tetrahedral and the S-B Full Coupling significantly less buckling of the spoke occurs before fracture. As a result, each of these models correctly captures the shear fracture between the rim bed and the spokes.

Lastly, a large difference in simulation time between the models was observed. Although directly comparing the simulation time for the models was made difficult because the simulations were run on a cluster with varying performance, a general trend that the S-B model is far less computationally expensive was seen. Typical computational times for the S-B quasi-static and Tetrahedral model were 30 minutes and nine hours, respectively.

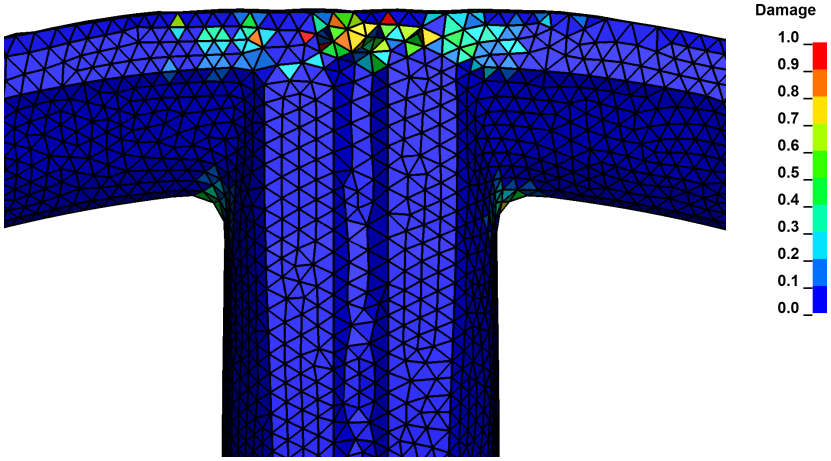

Figure 4.21: Checkboarding damage field in the Tetrahedral model with ELFORM = 13.

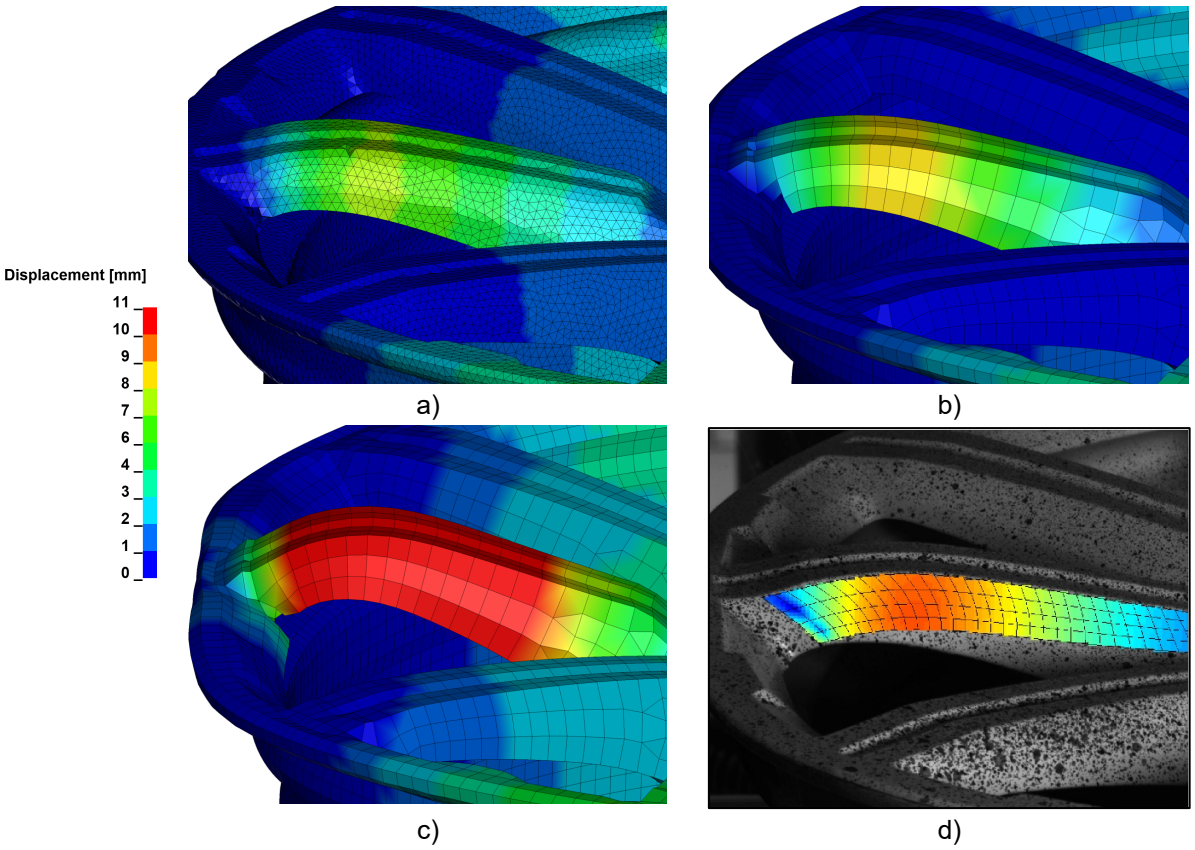

Figure 4.22: Out of plane displacement fields of the short spoke, z-direction, in quasi-static loading, a) Tetrahedral b) S-B Full Coupling, c) S-B Simple Coupling, d) Experimental. Last frame before fracture.

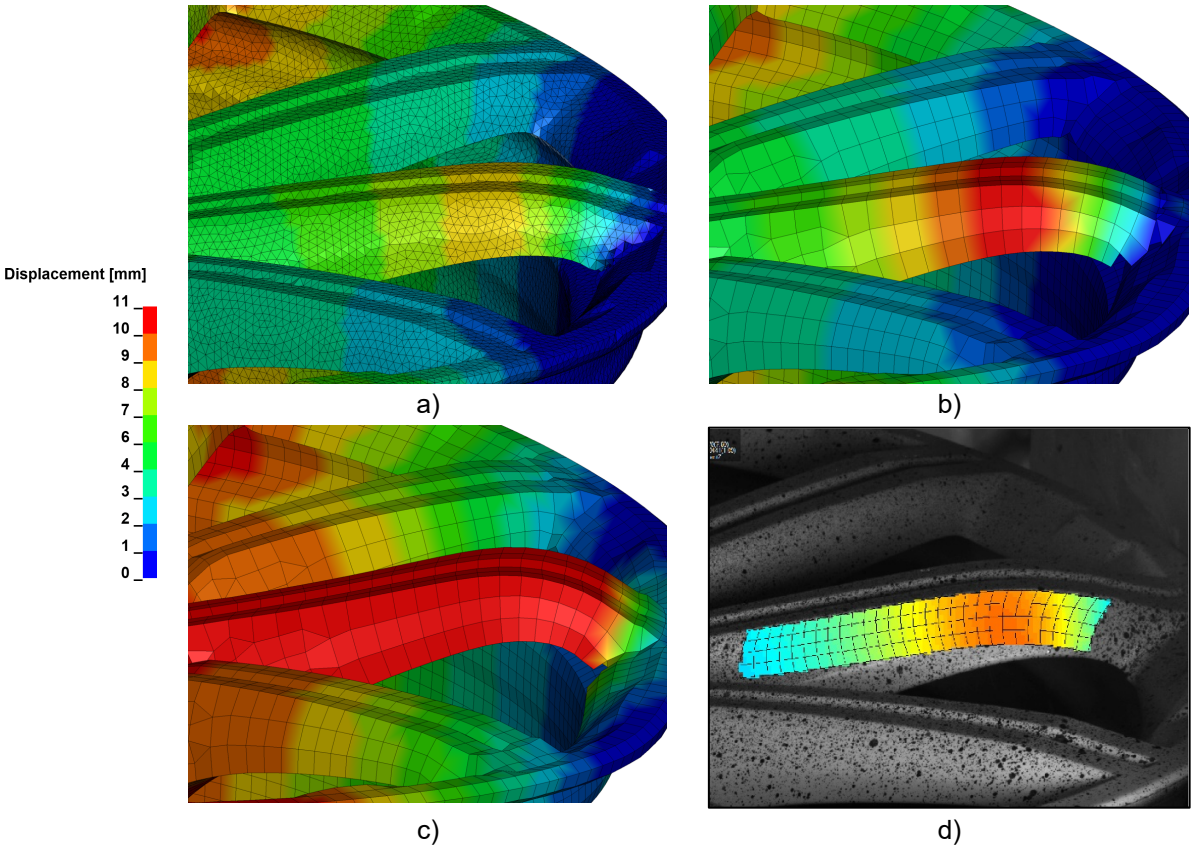

Figure 4.23: Out of plane displacement fields of the long spoke, z-direction, in quasi-static loading, a) Tetrahedral b) S-B Full Coupling, c) S-B Simple Coupling, d) Experimental. Last frame before fracture.

4.7.2 Dynamic Model

Since the overall goal of the project as a whole is to use the rim model in a full-scale dynamic simulation, a comparison of model performance under dynamic loading is of interest. The results from the simulation of the baseline models in dynamic loading are shown in Figure 4.24. The general trend is that the relative differences between the models are smaller than in the quasi-static simulations. This might be due to the addition of inertial forces in the dynamic loading case. The mass difference between the baseline models is small. When inertial forces account for a significant amount of the forces during deformation, the deviations due to stiffness and deformation become smaller, and the models perform more similarly. It is still seen that the S-B Simple Coupling model underestimates the peak forces significantly. However, in the dynamic case, the S-B Full Coupling and Tetrahedral model also underestimate the peak force seen experimentally.

An unanticipated observation is that the difference in spacing between the force peaks seen experimentally was not reproduced numerically. Experimentally, the second peak occurs at approximately $45\,mm$ and $65\,mm$ for the quasi-static and dynamic case, respectively. Whereas, numerically, the second peak occurs at approximately $55\,mm$, a $10\,mm$ offset in both cases. Due to element erosion, the $10\,mm$ offset to the quasi-static experiment is expected. The offset to the dynamic tests, however, is more difficult to explain. Since the increase in the spacing of the peak forces was not captured in the dynamic numerical model, this must either be due to a weakness in the numerical model or due to measuring errors in physical testing. One of the first things that could be done is to measure the end deformation of the rims tested dynamically to verify that the displacement measurement is accurate.

Since these simulations are dynamic and the impact mass and velocity correspond to the experimental tests, it is interesting to look at the energy absorption of the rim. At the end of the deformation, the amount of energy absorbed by all three models is close to the experiments. This can be seen from the mean force vs displacement plots where all the models have roughly the same mean force as the experiments at the end of the deformation, as the absorbed energy is the area under the force vs displacement curve.

Furthermore, it is important to remember that the dynamic results, both experimental and numerical, are affected by the force estimation scheme developed by Martinsen, and Dahler and Thuve [5] [6]. This may make them unsuited for direct comparison with the quasi-static tests where unfiltered forces are measured directly.

Lastly, it is noted that the rims in the quasi-static tests are deformed considerably further than in the dynamic tests. To further assess the performance of the dynamic model, it is therefore desirable to run more physical dynamic tests, this time with higher initial impact velocities.

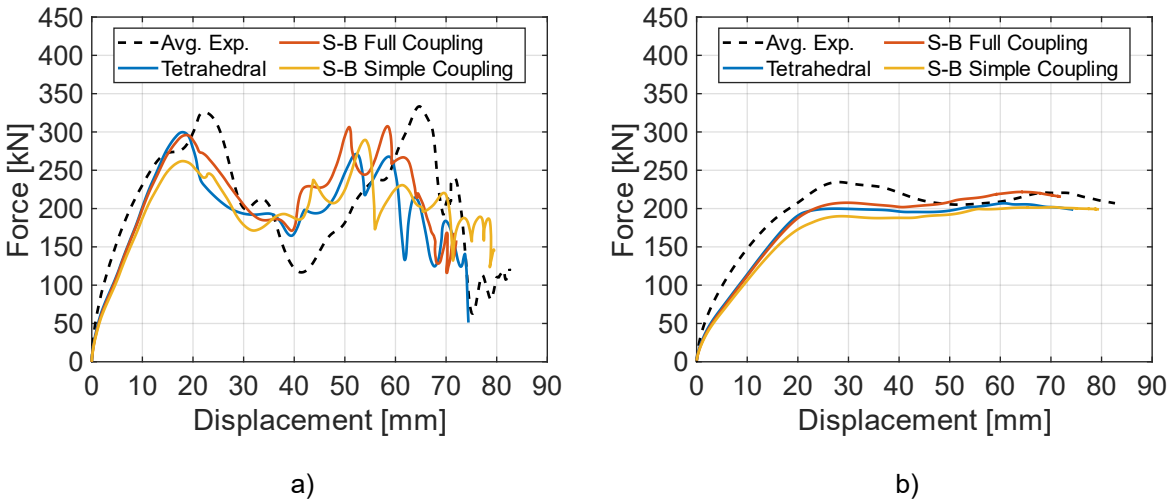

Figure 4.24: Force vs displacement comparison of dynamic baseline models, a) force, b) mean force.

4.8 Parametric Study of Tetrahedral Model

4.8.1 Automatic Mass Scaling

Numerical simulations using different mass scaling factors in the range from 10 to 5,000 were run using the Tetrahedral model. Figure 4.25 shows the force vs displacement history for these values. The difference between 10- and 100-times mass scaling is seen to be small, whereas a further increase above a factor of 100 leads to a significant deviation in the results. The results indicate that the solution converges as the mass scaling is reduced below a factor of 100. As the difference between 10- and 100-times mass scaling is minimal, the mass scaling of factor 100 is deemed to be a reasonable compromise between accuracy and computational cost.

4.8.2 Element Formulation

The performance of various tetrahedral elements available in LS-DYNA was compared, and the results are shown in Figure 4.26. The simulation using ELFORM = 4 was aborted early in the deformation history due to an error. Furthermore, a large variation in performance is observed between the element types, with some showing substantially lower force levels compared to the average experimental results. The only element type to achieve a force vs displacement history comparable to the physical tests is the ELFORM = 13 formulation. In the simulations using the other element types, a significant number of the elements are eroded in the contact area, and a clear checkboard pattern in the stress field is observed. This is especially a problem for ELFORM = 17. It is clear from these results that the previously discussed checkboard patterning of tetrahedral elements is a major problem for all the element types, except for ELFORM = 13 where it is of less concern.

4.8.3 Mesh Size

Figure 4.27 shows the force vs displacement history for various mesh sizes. As the medium and coarse meshed models use fewer elements to represent the rim geometry, they capture the geometry less accurately. However, from the force vs displacement history, it can be seen that the medium and coarse mesh have accurate behaviour, while the fine mesh has poor behaviour in the first part of the deformation.

The poor behaviour of the fine mesh model can be explained by the excessive penetration into the impact wall. A complicating factor in setting up a mesh size study for a problem where contact is an important feature is that the contact stiffness is mesh size dependent. In this case, the contact softens as the mesh of the rim is refined. How this should be corrected for, is not obvious. Due to this, the results from Figure 4.27 cannot be used to draw any conclusions regarding the effect of the mesh size. The mesh size study should be re-run with the same stiffness for all mesh sizes.

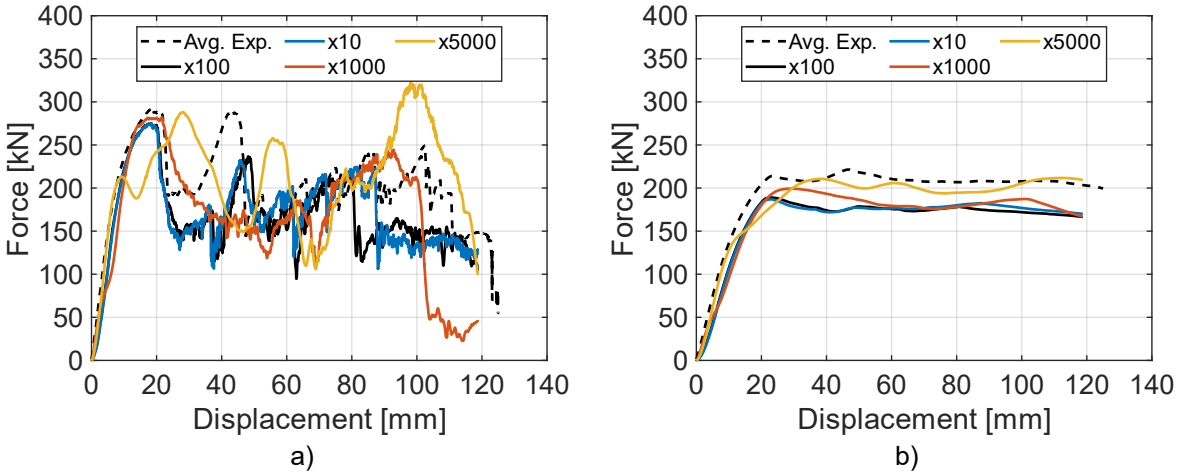

Figure 4.25: Force vs displacement of the tetrahedral numerical model for various mass scaling factors, a) force, b) mean force. Tetrahedral baseline model shown in black solid curve.

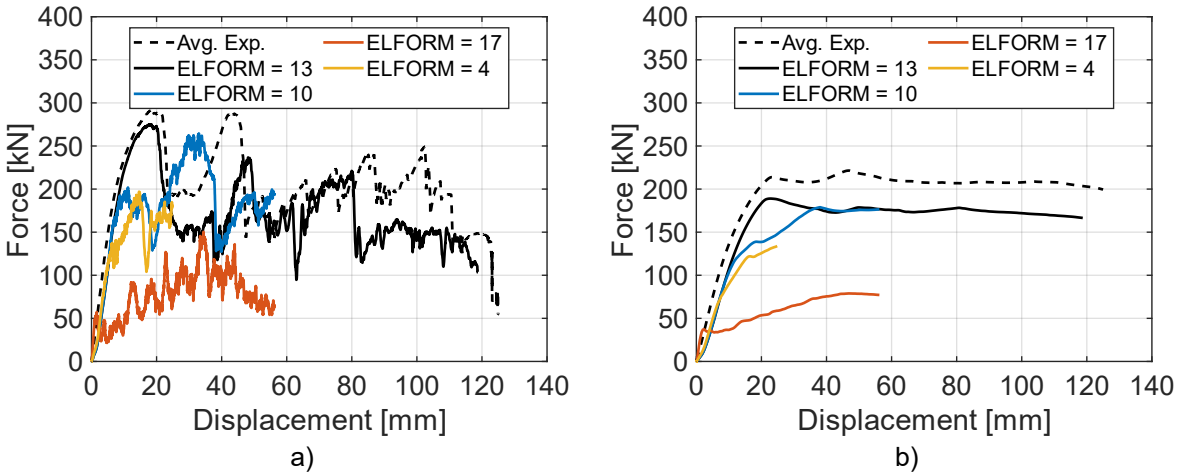

Figure 4.26: Force vs displacement of the tetrahedral numerical model for various element formulations available in LS-DYNA, a) force, b) mean force. Tetrahedral baseline model shown in black curve.

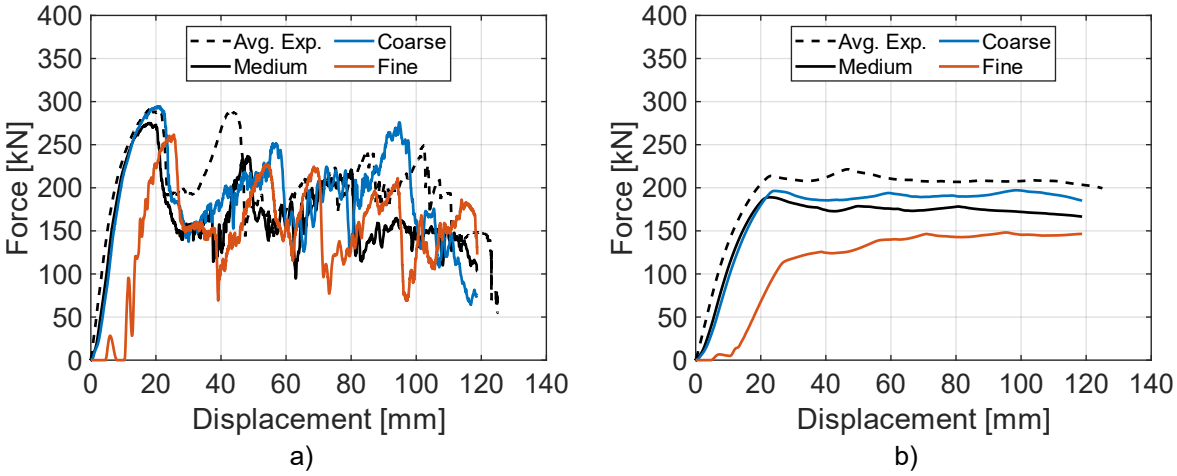

Figure 4.27: Force vs displacement of the tetrahedral numerical model for various mesh sizes, a) force, b) mean force. Tetrahedral baseline model shown in black curve.

4.8.4 Contact Stiffness

The fracture behaviour of the Tetrahedral rim model was seen to be greatly affected by the contact formulation. Different scaling factors for the contact stiffness formulation in LS-DYNA were therefore compared, and the results are plotted in Figure 4.28. During the first part of the deformation, the simulations with lower scaling factors show a lower force level, relative to those with higher scaling factors. This is due to the slave nodes of the rim penetrating further into the master segment of the impact box when the contact is softer. On the other hand, the softer contact formulations show a higher peak force, which is related to the checkboard patterning of the tetrahedral elements. It is seen that the checkboard patterning is worsened by having a stiffer contact, and for this reason, elements are eroded at an earlier stage with high scaling factors, leading to reduced peak forces. Therefore, it is preferable to have a softer contact as a means of circumventing the problem of checkboard patterning. Although softening the contact artificially is an alternative in quasi-static simulations, it should be done with great caution in dynamic simulation as it could influence the response. Lastly, the uncertainty in systematic global variation in material behaviour means that the ductility of the material in the contact area is not known. The actual material behaviour in this region might vary significantly from the spoke material currently used for the entire spoked part.

4.8.5 Fracture Parameter

Different values of the fracture parameter, $W_{c,avg}$, was used in the rim model in order to investigate to what extent the ductility and fracture behaviour of the material would affect the response of the rim. Figure 4.29 shows a clear increase in force as the fracture parameter is increased. This is especially apparent in the mean force plot, as is expected. A higher fracture parameter means that more damage must be accumulated before an element is eroded, which in turn leads to more ductile behaviour.

The impact of the scatter in material properties on the force vs displacement history was also investigated. Although several simulations for each value of the standard deviation would be preferable, only one simulation was run for each standard deviation. The results are shown in Figure 4.30. Only a small variation is seen before the first force peak. After the first force peak, a trend is observed that the models with a larger scatter in the material fracture parameter exhibit more brittle behaviour and generally lower force levels throughout the deformation. More simulations should be performed to confirm this.

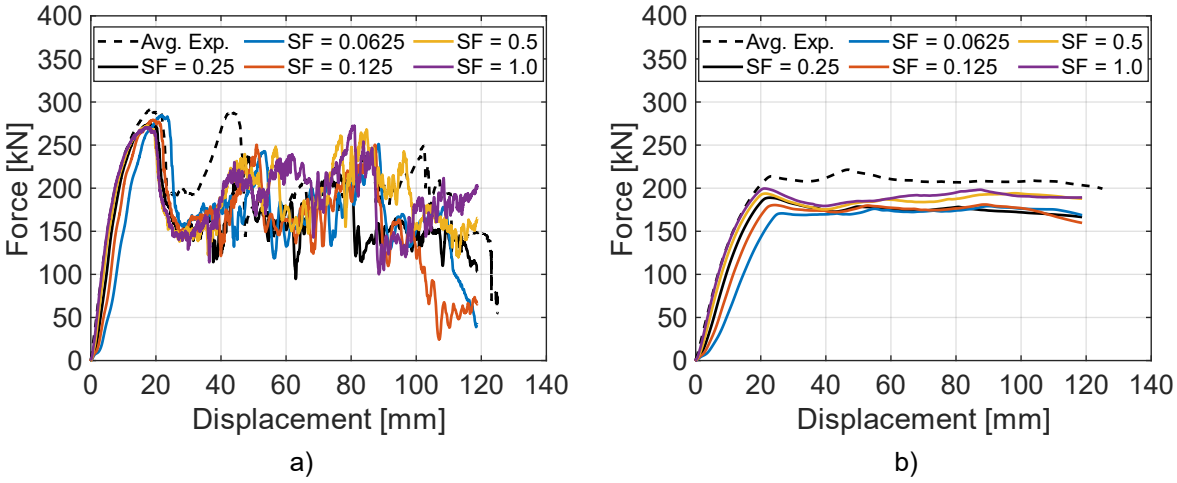

Figure 4.28: Force vs displacement of the tetrahedral numerical model for various contact stiffness scaling factors (SF), a) force, b) mean force. Tetrahedral baseline model shown in black curve.

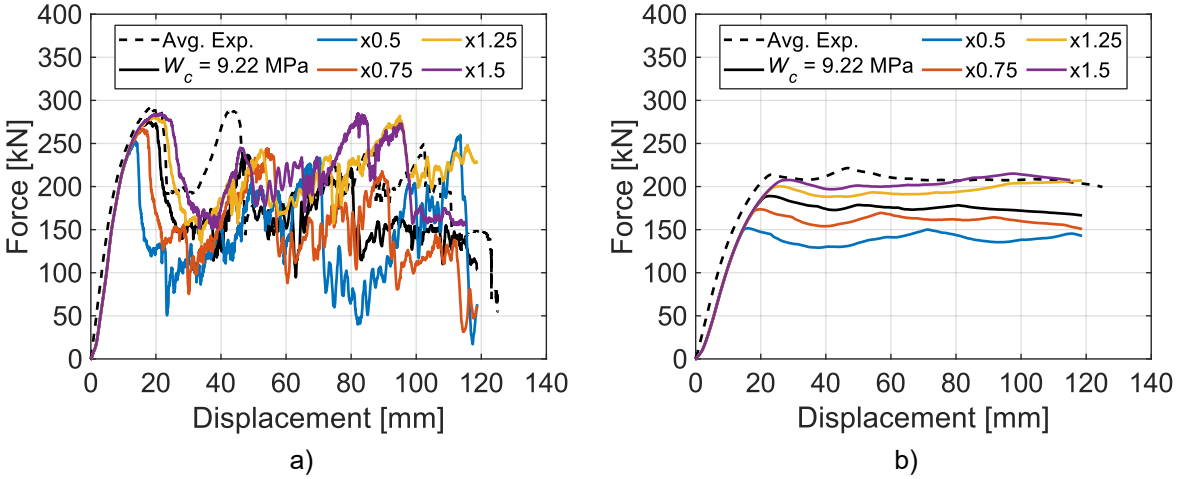

Figure 4.29: Force vs displacement of the tetrahedral numerical model for various fracture parameters, $W_{c,avg}$, a) force, b) mean force. Tetrahedral baseline model shown in black curve.

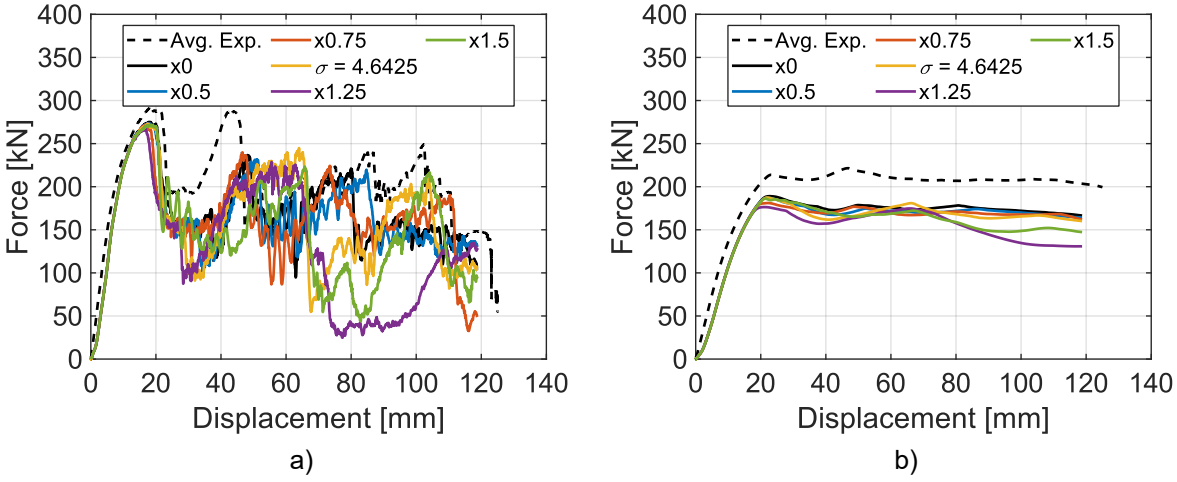

Figure 4.30: Force vs displacement of the tetrahedral numerical model for various values for the standard deviations, σ, a) force, b) mean force. Tetrahedral baseline model shown in black curve.

4.9 Probabilistic Fracture Models

4.9.1 Tetrahedral Model

Three simulations using the probabilistic Weibull CL fracture criterion in combination with the Tetrahedral model were performed. Figure 4.31 shows the resulting force vs displacement histories. It is apparent that the scatter between the three runs is small, and the overall trends and force levels from rim experiments are not captured. The model has a highly ductile behaviour, resulting in too high force levels throughout deformation. Figure 4.32 shows the eroded elements at the end of the deformation for each of the simulations, while Figure 4.33 shows the distribution of the fracture parameter, W_c, for the first simulation.

The increased force levels may be related to the small average element size of the model, which is approximately $V_{avg} = 6.5\,mm^3$. This is much lower than the reference volume, $V_0 = 200\,mm^3$, from the UT60 specimens. Consequently, the average fracture parameter in the numerical model is significantly increased due to the volume dependence of the Weibull PDF. The average fracture parameter for the model is $W_{c,avg} \approx 50\,MPa$, which is about four times the average value used in the non-stochastic model.

In order to explain the ductile behaviour, two aspects of the approach can be discussed. Firstly, the fracture mechanism itself and the fact that FEM is based on continuum mechanics. Because a FE model represents a weakness in the atomic structure of the material by a weakened element, it does not capture the mechanisms by which such defects promote fracture at an atomic level. Secondly, the possibility that the fracture parameters assigned to the elements in a fine mesh exceed the value of the bulk material. It is not known what the fracture parameter of the die-cast aluminium is when no defect is present, making it difficult to determine an appropriate cut off value for the maximum fracture parameter. These aspects are further discussed in Section 5.4, although not exhaustively, as it is not a primary objective in this thesis.

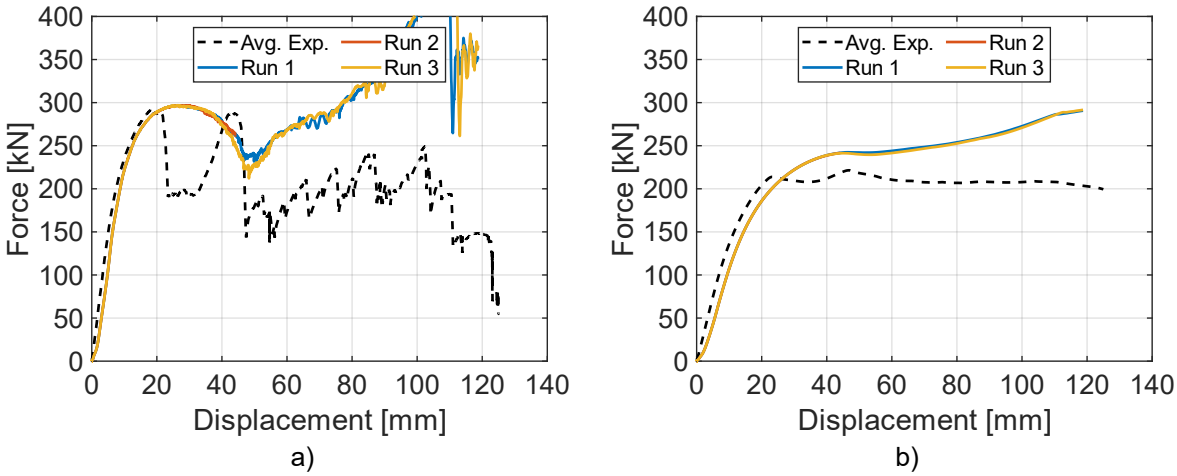

Figure 4.31: Force vs displacement plot of the quasi-static Tetrahedral model with Weibull distributed CL fracture, a) force, b) mean force.

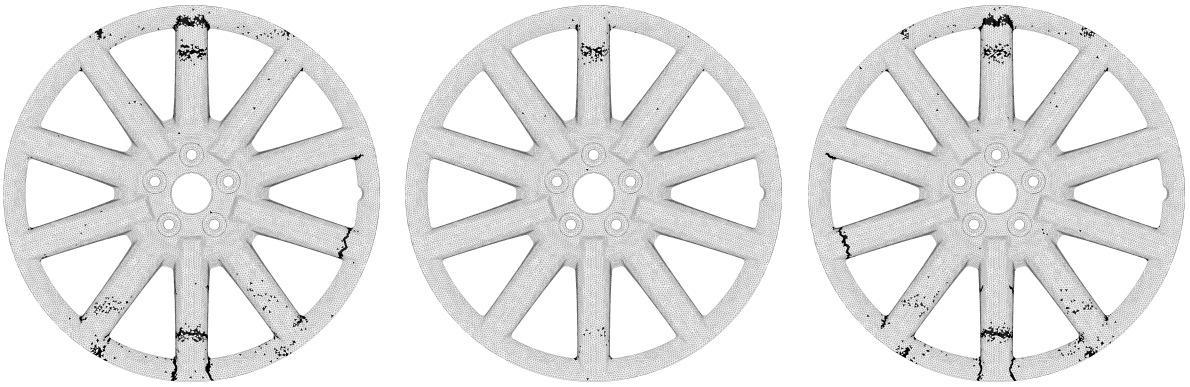

Figure 4.32: Eroded elements at the end of deformation of the quasi-static Tetrahedral model with Weibull distributed CL fracture, a) Run 1, b) Run 2, c) Run 3.

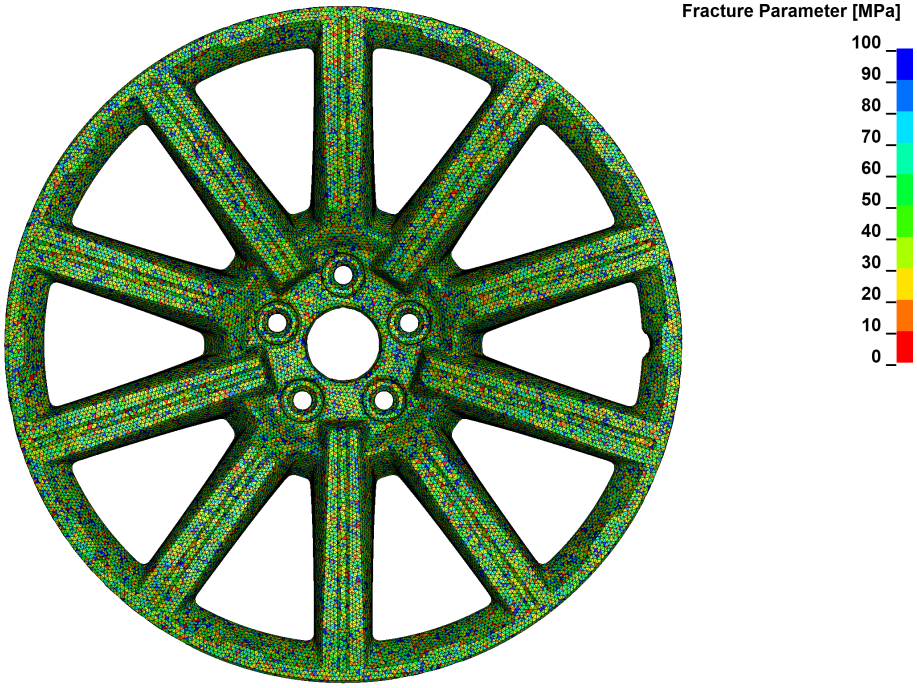

Figure 4.33: Distribution of the stochastic fracture parameter, W_c, in the quasi-static Tetrahedral model with Weibull distributed CL fracture, Run 1.

4.9.2 Shell-Brick Model

Figure 4.34 shows the same probabilistic material model used in the S-B Full Coupling model with much improved results compared to the Tetrahedral model. Figure 4.35 shows the eroded elements at the end of the deformation for each of the simulations, while Figure 4.36 shows the distribution of the fracture parameter, W_c, for the first simulation.

In the S-B Full Coupling model, the average element volume is $V_{avg} = 262.3\ mm^3$, which is much closer to the reference volume, $V_0 = 200\ mm^3$, of the UT60 specimens. Elements are in the range from $V_{min} \approx 100\ mm^3$ to $V_{max} = 600\ mm^3$. The scatter between the different simulation runs is visible but not very large. In comparison to the Tetrahedral model shown in Figure 4.31, the S-B Full Coupling with its larger element size is clearly more accurate. This is an indication that the best results are obtained when the numerical model uses elements that are of similar size to the specimens used to calibrate the stochastic behaviour. To what extent scaling of the element size results in good results is uncertain.

Figure 4.37 shows a simulation run of the S-B Full Coupling where the fracture parameters are assigned to all elements directly from the PDF for the reference volume, V_0. Meaning that the size effect is not accounted for, as it was for the previous simulations. The force vs displacement history of this simulation is very similar to what is seen in Figure 4.34. In order to make any further conclusions, more simulations should be performed.

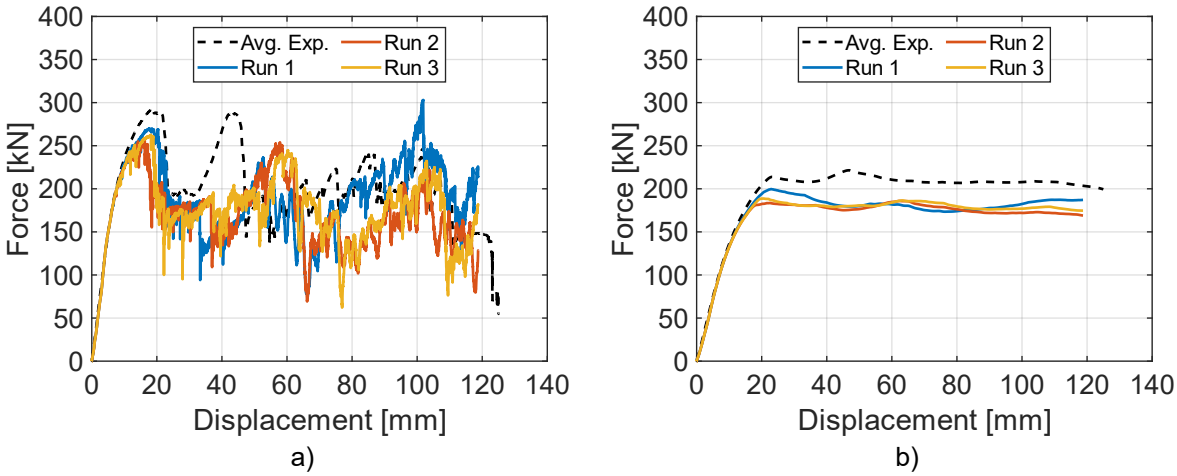

Figure 4.34: Force vs displacement plot of the quasi-static S-B Full Coupling model with Weibull distributed CL fracture, a) force, b) mean force.

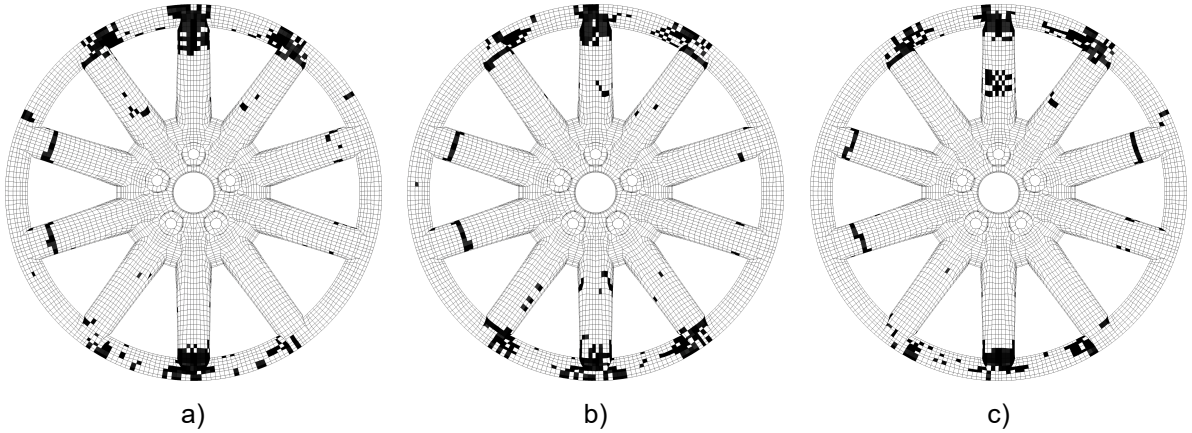

Figure 4.35: Eroded elements at the end of deformation of the quasi-static S-B Full Coupling model with Weibull distributed CL fracture, a) Run 1, b) Run 2, c) Run 3.

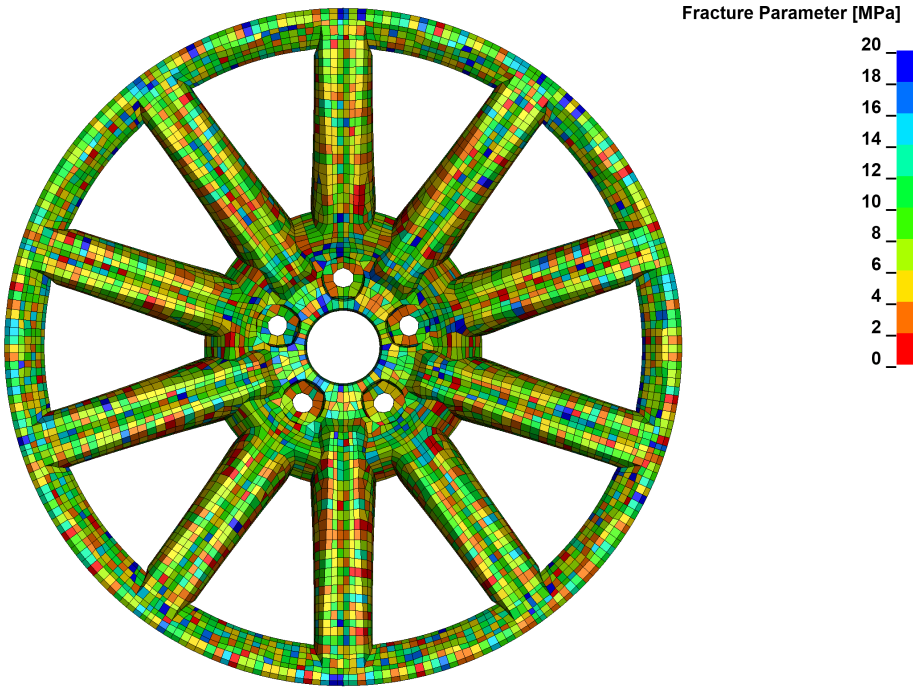

Figure 4.36: Distribution of the stochastic fracture parameter, W_c, in the quasi-static S-B Full Coupling model with Weibull distributed CL fracture, Run 1.

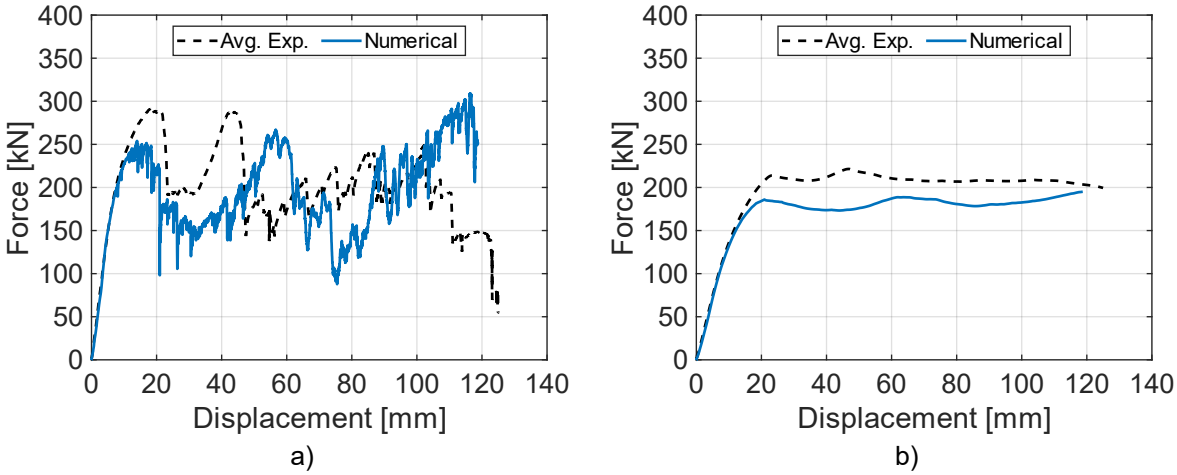

Figure 4.37: Force vs displacement plot of the S-B Full Coupling model with Weibull distributed CL fracture where the size of the elements are not accounted for, a) force, b) mean force.

4.10 Extended Cockcroft-Latham

Simulations on the Tetrahedral model were performed, to study the impact of the ϕ parameter on the overall behaviour of the rim. The results are shown in Figure 4.38. An increase in ductility and force level is observed with decreasing values of the ϕ parameter. It is evident from the results that the ϕ parameter has a great influence on the behaviour of the numerical rim model. The response becomes more brittle as ϕ approaches unity. It is seen that the peak force and the displacement at the first fracture are more accurately captured when $\phi = 0.75$.

Caution must be exercised when drawing any conclusions from these results, as the ECL fracture criterion was not calibrated from physical material tests. Nevertheless, the results show that if the die-cast rim material has a pronounced Lode dependence in its fracture behaviour, it would have a great impact on the force vs displacement history in the numerical model.

No other studies on the ECL fracture criterion in combination with aluminium have been found. The best reference is the steel material that was used to calibrate the ECL fracture criterion in the paper by Gruben et al. They found the value of $\phi = 0.383$ for the Docol 600DL steel. Whether the aluminium rim material has a ϕ parameter close to this value is not known. However, as has been suggested in multiple studies, the importance of the Lode parameter in fracture modelling is significant. This, together with the results shown in Figure 4.38, suggests that the ϕ parameter has a great influence on the overall fracture behaviour of the rim. A method for calibrating the ECL fracture criterion is therefore desired and should be included in any further work.

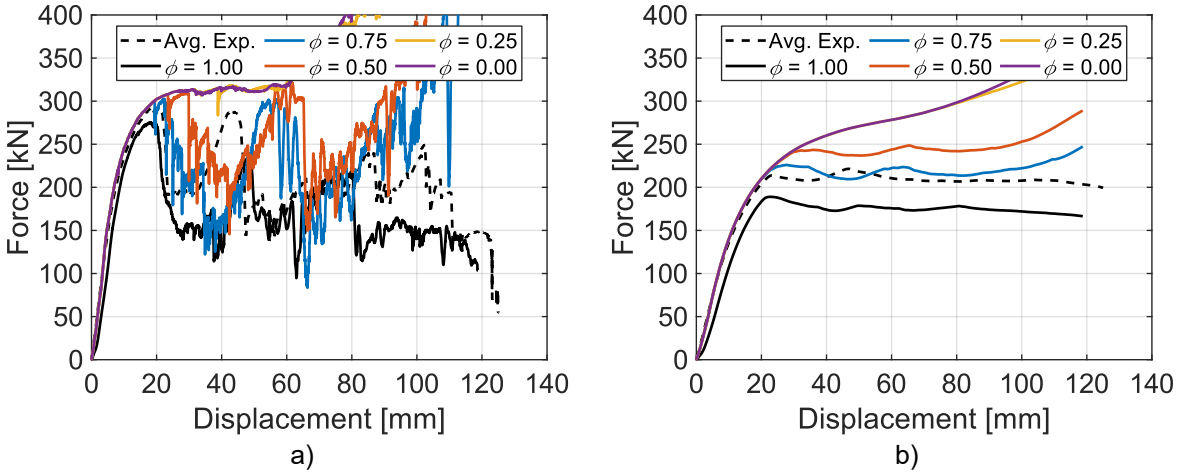

Figure 4.38: Force vs displacement plot of the Tetrahedral model for different values of the ϕ parameter, a) force, b) mean force. Tetrahedral baseline model shown in black curve.

Chapter 5

Discussion

This chapter follows up on the discussion in Chapter 4 and provides a more thorough discussion of the most important finding of the present work

5.1 Stochastic Behaviour of Rims

Based on the characteristics of the die-cast material, a distinct stochastic behaviour of the rim is expected. However, the results from the quasi-static rim tests presented in Section 0 show a distinct transition from a non-stochastic to a stochastic response, as the rim is deformed. Up to a displacement of about $50\ mm$ the rims appear to have a non-stochastic behaviour, as the response is similar. As the material tests show a clear stochastic behaviour, it is not obvious why this non-stochastic response is observed in the rim tests.

When this was further investigated, a notable difference in the deformation mode between the non-stochastic and the stochastic parts of the deformation history was observed. In the non-stochastic part, fracture occurs in a shear mode between the spokes and the rim bed, whereas after this point, fracture occurs in a tension dominated mode in the remaining spokes. The shear dominated fracture mode between the vertically oriented spokes and the rim bed can clearly be seen in the image series in Figure 4.9. It appears that in shear stress states there is a low variation in fracture behaviour, meaning that the material defects possibly do no activate in this type of fracture.

Another factor that must be considered is that the fracture between the spokes and the rim bed might be triggered by the geometry of the rim. In the region were fracture occurs, the geometry of the rim might promote a stress field with concentrated stresses in certain areas. Since the defects are stochastically distributed, this matter. If stresses are localised in a small area, the probability of a critical defect in this region is small. Consequently, the scatter between different rim tests will also be reduced. When fracturing occurs in the remaining spokes, the failing spokes are loaded under tension, meaning that the stresses are not localised in a small region, but rather evenly distributed over the entire spoke. As a larger region is subjected to high stresses, the probability of activating a defect is increased, leading to an increased scatter.

5.2 Material Testing and Selection of Fracture Criterion

The experimental results obtained from material testing of the various specimens were deemed unreliable, and calibration of the ECL fracture criterion was not performed. It was suspected that the presence of defects in the material specimens influenced the results to such a degree that determining the influence of the stress state itself on failure strain was not possible. In Chapter 2, the Weakest-Link approach and the material defects of die-cast aluminium were introduced. It was explained that fracture is promoted by stochastically distributed defects, and that probability of failure increases as a larger material volume is considered. In order to calibrate the ECL fracture criterion, the material behaviour in different stress states had to be evaluated. Specimens designed to apply certain loads were therefore extracted and tested. However, these specimens also had varying volumes where strains localise during loading. Consequently, they also have a varying probability of critical defects in this area. The difference in failure strain between the specimens is suspected to be significantly affected by this size effect.

By taking a look back at past research, it is seen that calibration of a stress state dependent fracture criterion for a die-cast material has been performed by Lee et al. [25]. In their study, they concluded that the Mohr-Coulomb stress state dependent fracture criterion could be successfully calibrated. However, in their analysis, the influence of stochastically distributed defects is not considered or mentioned. Considering the strong influence of defects observed by Knoll, this is a potential weakness in their analysis.

As die-cast materials have stochastic behaviour, care should be taken when attempting to transfer methods of calibrating fracture parameters used on materials with non-stochastic behaviour. In the publication by Gruben et al., where the ECL fracture criterion was proposed, a cold-rolled steel alloy was calibrated. This type of material does not have the same type of stochastically distributed defects as the die-cast aluminium, and the size effect likely influences the test results to a much lower degree. Transferring their approach to a die-cast material has proven to be a challenge. Instead, a calibration procedure should be designed specifically for materials with stochastically distributed defects, where more thought is put into the statistics of the problem. The design of such a material testing programme could possibly evaluate the design of the specimens and the number of tests needed to get reliable results. The possibility of using miniature UT and NT specimens that match the gauge area of the ISS-Venkat specimen could be investigated. A key finding, and suggestion for further work, is therefore to investigate a material testing programme specifically designed for materials with stochastically distributed defects.

The cost of extensive material testing should also be considered when it comes to industrial applications. Often a compromise between cost and accuracy in a model is necessary. As the ECL fracture criterion was not calibrated, a comparison to the simpler CL fracture criterion was not possible. The benefits of using a more complex fracture criterion in impact problems with die-cast aluminium parts can therefore not be determined. It is therefore difficult to draw any conclusions regarding the best compromise between accuracy and cost. Although recent research suggests a benefit of including a Lode parameter dependence in the fracture criterion,

the results show that the CL fracture criterion captures the main trends seen in the force vs displacement plot. Based on the material and component tests in this study, it remains uncertain to what extent a stress state dependent fracture criterion improves the accuracy of the die-cast aluminium alloy in the numerical rim model, and whether the increased costs can be justified.

5.3 Systematic Global Variations in Material Properties

Significant uncertainty remains in the systematic variation of material parameters across the rim. It is unknown whether the material behaviour is the same at the end of the spokes and the lip of the rim, which both are in contact with the impact wall, as in the spokes themselves. The geometry of the rim poses limitations on where specimens can be extracted. By reduction of the specimen size, specimens can be extracted from more locations across the rim. The lip of the rim is a location where the material behaviour is not fully known, and the use of miniature specimens, suggested for calibration of the ECL criterion in the previous section, would enable tests to be machined directly from this area. Another reason miniature why specimens would help determine systematic global variation is that the probability of a critical defect decreases with the size of the specimen. Due to this, a lower scatter is expected, which would reduce the number of tests needed for each test location. However, the accuracy of the miniature specimens should first be evaluated in comparison to the existing UT60 specimen data.

5.4 Numerical Fracture Modelling of Die-Cast Materials

The difference in failure mechanisms between the physical rim and the numerical rim model with a stochastic fracture model should be considered. As was described in Section 2.2, FEM is based on continuum mechanics, meaning that the material completely fills the space it occupies, instead of an atomic structure. In turn, this means that the physical mechanisms of fracture resulting from the breaking of atomic bonds are not captured. Much of the brittle behaviour of the die-cast aluminium alloy is due to defects that amplify the stress in a small region, promoting sudden fracture.

It is not certain that a weak element in a FE model, representing a material defect, will promote fracture in the same manner as in the experimental tests. Over the volume of a spoke, some of the elements are likely to have a low fracture parameter, representing a material defect. As weakened elements fail, the fracture is accelerated in the neighbouring elements, as the load is distributed across fewer elements. However, it is observed that these "defects" are not enough to cause a sudden fracture of the entire section. Experimentally, fracture occurs very suddenly. In the numerical simulation, however, it is much more gradual. When probabilistic fracture was included in the Tetrahedral model, as seen in Section 4.9, the average fracture parameter was increased significantly compared to the non-stochastic approach. This is because the variation in the Weibull PDF used to assign fracture parameters increases as element size is reduced. As a result, the fracture parameters in the model vary between values close to zero and values beyond $100\ MPa$. If this is physically reasonable is uncertain, and how the probabilistic

approach should scale with varying volumes is not apparent. It is possible that in the case of the Tetrahedral model, the average fracture parameter is increased beyond the value of the bulk material itself. With the tests performed so far, this is not possible to determine.

It is out of scope to get into detail about fracture mechanisms, but for further work, it could be interesting to look more into the mechanism by which the material defects cause fracture and how these can be captured numerically.

5.5 Geometric Discretization and Element Selection

5.5.1 Brick Elements

The choice between full and reduced integration brick elements in the S-B models is seen to impact the ductility of the quasi-static simulations significantly, with fully integrated elements being less ductile. Due to the way the user material is implemented, elements are eroded when the first integration point fails. This is typically how fracture and element erosion are implemented in an FE-code. Alternatively, the elements could be eroded when a user-defined number of integration points fail. It is, however, not apparent for the user how many integration points should fail before the element is eroded. The reduced integration elements can result in a too ductile behaviour, especially in bending, since the strains vanish in the integration point. The best choice for representing fracture may be to use reduced integration elements, as they are more efficient and therefore allow for a more refined mesh. The use of simple elements combined with a fine mesh has the benefit that a smaller volume and a smaller amount of mass is removed when fracture occurs.

As the critical time step in an explicit numerical simulation depends on the element with the smallest characteristic length, mesh refinement of the rim might dramatically increase the computational cost of a full-scale model. If the number of time steps doubles, the numerical operations associated with a single time step are doubled for all parts in the model, not only the rim. Whereas for a fully integrated element, the computational cost only increases for the rim itself. For this reason, the choice of element and mesh size can differ if the rim is a part of a full-scale model or analysed separately. In a numerical model where the rim is analysed separately, the use of reduced integration elements and a refined mesh might be the best approach.

5.5.2 Tetrahedral Elements

Complicated geometries are inherently difficult to mesh with brick elements. For this reason, the meshing of complicated geometries such as a rim is time-consuming and expensive. This incentivises the use of automatic tetrahedral meshing algorithms which can mesh complicated geometries easily. Automatic meshing with tetrahedral elements is a common feature in many software packages. The cost of using tetrahedral elements come at generally poorer numerical performance compared to brick elements. As seen in Subsection 4.6.2, many tetrahedral elements formulations are plagued by the formation of checkboard patterns, which in

combination with compressive load and fracture modelling can lead to unphysical behaviours. However, as seen, there are methods to alleviate these problems. In LS-DYNA, ELFORM = 13 is a tetrahedral element formulation that, to a large extent, overcomes these defects and is suitable for dynamic explicit simulations.

Tetrahedral elements may be worth considering, even with their shortcomings. This is especially true if the geometry in question is expected to change often in an iterative design process. Further development of these tetrahedral element formulations may lead to more reliable and versatile element formulations, with an accuracy to rival brick elements.

5.6 Limitations of Work

In order to identify and clearly state the limitations of the present work that might affect the conclusions, a short discussion is included here.

The first limitations are methodological. Concern the limited sample size in various parts of the study and the limitation in available resources. Only a limited number of physical rim tests were performed, with regards to the number of tests and different rim orientations. Also, for the material tests, a limited number of tests was conducted, which is an issue regarding the statistical information that can be extracted. Additionally, a limited resource in the study has been the computational power, putting a boundary on what type of simulations that were possible and imposed certain simplifications on the numerical model.

The second limitations concern the amount of information and knowledge available throughout the project. Within the field of numerical fracture modelling, there is a limited amount of research on the behaviour of die-cast materials. Especially when it comes to the calibration of a stress state dependent fracture criterion, only one research paper was found as a reference to the methods and results obtained in the present work. Also, uncertainty remains regarding rim production processes and batch variations, as information about this was not disclosed to the authors.

The third limitation is regarding time constraints. In prioritising the available time, a priority was made to pursuit novel work instead of spending considerable amounts of time to evaluate the correctness of the previous work. This includes evaluation of the force estimation scheme, test rig design, and other data that was used from previous work. Furthermore, additional dynamic rim tests could not be performed due to time limitations.

Lastly, the work has been limited by restrictions following the outbreak of Covid-19. How the thesis was impacted is further clarified in Impact of Covid-19 Restrictions on Thesis Work.

Chapter 6

Conclusion and Further Work

6.1 Conclusion

A conversion of the rim and test rig FE models from Abaqus to LS-DYNA was successfully completed, and a user material with the desired formulations was implemented. This work was carried out with the help from co-supervisor Torodd Berstad.

Based on a literature review on stress state dependent fracture, it was decided that the numerical rim model would benefit from using a Lode-dependent fracture criterion. For this purpose, the ECL fracture criterion was selected and implemented in an LS-DYNA user material. Material tests were performed to characterize the stress state dependence of the material. However, the results disagreed with what was anticipated based on the reviewed research. This was believed to be due to the stochastically distributed defects in the material and the volumetric differences between the specimens having an influence on the results. Consequently, the calibration of the fracture criterion was not carried out.

From previous and new material tests, the parameters of a probabilistic fracture criterion were determined. For this purpose, the Weibull distribution was used. The probabilistic fracture criterion was implemented in the LS-DYNA user material, and several simulations were run on the S-B Full Coupling and Tetrahedral model. The S-B Full Coupling model captured the same trends that were seen from the physical rim tests. However, the Tetrahedral model, with its small elements, showed a much too ductile behaviour. This was found to be an issue with the way the Weibull distribution scales with the element volume and how the FE model captures the fracture mechanisms.

Quasi-static rim tests were carried out using the test rig. Four rims were crushed, and the force vs displacement history recorded, along with images of the deformation. The rims were oriented in the short spoke configuration and deformed to approximately $120\ mm$. With this orientation, little scatter between the tests was observed up until approximately $50\ mm$ and before the second spoke failed. Beyond this point, the structural response of the rim is clearly stochastic. It remains uncertain what causes this transition between non-stochastic and stochastic behaviour.

Extensive numerical simulations have been carried out to investigate various aspects of FE modelling. The importance of the coupling in the S-B model has been evaluated. It was found that the transfer of moment between the rim bed and the spokes is of vital importance. The S-B Simple Coupling model was found to lack stiffness and had significantly lower forces throughout deformation compared to the S-B Full Coupling model. Furthermore, the performance of a tetrahedral model was investigated, both by comparison to the S-B Full Coupling model and in a parametric study. In comparison, the S-B Full Coupling model the Tetrahedral model shows a similar force vs displacement behaviour. Although the Tetrahedral model can be automatically meshed, it shows a significant increase in computational cost. In the parametric study, it was found that the FEM formulation used in the baseline Tetrahedral model was acceptable.

The quasi-static rim tests were compared to previous dynamic tests, and some differences were observed. Higher forces were seen in the dynamic tests and explained by the presence of inertial forces and strain rate dependence of the material. More scatter was seen up to the second peak between the different tests under dynamic loading, compared to quasi-static. This is believed to be due to the way the forces are measured and estimated in the dynamic tests.

6.2 Further Work

6.2.1 Material Testing

As the ECL fracture criterion could not be calibrated, the effects of a stress state dependent fracture criterion could not be investigated. In order to assess the impact of a more advanced fracture criterion, a material testing programme should be devised. The programme should include specimens under different stress states, but with similar gauge volumes. The possibility of using miniature specimens should also be looked into, as it could help with the problems faced with the currently tested material specimens.

The rim is divided into two sections, the Spokes and the Rim Bed, due to the systematic variation in the material parameters. With miniature specimens, it would be possible to extract specimens from far more location in the rims and thereby further investigate the systematic global variation in the material parameters. For example, the area where the spokes connect to the rim bed has been shown to fracture too easily in numerical simulations.

6.2.2 Rim Testing

In order to gain more insight into the structural and stochastic behaviour of the rims, it is suggested that different orientations of the rim in the impact box should be tested. The orientations may first be performed numerically in order to ensure its safety.

Lastly, dynamic tests with a higher impact velocity should be considered. This would induce a larger deformation, which would be more comparable to the quasi-static tests. Differences in rim behaviour under dynamic and quasi-static conditions could be investigated, and the dynamic measurements could be further evaluated. Measure the final deformation of the rims.

References

[1] V. Bond Jr., "Automotive News," 07 03 2013. [Online]. Available: https://www.autonews.com/article/20130307/OEM11/130309871/honda-volvo-models-get-high-marks-in-new-overlap-crash-tests. [Accessed 02 03 2020].

[2] Insurance Institute for Highway Safety (IIHS), *Small Overlap Frontal Crashworthiness Evaluation,* Ruckersville, 2017.

[3] Insurance Institute for Highway Safety (IIHS), "2017 Audi Q7," [Online]. Available: https://www.iihs.org/ratings/vehicle/Audi/q7-4-door-suv/2017. [Accessed 31 January 2020].

[4] E. Kittilsen and E. Swanberg, Behaviour and modelling of cast aluminium rims subjected to impact loading, Trondheim, 2017.

[5] C. Martinsen, "Modelling and testing of thick aluminium castings under impact loadings," Trondheim, 2018.

[6] F. B. Dahler and N. Thuve, "Testing and Modeling of Thick Aluminum," Trondheim, 2019.

[7] The Aluminum Association, "Automotive," [Online]. Available: https://www.aluminum.org/product-markets/automotive. [Accessed 15 May 2020].

[8] M. P. Groover, Fundamentals of Modern Manufacturing, 4th Edition, John Wiley & Sons, Inc., 2010.

[9] O. Knoll, "A Probabilistic Approach in Failure Modelling of Aluminium High Pressure Die-Castings," Norwegian University of Science and Technology, Trondheim, 2015.

[10] W. D. Callister and D. G. Rethwisch, Materials Science and Engineering: An Introduction, Eight Edition, John Wiley & Sons, Inc., 2009.

[11] Wikipedia, "Continuum mechanics," [Online]. Available: https://en.wikipedia.org/wiki/Continuum_mechanics. [Accessed 16 May 2020].

[12] O. Hopperstad and T. Børvik, "Lecture Notes - Materials Mechanics," 2017.

[13] O. S. Hopperstad and T. Børvik, Impact Mechanics - Part 1: Modelling of plasticity and failure with explicit finite element methods, Trondheim, 2018.

[14] Y. Chen, A. Clausen, O. Hopperstad and M. Langseth, "Stress–strain behaviour of aluminium alloys at a wide range of strain rates," International Journal of Solids and Structures, 2009.

[15] T. Børvik, O. S. Hopperstad, T. Berstad and M. Langseth, "A computational model of viscoplasticity and ductile damage," *European Journal of Mechanics - A/Solids,* 2001.

[16] Wikipedia, "Hypoelastic material," [Online]. Available: https://en.wikipedia.org/wiki/Hypoelastic_material. [Accessed 16 May 2020].

[17] Y. Bai and T. Wierzbicki, "A new model of metal plasticity and fracture," *International Journal of Plasticity,* 2008.

[18] D. Mohr and S. J. Marcadet, "Micromechanically-motivated phenomenological Hosford–Coulomb," *International Journal of Solids and Structures,* 2015.

[19] Y.-S. Ma, D.-Z. Sun, F. Andrieux and K.-S. Zhang, "Influences of initial porosity, stress triaxiality and Lode parameter on plastic deformation and ductile fracture," *Acta Mechanica Solida Sinica,* 2017.

[20] S. Bergo, D. Morin, T. Børvik and O. S. Hopperstad, "Micromechanics-based identification of a ductile fracture model for," *Engineering Fracture Mechanics,* 2019.

[21] A. Benzerga, D. Surovik and S. Karalavarma, "On the path-dependence of the fracture locus in ductile," *International Journal of Plasticity,* 2012.

[22] G. Gruben, O. Hopperstad and T. Børvik, "Evaluation of uncoupled ductile fracture criteria for the dual-phase steel Docol 600DL," 2012.

[23] C. C. Roth, T. Fras, N. Faderl and D. Mohr, "Benefits of Using Lode Angle Dependent Fracture Models to Predict," *EPJ Web of Conferences,* 2018.

[24] X. Xiao, Z. P. H. Mu and Y. Lou, "Effect of the Lode parameter in predicting shear cracking of 2024-T351," *International Journal of Impact Engineering,* p. 185–201, 2018.

[25] J. Lee, S.-J. Kim, H. Park, H. J. Bong and D. Kim, "Metal plasticity and ductile fracture modeling for cast aluminum alloy parts," *Journal of Materials Processing Tech.,* vol. 255, pp. 584-595, 2018.

[26] Livermore Software Technology Corporation (LSTC), *LS-DYNA® - Keyword User's Manual: Volume II,* California, 2018.

[27] K. M. Mathisen, *TKT4197 - Nonlinear Finite Element Analysis: Lecture 7 - Solution of the Dynamic Equilibrium Equations by Explict Direct Integration,* Trondheim, 2019.

[28] Dassault Systèmes Simulia Corp., *Abaqus 6.14 Analysis User's Guide: Volume II: Analysis,* Providence, 2014.

[29] K. Bell, An engineering approach to finite element analysis of linear structural mechanics problems, Trondheim: Fagbokforlaget Vigmostad & Bjørke AS, 2013.

[30] J. Bonet and J. Burton, "A simple average nodal pressure tetrahedral element for incompressible and nearly incompressible dynamic explicit applications," *Communications in Numerical Methods in Engineering,* no. 14, pp. 437-449, 1998.

[31] DYNAmore GmbH, "Contact modeling in LS-DYNA," [Online]. Available: https://www.dynasupport.com/tutorial/ls-dyna-users-guide/contact-modeling-in-ls-dyna. [Accessed 29 May 2020].

[32] Flintec, "Load Cells," [Online]. Available: https://www.flintec.com/weight-sensors/load-cells. [Accessed 24 April 2020].

[33] Baumer, "Laser distance sensors," [Online]. Available: https://www.baumer.com/ch/en/product-overview/distance-measurement/laser-distance-sensors-/c/289. [Accessed 24 April 2020].

[34] S. N. Olufsen, M. E. Andersen and E. Fagerholt, "μDIC: An open-source toolkit for digital image correlation," *SoftwareX,* vol. 11, 2020.

[35] E. Fagerholt, "eCorr v4.0 Documentation," 2017. [Online]. Available: http://folk.ntnu.no/egilf/ecorr/doc/index.html. [Accessed 04 March 2020].

[36] Livermore Software Technology Corporation (LSTC), *LS-DYNA® - Keyword User's Manual: Volume I,* California, 2018.

[37] J. Lord and R. Morrell, *Measurement Good Practice Guide No. 98: Elastic Modulus Measurement,* Teddington: National Physical Laboratory, 2006.

[38] J. G. Kaufman, Introduction to Aluminum Alloys and Tempers, Ohio: ASM International®, 2000.

[39] C. Dørum, "Behaviour and modelling of thin-walled cast components," Norwegian University of Science and Technology, Trondheim, 2005.

[40] C. Dørum, O. Hopperstad, T. Berstad and D. Dispinar, "Numerical modelling of magnesium die-castings using stochasticfracture parameters," Engineering Fracture Mechanics, 2009.

[41] D. Morin, B. Kaarstad, B. Skajaa, O. Hopperstad and M. Langseth, "Testing and modelling of stiffened aluminium panels subjected to quasi-static and low-velocity impact loading," *International Journal of Impact Engineering,* 2017.

[42] M. B. Gorji and D. Mohr, "Predicting shear fracture of aluminum 6016-T4 during deep drawing: Combining Yld-2000 plasticity with Hosford–Coulomb fracture model," *International Journal of Mechanical Sciences,* 2018.

[43] M. Dunand and D. Mohr, "Effect of Lode parameter on plastic flow localization after proportional loading at low stress triaxialities," *Journal of the Mechanics and Physics of Solids,* 2014.

[44] Livermore Software Technology Corporation (LSTC), *LS-DYNA® - Keyword User's Manual: Volume III,* California, 2018.

[45] Livermore Software Technology Corporation (LSTC), *LS-DYNA® Theory Manual,* California, 2018.

[46] Eurostat, "Road accident fatalities - statistics by type of vehicle," June 2019. [Online]. Available: https://ec.europa.eu/eurostat/statistics-explained/index.php?title=Road_accident_fatalities_-_statistics_by_type_of_vehicle. [Accessed 05 June 2020].

Impact of Covid-19 Restrictions on Thesis Work

Admission to campus at the Norwegian University of Science and Technology was suspended for student's 12th March, which has put some limitations on the authors work during this master's thesis. To clarify what parts of the present work have been affected or limited by the restrictions following the outbreak of Covid-19, a short notice is included.

After the lock-down of the campus, all communication between the authors and work has been done remotely from separate locations. Communication with supervisors has been done via video conference and mail. Although, this has somewhat limited the quality of communication between the authors and with the supervisors, getting advice and help has not been a challenge. Communicating took more time. However, the author's supervisors have been helpful. Collaboration has continued the same way as before, only limited by the restrictions in communication introduced by digital communication.

When it comes to the experiments, the component tests had already been completed in February. These were the most important ones. However, some notable challenges are necessary to mention as they have made the project more difficult and some aspects more time consuming than expected. Firstly, the material tests of the spokes were performed without the authors being present, making it more difficult to control and document the experimental work for these tests. Secondly, with a total amount of data up to 1 TB for the project, transfer across different computers and servers has been very time-consuming. This has made some parts of the work a challenge and added significant time to the completion of the project. As a solution, much of the work has been split up between the authors, limiting the amount of data transfer. However, this has also slowed down the collaboration, gaining of mutual understanding and knowledge sharing.

The challenges posed by the outbreak of Covid-19 has made parts of the thesis significantly more time-consuming. Continuous collaboration between the authors was made difficult, and the transfer of large amounts of data from simulations and experiments was time-consuming. This has not necessarily impacted the quality of the work but has imposed some limitations on the direction taken in project and collaboration.

Appendix

A-1. Machine Drawings of Spoke Specimens

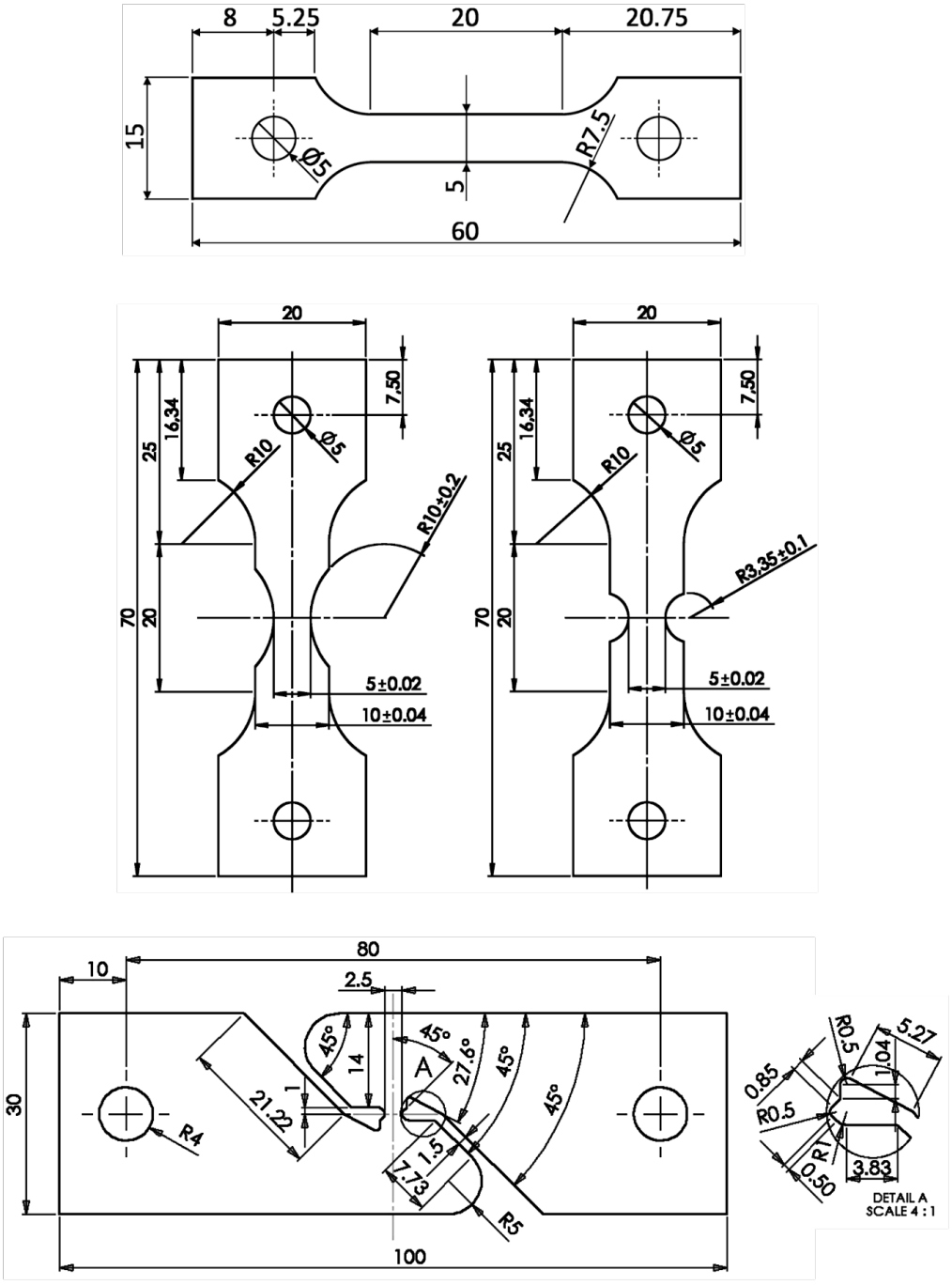

Figure A-1: Machine drawings of specimens, from top to bottom and left to right, UT60, NT10, NT335, ISS-Venkat. All lengths in millimetres. Thickness of all specimens is 2 mm.

A-2. 3D-DIC Camera Set-Up

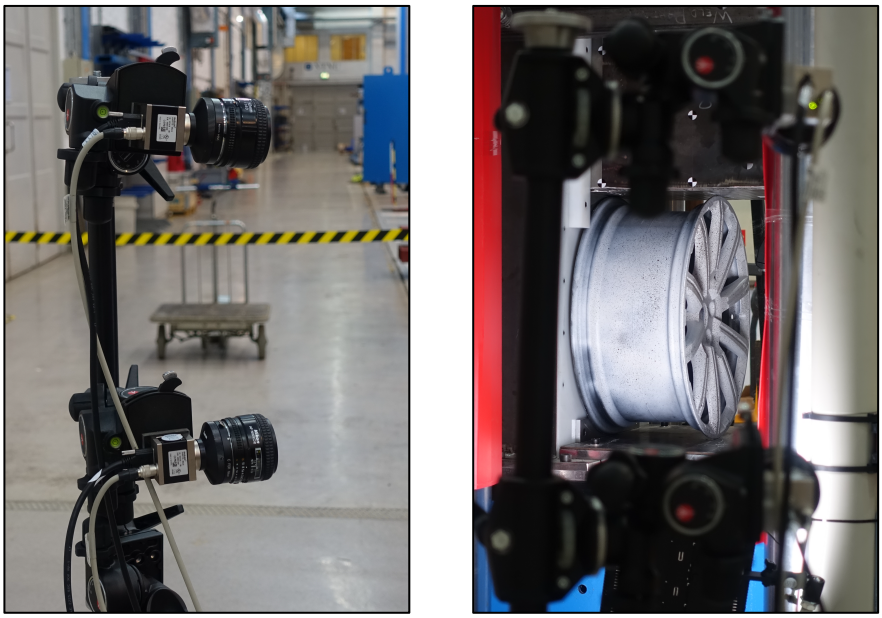

a) b)

Figure A-2: Camera set-up for 3D-DIC, a) camera placement, b) camera view.

A-3. Cover Plate

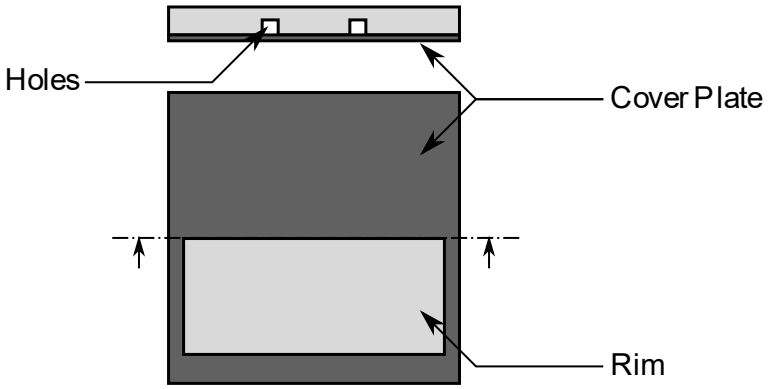

Figure A-3: Cover plate and impact wall in test rig.

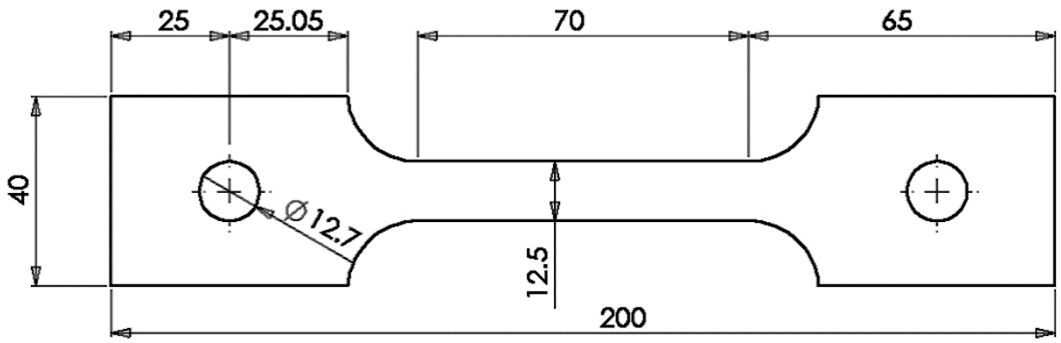

Figure A-4: Measurements of UT200 specimen in millimeters.

A-4. Material Tests of Spokes

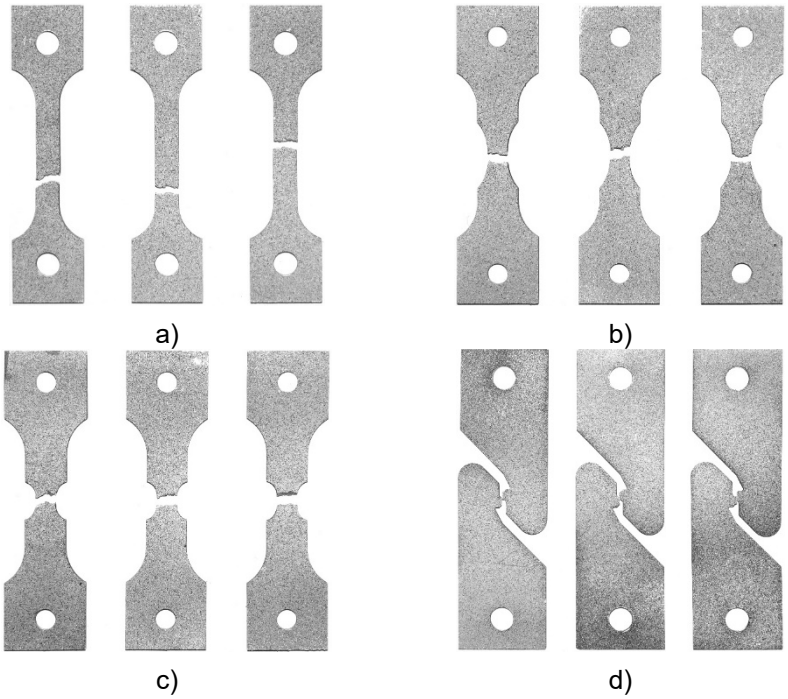

Figure A-5: Fractured specimens, a) UT60, b) NT10, c) NT335, d) ISS-Venkat.

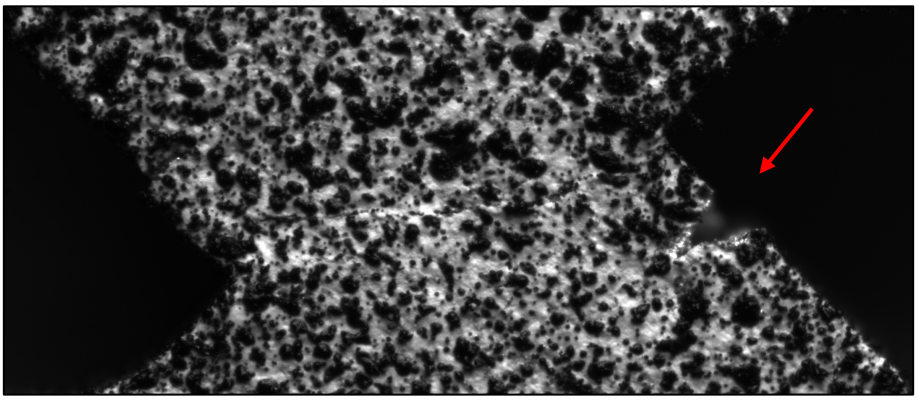

Figure A-6: Formation of a crack in the ISS-Venkat specimen.

Bjørn Gjertsen, Sondre Tjessem

Testing and Modelling of Thick Aluminium Castings Under Impact Loadings

NTNU
Norwegian University of
Science and Technology

Audi